Permeation of Nanoparticles through a Model Membrane:

CG-MD Simulations Studies

BY

Bo Song

B.S., Xiamen University, Xiamen, 2005

M.S., Xiamen University, Xiamen, 2008

THESIS

Submitted as partial fulfillment of the requirements
for the degree of Doctor of Philosophy in Chemical Engineering
in the Graduate College of the
University of Illinois at Chicago, 2012

Chicago, Illinois

Defense Committee:

Sohail Murad, Chair and Advisor
Lewis E. Wedgewood
Ludwig C. Nitsche
Cynthia J. Jameson, Chemistry
Ashfaq Khokhar, Electrical and Computer Engineering

ACKNOWLEDGMENTS

I would like to begin by acknowledging my Ph.D advisor, Dr. Sohail Murad, for his patiently guidance and continued financial support throughout this work. Without him, this Ph.D work would not have been possible. I would like to acknowledge Dr. Cynthia J. Jameson, for helping me with my research and always be energetic and loving the fun research brings. I would also like to acknowledge Dr. Huajun Yuan for the discussion in my research and the helps in my daily life.

My sincerest thanks should be given to Dr. Lewis E. Wedgewood, Dr. Ludwig C. Nitsche and Dr. Ashfaq Khokhar for serving as members of my dissertation committee. I thank Dr. John Regulabuto, Dr. Randall J. Meyer, Dr. Ying Liu and Dr. Belinda Akpa for their valuable course work and the discussions in the course work. I take this opportunity to thank Dr. Raffin Turian and Dr. Jeffery P. Perl for their guidance and patience when I served as a teaching assistant. I thank department staff Karen Millar, Bill Schmilke and John Sitas for helping me to maintain a pleasant working environment. Thanks should also be given to all of my friends I have found over the years past and present.

I would like to express my heartfelt gratitude to Xiumin Liu whom I was lucky enough to meet at Xiamen University and who subsequently became my best friend and my wife. Finally, my sincerest love and gratitude should be given to my parents for their unwavering support and love.

This work has been supported by the Department of Energy DOE, Office of Basic Energy Science grant [Grant No. DE-FG02-08ER46538] and by the National Science Foundation [CBET-0730026].

B. Song

TABLE OF CONTENTS

LIST OF TABLES

LIST OF FIGURES

SUMMARY

How nanoparticles interact with biological membranes and the structural and mechanical properties of membranes during the nanoparticle permeation are of significant importance in determining the toxicity of nanoparticles as well as their potential applications in phototherapy, imaging and gene/drug delivery. In this work, coarse-grained molecular dynamics (CG-MD) simulations are carried out to explore the permeation characteristics of nanoparticles through a model membrane as well as the structural and mechanical properties of the membrane. We study gold nanoparticles as our model nanoparticles and a self-assembled DPPC lipid bilayer as our model membrane. A series of simulations are performed to validate the coarse-grained model for nanoparticles and lipid membrane. We start with various sizes of nanocrystals (bare nanoparticles) and then compare the differences in permeation behaviors between bare nanoparticles with ligand-coated nanoparticles with various ligand lengths to provide insights into how the ligands affect the permeation process. After that, CG-MD is applied to investigate the water penetration, ion transport and lipid molecule flip-flop phenomenon during nanoparticle permeation. The effect of ion concentration, pressure differential across the membrane, nanoparticle size and permeation velocity have been examined in this work. Finally, CG-MD is implemented to explore a method for the calculation of membrane compressibility. Membrane behavior for conditions not studied experimentally is also predicted by our method. The findings described in our work will lead to a better understanding of nanoparticle permeation process, nanoparticle-lipid membrane interactions, membrane deformation and should help in developing more efficient nanocarrier drug delivery systems while avoiding cell cytotoxicity.

1. INTRODUCTION AND SCOPE OF THE THESIS

In this thesis, we apply coarse-grained molecular models to investigate the permeation process of nanoparticles through a model membrane as well as the structural and mechanical properties of biological membranes. The objective of this chapter is to introduce the background of this study, the components of the system (model membrane and nanoparticles) and their key characteristics. We will elaborate on why it is important to study and understand such permeation processes, how computer simulations and molecular modeling can be instrumental in gaining this knowledge and review the state of the art in this field. Finally, we also will formulate the scope and objectives of this thesis and provide an outline of its structure.

1.1 The Biological Membrane and Lipid Bilayers

Cell membrane is the basic structural part of a cell that encapsulates its contents and defines the intra- and extra- cellular space. It provides the integrity of the cell structure; it regulates the transport of molecules across the cell (gases, ions, nutrients etc.) and maintains the cell potential. Also, the cell membrane can serve as a protective barrier, which prevents transport of undesired molecules into the cell.

The most accepted representation of biological membranes, the fluid mosaic model (Figure 1) [1], was introduced by Singer and Nicolson in 1972. In this description, a membrane is composed mainly of lipid molecules and various kinds of functional membrane proteins that form a bilayer film. Other components of the cell membrane may include cholesterol, sugars and other organic species.

Although most of the specific membrane functions (such as regulated ion conduction, molecular recognition, signaling etc.) are performed by membrane proteins, a number of membrane properties (such as mechanical compressibility, defects formation, phase behavior and passive transport) are defined by the lipid bilayer. As a cell membrane is difficult to obtain in its full complexity in vitro, a lipid bilayer often serves as a model membrane in the studies of various membrane properties and functions.

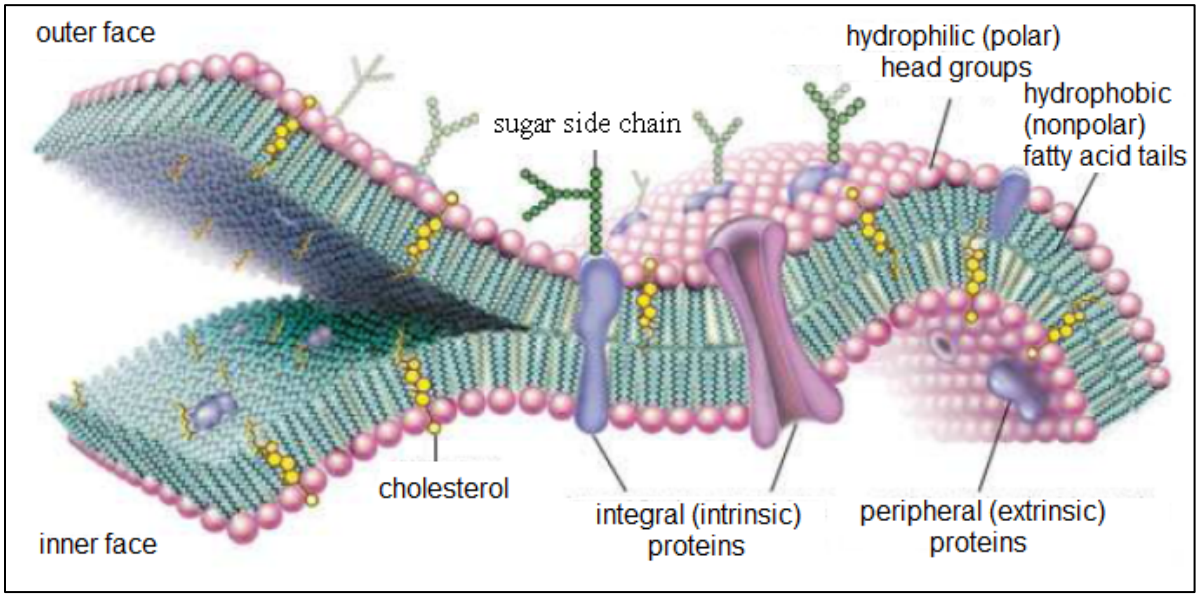

Figure 1. The fluid mosaic model of the biological membrane [1].

Lipid molecules are small amphipathic molecules, made of two major components: fatty acids and a head group. The fatty acids are the hydrophobic tails and the head group, which consists of a choline group and phosphate group, is the polar groups of the lipid molecules. There are several different types of lipids including phosphatidyleserine (PS),

phosphatidylglycerol (PG), phosphatidylcholine (PC) and phosphatidylethanolamine (PE). In the case of PS and PG lipid molecules the head group is negatively charged.

Due to their amphipathic nature, lipid molecules are able to spontaneously form lamellar structures. In the fluid state, the hydrophobic core of the lipid bilayer is about 3-5 nm thick, depending on the type of lipid molecules it contains. Other key characteristics of a lipid bilayer include the area per lipid and the order parameters of the lipid membrane. These two structural characteristics are often used to compare simulation results with experiments. For example, a DOPC (Dilauroylphosphateidylcholine) lipid bilayer has an area per lipid of 0.772 nm^2 [2] and this value can be used to validate a new force field. The order parameter is an indicator which describes the internal structure of a lipid membrane. It is also an important characteristic of a lipid membrane.

The composition of real cell membranes is complex, but quite often, in membrane studies and membrane-nanoparticle studies, the cell membrane is simplified as a pure lipid membrane, consisting of one specific lipid (usually DPPC). A similar approach will be adopted in this work.

1.2 Nanoparticles

The nanomaterials are defined as materials with one dimension that is 100 nm or less in size. Due to their small size, nanomaterials exhibit novel properties that are often vastly different from their bulk counterparts, such as high tensile strength, high electrical and thermal conductivity, and unique electronic properties, the discovery of which has led to widespread interest in their potential commercial and industrial applications. Currently, experimentists are able to synthesize different kinds of nanomaterials with different sizes,

shapes and surface properties et.al (Figure 2). Fullerenes, carbon nanotubes (CNT), metal and metal oxides and polymeric nanoparticles are the main classes of nanomaterials, which are widely investigated recently.

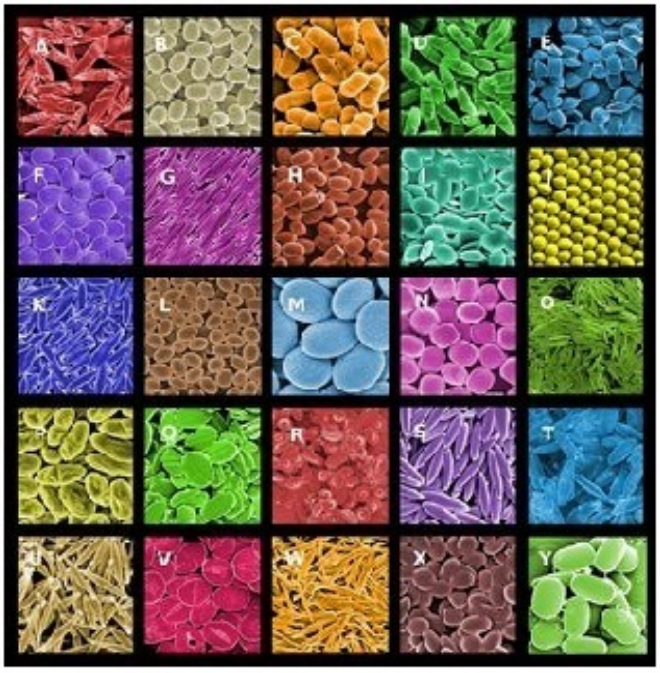

Figure 2. Figure of different kinds of nanoparticles (Figure adapted from http://phys.org/news104677694.html)

Fullerenes are closed cage structures consisting of sixty or more carbon atoms, with each carbon atom bonded to three others. Fullerenes are similar in structure to graphite but contain pentagonal rings in addition to hexagonal rings, which allow the cage to close. Surface functionalization can lead to a wide variety of fullerenes that vary in their chemical and biological properties. Contamination with solvents, amorphous carbon or other materials may also influence their chemical and biological behaviors.

Carbon nanotube (CNT) first discovered by Iijima [3], are a form of carbon that is similar in structure to C_{60} but elongated to form tubular structures in diameter. CNT can be produced with very high aspect ratios and range in length from a few micro-meters to milli-meters. Basically, there are three types of CNT: i) single-walled carbon nanotubes; ii) double-walled carbon nanotubes and iii) multi-walled carbon nanotubes. Surface functionalization can also lead to a wide variety of CNTs that vary in their chemical properties and biological activity. Also, contamination with metal catalysts, amorphous carbon or other materials may influence their behavior.

Metal and metal oxide nanoparticles are based on various elements, including gold, silver, aluminum, cobalt, copper, iron, magnesium, nickel, titanium and zinc. However, with regards to the research into the environmental and safety of these materials, studies have largely focused on a number of key substances in relation to their potential applications nowadays. For metals, the greatest number of studies has concentrated on gold and silver nanoparticles. Metal oxides, TiO_2 and ZnO nanoparticles have been widely studied due to their high utilization in products such as sunscreens. CeO_2 and SiO_2 nanoparticles have also attracted research attention due to their widespread application. For example, CeO_2 can be used as a catalyst and helps to reduce the emission of soot and SiO_2 can be used as an anti-clogging agent. As with the fullerenes and CNTs, surface modification/coatings can lead to a wide variety of metal and metal oxide particles that vary in their physico-chemical properties as well as biological activity.

For the past few decades, there has been an extensive research interest in the area of drug delivery using biodegradable polymeric nanoparticles as carriers for small molecules. These kinds of nanoparticles have been used as a physical approach to change and improve

the pharmacokinetic and pharmaco-dynamics properties of various types of drug molecules. They have been used to facilitate the drug to the specified sites, protect the drug entity and to deliver the drug at a controlled and sustained rate to the site of action. Polymeric nanoparticles offer some specific advantages. For example, nanoparticle coated with hydrophilic polymer such as PEG (Polyethylene glycol) have been used as potential drug delivery devices because of their ability to circulate for a prolonged period time targeting a particular organ and their ability to deliver proteins, peptides and genes.

1.3 Nanoparticle-membrane Interactions

In the area of biomedicine, nanoparticles are of great interest for use as imaging tools, phototherapy agents and gene delivery carriers. The interactions of nanoparticles with cell membranes are of key importance to such applications [4-6]. A big challenge is how to achieve efficient delivery to intracellular target compartments, while avoiding cytotoxicity during passage through cell membranes to reach the target [7-8]. Understanding the interaction of nanoparticles with the membrane has importance for designing medical therapeutics, as well as for predicting effects from environmental exposure [9-13]. The increasing commercial use of nanoparticles also motivates the research progress of the nanoparticle properties that are likely to yield adverse effects from environmental and human exposure.

For example, previous studies have shown that some nanoparticles penetrate the cell membranes by generating transient holes [10], which can lead to cell death due to loss of membrane polarization and/or leakage of ions and molecules into/out of the cell. In contrast, some data suggest that cell-penetrating peptides may be capable of penetrating membranes

without causing overt pore-formation in the cell membrane [5, 14-16]. Therefore, appropriate control of the nanoparticle-membrane interaction is an essential component of nanoparticle-based devices. Previous research has identified the nanoparticle properties that are predictive of membrane disruption [7, 10]. Specifically, Leroueil *et al.* and Oberdorster *et al.* have reported that nanoparticle size, surface area and net charge are the primary predictors of membrane disruption [10, 12]. At the same time, membrane binding, membrane deformation, pore formation, and ion leakage induced by nanoparticles was demonstrated in *vivo*, in *vitro*, and on phospholipid model membranes [7, 17-23].

However, previous experiments were unable to resolve the molecular-scale details of the nanoparticle-membrane interaction and some of the simple questions have not been answered yet: How do nanoparticles transport across biological membranes? What structural changes (such as thickness, order parameter and flip-flop phenomenon) occur in lipid membranes during the permeation of nanoparticles? How does water and ion leakage happen during the nanoparticle permeation? Can a lipid membrane heal itself after perturbation by nanoparticles? Due to their complexity, the study of translocation of nanoparticles through real cell membranes is inherently challenging. Therefore, there is a clear need for physical insight that can help address these and other questions. In a large context, it would be of interest to determine how the nature of such transport and the interactions between lipid membrane and nanoparticles, in particular, may determine the biocompatibility and toxicity of nanoparticles.

1.4 Molecular Modeling and Simulations of Nanoparticle Permeation

Some molecular dynamics simulations studies have been conducted on the interactions of nanoparticles and biological membranes and a number of possible mechanisms have been reported recently. Those nanoparticles include fullerenes [24-27], carbon nanotubes [28-29], bare nanoparticles [30-32] and functionalized nanoparticles [33-34]. The results from their initial studies are very promising. These theoretical studies of translocation of nanomaterials have examined various aspects of the permeation process, including altered membrane thickness around the embedded nanoparticles, the phase transformations of lipid bilayers, the structural properties of the bilayers during permeation such as average order parameters of tail, area per lipid and the thermodynamics of adsorption and penetration for nanomaterials. The effect of nanoparticle shape on its permeation through lipid bilayers using dissipative particle dynamics has also been investigated [35], in which the minimum driving forces required for various shaped nanoparticles (ellipsoids, cylinders, pushpin shapes) to translocate across the lipid bilayers was investigated. In summary, computer simulations in this field are at an early stage and many efforts are still underway to investigate the effects of nanostructured materials in biological environments.

1.5 Objectives and Scope of This Thesis

In this study, using coarse-grained molecular dynamics simulations, an effort to get insights of the permeation process of bare nanoparticles (nanocrystals) of different sizes and ligand-coated nanoparticles of different ligand through lipid membrane has been made, as well as the investigation of the nanoparticle permeation-induced water penetration, ion

transport and lipid molecule flip-flop and the compressibility of membrane under external stimuli. Short chapter summaries are given below.

Chapter 2 / Methodology: Description of the methods used in this work. An introduction to molecular dynamics simulations is given first, including inter- and intra molecular potentials, code implementation issues and different force field regimes. A description of the coarse-grained (CG) model used in this study and an example of a typical lipid membrane simulation system is provided in the second part of this chapter.

Chapter 3 / Simulation and validation of a coarse-grained lipid membrane and nanoparticles: CG-MD simulations of a lipid membrane self-assembly process and the construction of nanoparticles are reported in this chapter. The MARTINI CG force field is discussed and the comparisons of our simulation results with available experimental or atomistic simulation data are provided in this chapter.

Chapter 4 / Permeation of nanocrystals (bare nanoparticles) through a lipid membrane: CG-MD simulations of the permeation process of gold nanocrystals (bare gold nanoparticles) across a lipid membrane are reported in this chapter. Extensive MD simulations with various sizes of nanocrystals in a lipid membrane system are discussed. The nanocrystal permeation behavior is observed; the characteristics and the mechanism of the nanocrystal transportation are explored and the structural and dynamical details of the membrane during the permeation process are investigated in this chapter.

Chapter 5 / Permeation of ligand-coated nanoparticles through a lipid membrane: CG-MD simulations of the permeation process of ligand-coated gold nanoparticles across a lipid membrane are discussed in this chapter. The ligand-coated nanoparticles permeation behavior is observed and how the ligands affect the nanoparticle

permeation behaviors and the structural response of the lipid membrane are investigated in this chapter.

Chapter 6 / Nanoparticle permeation induces water penetration, ion transport and lipid molecule flip-flop: CG-MD simulations are studied to investigate the nanoparticle permeation induced water penetration, ion transport and lipid molecule flip-flop phenomenon in a lipid membrane in this chapter. The effect of ion concentration, pressure differential across the membrane, nanoparticle size and permeation velocity are examined in this chapter.

Chapter 7 / Investigation of the compressibility of a lipid membrane: CG-MD simulations are described to explore a method for calculating the compressibility of a model membrane. Comparisons of our simulation results with available experimental or atomistic simulation data are provided in this chapter, as well as the membrane behaviors prediction under conditions not studied experimentally.

Chapter 8 / Summary and Conclusions

2. METHODOLOGY

This chapter is a description of the methodology used in this work. In this thesis, molecular dynamics (MD) is used as the primary tool. Thus, in the first part of this chapter, we will introduce some basic principles of the molecular dynamics simulation technique, the molecular potentials and some implementation issues. In the second part of this chapter, we will provide different force field regimes in MD simulations. Specifically, a short description of the MARTINI coarse-grained model, the molecular mapping method and an example of a lipid molecule and a lipid membrane system will be presented in the second part of this chapter.

2.1 Fundamentals of Molecular Dynamics

Molecular dynamics is a computer based molecular modeling technique in which the equations of motion of each particle (or molecule) are solved to trace the time evolution of classical systems. It is concerned with time evolution, under the laws of classical mechanics, of systems of particles interacting via conservative forces, and is a numerical solution of the classical N-body problem. Both static and dynamic properties can be obtained by time averaging appropriate statistical mechanical expressions. MD methods can be used to study both thermodynamics and transport properties, providing access to dynamic quantities such as transport coefficients, and time correlation functions.

MD is a widely used fundamental technique for investigating dynamic systems, making important contributions in the study of liquids, surface physics, materials science and biomolecules system etc. MD allows us to study the dynamics of large macromolecules,

including biological system such as proteins, nucleic acids and membranes. For example, drug design in the pharmaceutical industry is often initiated with molecular dynamics which enables properties of a hypothetical molecule to be examined before its actual synthesis (which is far more expensive). MD represents an interface between laboratory experiments and theory, and can be understood as a “virtual experiment". The flow chart of a typical MD simulation is shown in Figure 3.

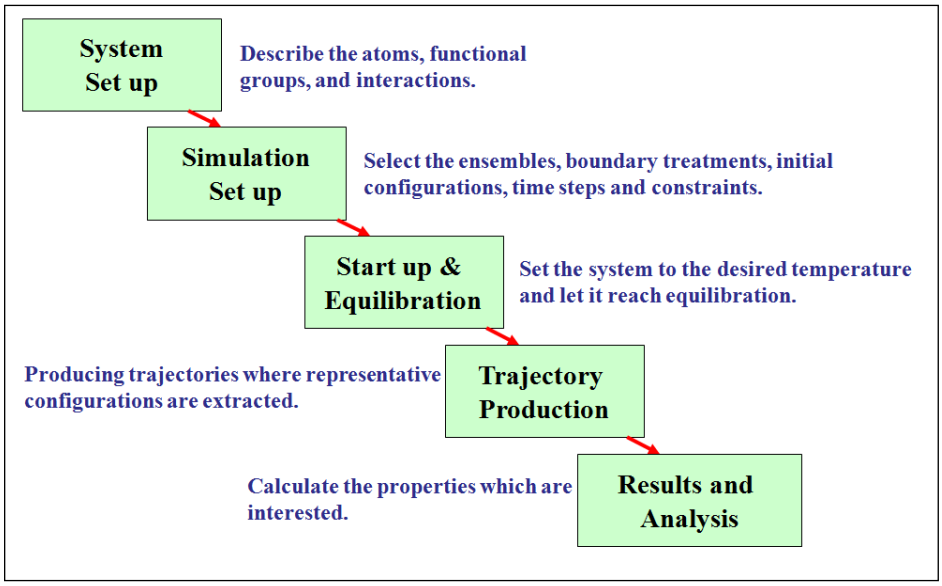

Figure 3. Flow chart of a typical molecular dynamics simulation.

2.2 Inter- and Intramolecular Potentials

Force field is a system of equations that describes the basic physical interactions in a molecular system. It can be described by the sum of intramolecular interactions, pairwise potentials, and three body potentials and so on. The force field is typically divided into bonded and nonbonded categories. Non-bonded interactions include intermolecular Van der

Waals and coulombic interactions, and usually in molecular dynamics simulations, only pairwise potentials are considered. Bonded interactions include intramolecular forces due to bond stretching, angle bending and torsions (Figure 4). The total energy of a system is given by Equation (1):

$$u_{total} = \sum_{pairs} u_{LJ} + \sum_{pairs} u_{coul} + \sum_{bonds} u_{bonds} + \sum_{angles} u_{angles} + \sum_{dihedrals} u_{dihedrals} \qquad (1)$$

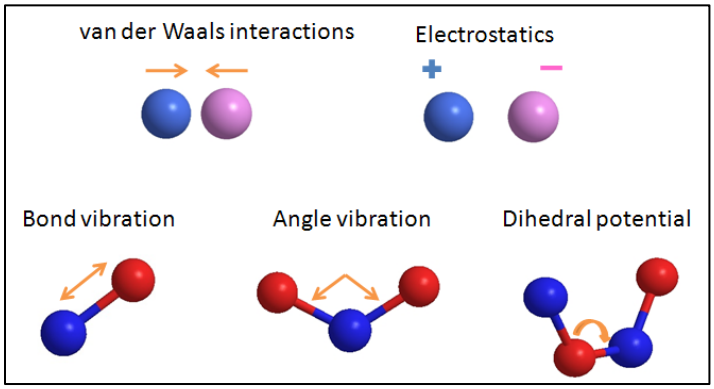

Figure 4. Examples of interactions in a force field.

2.2.1 Intermolecular Potentials

van der Waals Interactions

In order to calculate the forces on each particle of a system, one needs a description of inter-particle interactions, or potentials. One of the simplest and most widely used potentials to describe the van der Waals interactions is the Lennard-Jones (LJ) (12, 6) potential. For a pair of atoms i and j located at r_i and r_j the LJ (12, 6) potential energy is

$$u_{ij} = 4\varepsilon_{ij}[(\frac{r_{ij}}{\sigma_{ij}})^{-12} - (\frac{r_{ij}}{\sigma_{ij}})^{-6}] \tag{2}$$

where $r_{ij} = \|r_{ij}\|$, ε is the depth of the potential and σ is the collision diameter. The potential described by Equation (2) includes both a short-range, repulsive component due to electronic clouds overlap, and an attractive component due to dispersion forces.

Since intermolecular forces are necessarily conservative, the force that atom *j* exerts on atom *i* is given by

$$F_{ij} = \frac{24\varepsilon_{ij}}{\sigma_{ij}^2}[2(\frac{r_{ij}}{\sigma_{ij}})^{-14} - (\frac{r_{ij}}{\sigma_{ij}})^{-8}]r_{ij} \tag{3}$$

As can be observed from Figure 5, where the Lennard-Jones (12, 6) pair potential and pair force is shown in reduced unit (where $r^* = r/\sigma, u^* = u/\varepsilon, f^* = f\sigma/\varepsilon$), the contribution of remote particles to the total LJ-potential can be considered insignificant. We can thus neglect pair interactions beyond some cut off radius r_c in order to save computational time. However, in order to remove the energy fluctuations that occur due to the truncation of u_{ij} and force in finite systems, the shifted-force potential described by the following equation is often used:

$$u_s = \begin{cases} u_{ij}(r) - u_{rc} - (r - r_c)(\frac{du}{dr})r_c & r \le r_c \\ 0 & r > r_c \end{cases} \tag{4}$$

where in Equation (4), r_c is the cut-off distance, the common choice being 2.5σ-5.0σ, u_s is then referred to as the shifted-force potential.

Coulombic electrostatic potential

The electrostatic interaction between two molecules (or between different parts of the same molecule) is given in equation (5) by Coulomb's law:

$$u_{coul}(r_{ij}) = \frac{q_i q_j}{4\pi\varepsilon_0 r_{ij}} \tag{5}$$

where ε_0 is the permittivity in vacuum, q_i and q_j represent the charges on particles i and j respectively, and r_{ij} is the distance between particles i and j.

The Coulombic force that atom j exerts on atom i is given in equation (6),

$$F_{ij}^{coul} = \frac{q_i q_j}{4\pi\varepsilon_0 r_{ij}^2} \tag{6}$$

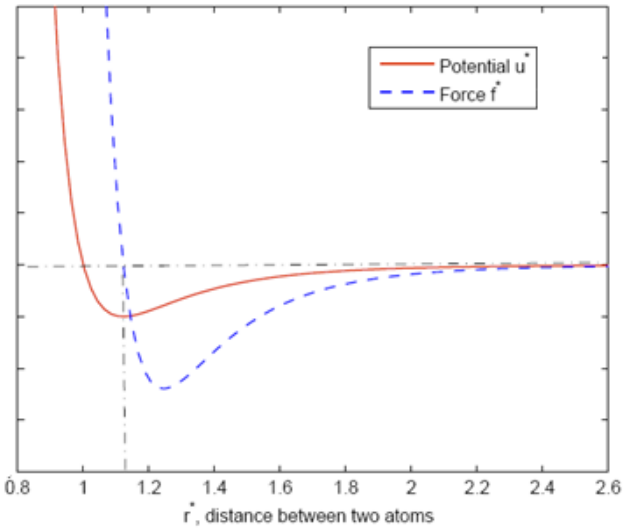

Figure 5. Lennard-Jones (12, 6) pair potential and pair force in reduced units.

2.2.2 Intramolecular Potentials

In order to describe the structure of a molecule, one uses the inter-atomic distances constrained by chemical bond lengths between two particles, the bond angles between three

particles and dihedral angles between three consecutive bond vectors. We summarize below the most common approaches for the treatment of bonded interactions.

Bond stretching

The bond length (stretching) between two particles is often modeled using a harmonic spring potential given by equation (7):

$$u_{bond}(r) = \frac{1}{2} k_b (r - r_b)^2 \tag{7}$$

where k_b is the bond force constant representing the stiffness of the bond, r_b is the equilibrium bond length and r is the distance between the two bonded atoms.

Angle bending

Angle bending, like the bond length interaction, can be represented by a harmonic potential as a function of θ, given by equation (8), which is the angle formed between three particles:

$$u_{angle}(\theta) = k_\theta (\theta - \theta_0)^2 \tag{8}$$

where k_θ is the angle force constant and θ_0 is the optimal equilibrium angle.

Torsions

The dihedral angle potentials describe the interaction arising from torsional forces between particles and they require the specification of four atomic positions. One of the mainly used expressions for the dihedral angle potential is given by equation (9):

$$u_{dihedral}(\phi) = k_\phi (1 + \cos(n\phi - \delta)) \tag{9}$$

where ϕ is the dihedral angle, k_ϕ is the dihedral force constant, n is the multiplicity, and δ is the phase of the potential.

2.3 Implementation Issues

2.3.1 Time Integration Algorithm

The time integration algorithms are based on finite difference methods. The idea behind these methods is that the time is broken down into segments, separated by a time step *dt*, creating a finite grid. At a point of this grid, corresponding to time *t*, the positions and a number of their derivatives are known (or can be calculated), and are used in order to estimate the same quantities at a time *t* + *dt* as Taylor series expansions, equation (10) to (13),

$$r(t+dt) = r(t) + dtv(t) + \frac{1}{2!}dt^2 a(t) + \frac{1}{3!}dt^3 b(t) + \frac{1}{4!}dt^4 c(t) + \ldots \tag{10}$$

$$v(t+dt) = v(t) + dta(t) + \frac{1}{2}dt^2 b(t) + \frac{1}{6}dt^3 c(t) + \ldots \tag{11}$$

$$a(t+dt) = a(t) + dtb(t) + \frac{1}{2}dt^2 c(t) + \ldots \tag{12}$$

$$b(t+dt) = b(t) + dtc(t) + \ldots \tag{13}$$

where *v* is the first derivative of the positions with respect to time (velocity), *a* is the second derivative of the positions (acceleration), *b* is the third derivative and so on.

There are several different algorithms used in molecular dynamics with the Verlet algorithm and its variations being the most widely used. The relationships used in Verlet algorithm are given in equation (14) and (15).

$$r(t+dt) = r(t) + dtv(t + \frac{1}{2}dt) \tag{14}$$

$$v(t+\frac{1}{2}dt) = v(t-\frac{1}{2}dt) + dta(t) \tag{15}$$

and it can be easily shown that the velocity is calculated by making use of the half intervals,

$$v(t) = \frac{v(t+\frac{1}{2}dt) + v(t-\frac{1}{2}dt)}{2} \tag{16}$$

Overall, in this algorithm, the velocities at $t+\frac{1}{2}dt$ are calculated from the velocities at $t-\frac{1}{2}dt$ and the accelerations at t. From the calculated velocities and the position at time t, the new positions at $t+dt$ are estimated.

2.3.2 Periodic Boundary Conditions

In the majority of the applications of MD simulations, in order to get a realistic view of a phenomenon, one would like to be able to treat the system as an infinite system and not a simulation cell of limited dimensions. In order to achieve this 'bulk' behavior of the system, a technique known as periodic boundary conditions (PBC) is used. In this technique, the single simulation cell is infinitely replicated in the three Cartesian dimensions.

The most important feature of PBC is that every particle can interact not only with the particles that are already in the simulation cell, but also with the ones located in the neighboring cells. This way, any surface effects due to the finite dimensions of the cell are minimized. However, with the PBC there could be effects associated with the artificial periodicity of the system. Also, any movement of a particle outside the cell does not affect

its interaction with the particles close to it, as the particle 'leaves' the cell and re-enters to it from the opposite side (Figure 6).

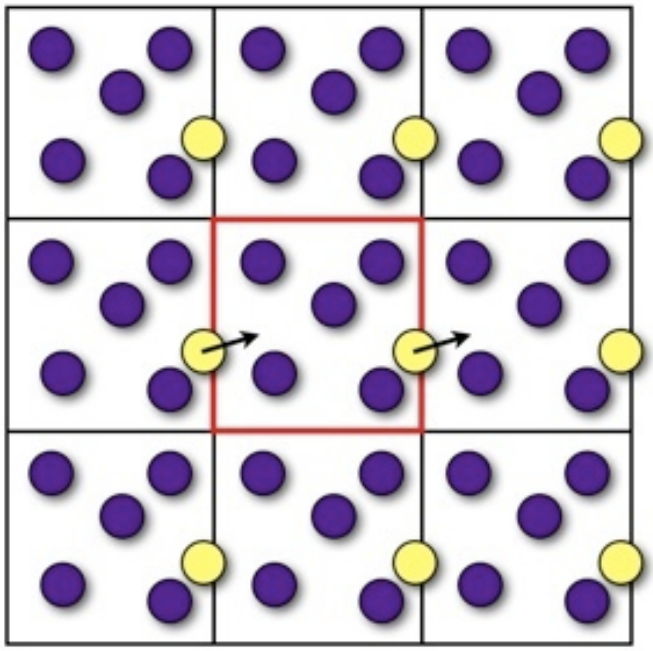

Figure 6. A two dimensional representation of the periodic boundary conditions (http://matdl.org/matdlwiki/index.php/softmatter:Periodic_boundary_conditions).

In the minimum image convention, every particle *i* interacts only with the closest image of particle *j*. There are some assumptions to be made so that this condition holds. As described before, a usual treatment for a potential is to neglect all the interactions after a cut-off distance r_c between two particles. If now we assume that the simulation cell is larger than $2r_c$, it is clear that under these conditions there is at most one pair formed by particle *i* in the cell and all the images of a particle *j*.

2.3.3 Neighbor List

Neighbor list is a method used in combination with cut-off for the calculation of interactions between particles. In addition to a cut-off radius r_c, another radius r_n, larger than r_c, is defined. This radius is used for the creation of a 'neighbor list' that includes the atoms that are located at a distance smaller than r_n. In the calculation of short range interactions, only the particles in each particle's neighbor list are considered. While the simulation proceeds, particles move in or out of the boundaries of r_n. It is thus necessary that the neighbor list is updated regularly throughout the simulation. In order for this to be done periodically and not at each step, r_n should be chosen so that the difference r_n - r_c is large enough.

It is also important to note here, that the neighbor list method leads to a noticeable speedup in the calculation of the forces, as the time to examine all pair separations in a system of N particles is proportional to N^2 and this calculation is avoided between the updates of the list.

2.4 Different Force Field Regimes: First Principle, All atom, United Atom, and Coarse-grained Site

Molecular mechanics force fields, designed for accurately predicting structures and properties, usually include many terms. Quantum mechanical calculations usually provide the most detailed molecular force fields. Comparison of simulation results with thermo physical properties and vibration frequencies is invaluable in force field development and refinement. A separate family of force fields, such as CHARMM [36] and OPLS [37] are geared more towards larger molecules in condensed phases. More approximate potentials

have also been constructed in which the CH_2 and CH_3 units are represented by single "united atoms". These potentials are typically less accurate and less transferable than the explicit atom potentials, but significantly less expensive [38]. For more complicated molecules this approach may need to be modified further. For example, in polymer simulations, there is frequently a need to economize further and coarse-grain the interactions more dramatically. Significant progress has been made in recent years in approaching such problems systematically [39].

Atomistic simulations reveal more details but are restricted to small length and time scales. MD simulations on very large systems may require computer resources that they cannot easily be available for traditional all-atom methods. Similarly, simulations of processes that are long timescales can become prohibitively expensive. Therefore, more computational efficient simulation models are required to fully investigate such larger system over longer time scales in coarse-grained (CG) models, instead of explicitly representing every atom of the system, small groups of atoms are represented as a single interactive site (pseudo-atoms). In these cases, one can sometimes tackle the problem by using reduced representations. CG models are becoming increasingly popular to study large biological systems of lipids and surfactants and gaining widespread usage in the polymer and biophysical communities.

2.5 The MARTINI Coarse-grained Model

2.5.1 Molecular Mapping and Interaction Sites

In the studies presented in this thesis, the membranes are described using the model proposed by Marrink and co-workers, called MARTINI force field [40-41]. The MARTINI

field was developed in an effort to expand an already successful coarse-grained protocol for membranes and proteins [42]. In the following sections, we will present a general description of the model and force field parameters, and also focus on the representations and parameters used for the modeling of lipid membranes. In MARTINI, basically every four heavy atoms are represented by one interactive site. There are four main types of beads representing different levels of interaction: polar (P), apolar (C), nonpolar (N), and charged (Q). Under the main types, each bead is assigned a further subtype, in order to describe more accurately the overall chemical nature of the represented group of atoms. In this description, hydrogen-bonding capability (d=donor,a=acceptor, da=both and 0=none) and different levels of polarity (from 1=low polarity, to 5=high polarity) are included. All the beads are assigned a mass of m=72 amu for reasons of computational efficiency (for the beads that take part in ring structures this value is equal to 45 amu). The mapping of a coarse-grained water site (P_4) is shown in Figure 7.

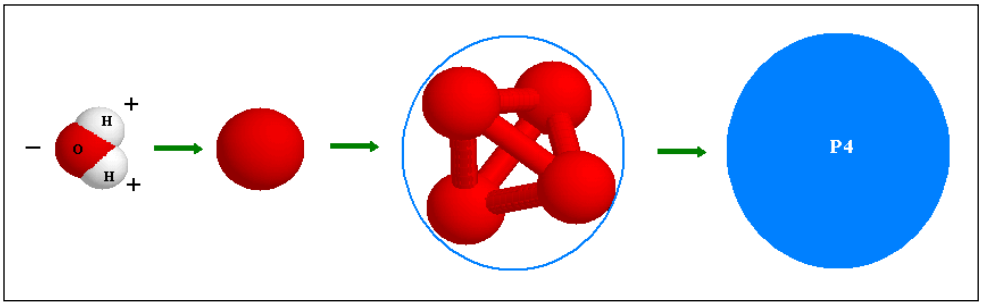

Figure 7. Coarse-grained mapping strategy for water molecules.

2.5.2 The Molecular Force Field

In MARTINI, the van der Waals interactions are described using a shifted Lennard-Jones 12-6 potential. An effective size of σ=0.47 nm is used (σ=0.43 nm, for the ring like structures and σ=0.62 nm for the super repulsive interaction). Ten different values of the characteristic energy ε are available to represent the interactions among various bead types. In Tables 1 and 2, we show present the different levels of interactions and a bead-bead interaction matrix. More details can be found in the original publication [41]. The charged particles interact through a Coulombic potential energy with a relative dielectric constant ε_{rel} = 20.

For both van der Waals and Coulombic interactions a cut-off of 1.2 nm is used. A shift to zero is also used between 0.9 and 1.2 nm in the case of van der Waals interactions and between 0 and 1.2 nm for the electrostatic interactions. Moreover, in MARTINI, the bonds between the CG sites are described by a harmonic spring potential. For the description of angles a harmonic cosine potential is used. More detailed description of the force field parameters can also be found in the original publication [41].

Table 1. Levels of interaction in the MARTINI Force Field (Same as in [41]).

	Description	ε_{ij} (kJ/mol)	σ (nm)
O	Supra attractive	5.6	0.47
I	Attractive	5.0	0.47
II	Almost attractive	4.5	0.47
III	Semi attractive	4.0	0.47
IV	Intermediate	3.5	0.47
V	Almost intermediate	3.1	0.47
VI	Semi repulsive	2.7	0.47
VII	Almost repulsive	2.3	0.47
VIII	Repulsive	2.0	0.47
IX	Super repulsive	2.0	0.62

Table 2. Interaction matrix in the MARTINI force field.

		Q				P					N				C				
		da	d	a	0	5	4	3	2	1	da	d	a	0	5	4	3	2	1
Q	da	O	O	O	II	O	O	O	I	I	I	I	I	IV	V	VI	VII	IX	IX
	d	O	I	O	II	O	O	O	I	I	I	III	I	IV	V	VI	VII	IX	IX
	a	O	O	I	II	O	O	O	I	I	I	I	III	IV	V	VI	VII	IX	IX
	0	II	II	II	IV	I	O	I	II	III	III	III	III	IV	V	VI	VII	IX	IX
P	5	O	O	O	I	O	O	O	O	O	I	I	I	IV	V	VI	VI	VII	VIII
	4	O	O	O	O	O	I	I	II	II	III	III	III	IV	V	VI	VI	VII	VIII
	3	O	O	O	I	O	I	I	II	II	II	II	II	IV	IV	V	V	VVI	VII
	2	I	I	I	II	O	II	II	II	II	II	II	II	III	IV	IV	V	VI	VII
	1	I	I	I	III	O	II	II	II	II	II	II	II	III	IV	IV	IV	V	VI
N	da	I	I	I	III	I	III	II	II	II	II	II	II	IV	IV	V	VI	VI	VI
	d	I	III	I	III	I	III	II	II	II	II	III	II	IV	IV	V	VI	VI	VI
	a	I	I	III	III	I	III	II	II	II	II	II	III	IV	IV	V	VI	VI	VI
	0	IV	IV	IV	IV	IV	IV	IV	III	III	IV	IV	IV	IV	IV	IV	IV	V	VI
C	5	V	V	V	V	V	V	IV	IV	IV	IV	IV	IV	IV	IV	IV	IV	V	V
	4	VI	VI	VI	VI	VI	VI	V	IV	IV	V	V	V	IV	IV	IV	IV	V	V
	3	VII	VII	VII	VII	VI	VI	V	V	IV	VI	VI	VI	IV	IV	IV	IV	IV	IV
	2	IX	IX	IX	IX	VII	VII	VI	VI	V	VI	VI	VI	V	V	V	IV	IV	IV
	1	IX	IX	IX	IX	VIII	VIII	VII	VII	VII	VI	VI	VI	VI	V	V	IV	IV	IV

2.5.3 A Coarse-grained Description of a Lipid Membrane System

The membrane and nanoparticles used in the coarse-grained simulations of this thesis have been represented with the MARTINI force field. As described in the introduction, a membrane is composed mainly of lipids and proteins. For reasons of simplicity, we will represent the model membrane as a lipid bilayer, without undervaluing the importance of membrane proteins in the overall functionality of a cell membrane.

The atomistic and coarse-grained representations of a DPPC (Dipalmitoylphosphatidylcholine) lipid molecule and its mapping strategy are shown in Figure 8. The lipid tails are represented as C1-type beads, the glycerol group as Na-type, the phosphate group as Qa-type and the choline group as Q0-type beads. There are 130 atoms in the atomistic model, while there are only 12 interactive sites in the coarse-grained model. The system of equilibrated lipid bilayer in the water environment is shown in Figure 9.

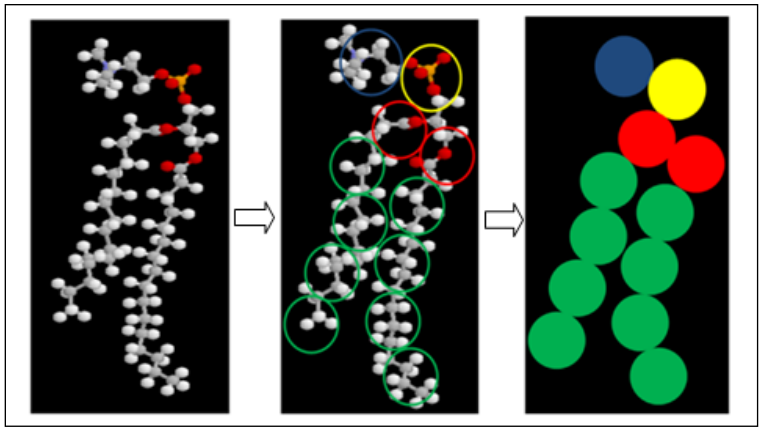

Figure 8. Coarse-grained mapping strategy of a DPPC lipid molecule.

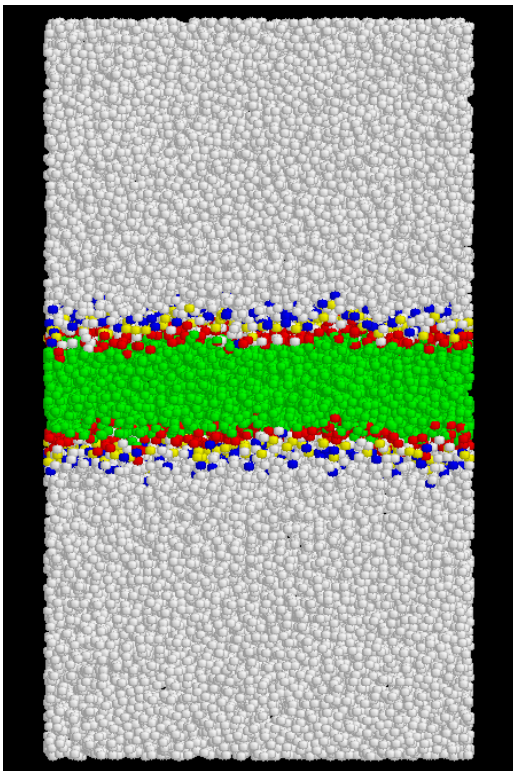

Figure 9. Coarse-grained representation of a lipid membrane/water system.

3 SIMULATION AND VALIDATION OF A COARSE-GRAINED LIPID MEMBRANE AND NANOPARTICES

In Chapter 1 and 2, we have introduced the biological background and the method of coarse-grained molecular dynamics simulation. In this chapter, we will focus on the simulation and validation of the system used in our studies, including the lipid membrane system, nanocrystals (bare nanoparticles) and ligand-coated nanoparticles, based on the MARTINI force field. We will elaborate on how we obtained the lipid membrane from self-assembly of the lipid molecules how we constructed the nanoparticles. Also, we provide a more detailed description of the tests (dynamical and structural properties) we have done for the validation of the lipid membrane system and the nanoparticles and demonstrate the effectiveness of the MARTINI force field in this work.

3.1 Introduction

Lipid membranes provide the basic structural unit of living cells, and knowledge of their physical and chemical properties is very important for our understanding of how the whole cell functions. Fully atomistic molecular dynamics simulations of lipid membranes have become feasible in the last few years [43-47]. There is, however, very time consuming even if a small fragment of membrane is considered. An often used way to reduce computer time for simulations of large molecular systems in cases when all-atomic resolution is not principally important is to use coarse-grained models. Coarse-grained lipid model allow simulations of bigger membrane fragments for longer time while preserving many properties of all-atomic model. This allows us to address a much wider range of problems.

In the past few years, a number of coarse-grained lipid model with different levels of details have appeared [40, 48-50]. In this study, we use MARTINI coarse-grained model, which is one of the most popular models for molecular dynamics simulations of biomolecular systems.

Metal nanoparticles, bare or capped with organic adsorbents and assembled into various nanoparticles, have a strong potential for the development of new materials for nanotechnology [51-53]. Chemical control over nanoparticles size, shape, and composition presents one the major challenges in this area, because these parameters govern many thermodynamic, optical, and chemical properties of such nanoparticles [54-56]. Several approaches have been reported for manipulating the properties of metal nanoparticles, among which control over chemical properties of capping agent, such as modification of surface-stabilizing groups or alkyl chain length, were applied [57-59]. Like the lipid membranes, there has been significant progress in using atomistic and coarse-grained molecular dynamics for investigating structural and dynamics of nanoparticles [60-62]. The MD simulations have also been applied for examining ligand shell organization in self-assembled monolayers at nanoparticle surfaces [63]. The structural and thermal properties of the DNA-functionalized and DNA linked particles have been modeled using both atomistic and coarse-grained methodology [64].

There is increasing interest in using gold nanoparticles as attractive nanoparticles for biological and biomedical applications, such as bio-imaging, single molecule tracking, drug delivery and diagnostic purposes. For example, gold nanoparticles can be engineered to accumulate preferentially in tumor cells using properly functionalized targeting ligands, thus providing an effective tool for cancer diagnosis and therapy [18]. These experiments

motivate our work to use gold nanoparticles as our model nanoparticles. In this study, we start with gold nanocrystals (bare gold nanoparticles) and attach various lengths of alkyl chain ligand onto the surface of gold nanocrystals to construct the uncharged ligand-coated gold nanoparticles. MARTINI coarse-grained model is also applied in mapping the ligands.

3.2 Lipid Membrane

3.2.1 Lipid Membrane Self-Assembly Process

The model membrane in the present work consists of DPPC (C_{16}) lipid bilayer. The detail of the neutral DPPC (C_{16}) molecular structure is shown in Figure 10 and the coarse-grained mapping has been shown in Figure 8 in the last chapter.

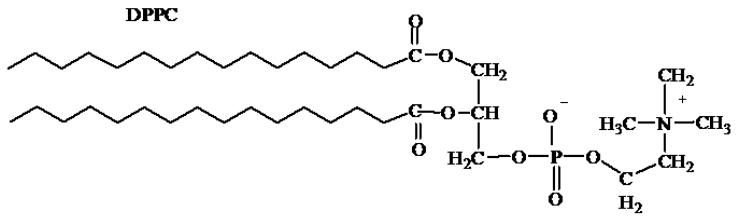

Figure 10. Structure of dipalmitoylphosphatidylcholine (DPPC) (C_{16}) molecule.

The initial configuration of the lipid bilayer system comes from the self-assembly process of the lipid membrane with 128 DPPC molecules and 2000 water molecules, starting from random orientations and positions [65] under periodic boundary conditions. Constant temperature and constant pressure Nose-Hoover molecular dynamics algorithm (NPT ensemble) was used with the temperature 323 K and pressure 1 atm. All the

simulations were performed using the LAMMPS (Large-scale Atomic/Molecular Massively Parallel Simulator) simulation package. A time step of 10 fs is used in the simulations.

A series of snapshots of 100 ns MD runs is shown in Figure 11, which clearly shows that a lipid bilayer membrane form spontaneously quickly at the end of the simulation.

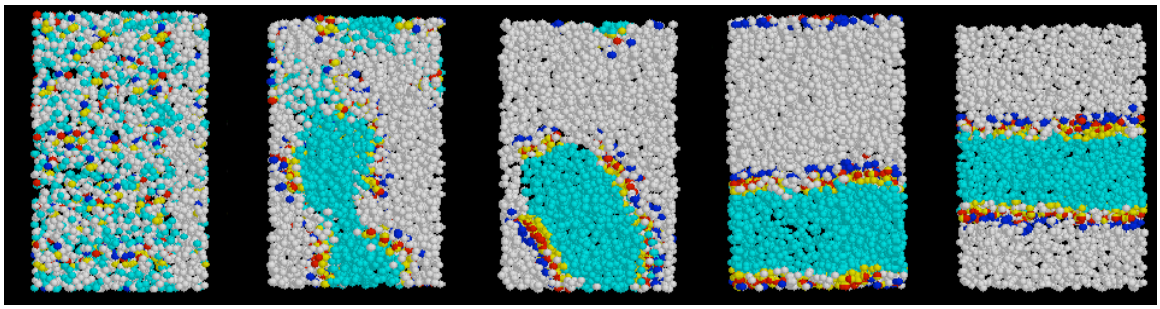

Figure 11. Snapshots of lipid membrane self-assembly process.

3.2.2 Validation of Equilibrated Lipid Membrane/Water System

To validate the MARTINI force field used in this study, we carried out a simulation for lipid membrane/water system first with comprehensive series of tests before introducing the nanoparticles. We used an extended water region to allow for the inclusion of the nanoparticles. The lipid membrane/water system under these tests consists of 128 DPPC molecules and 3764 CG waters in a $6.3 \times 6.5 \times 15.5$ nm^3 simulation box.

A range of properties of this lipid membrane was examined in the present work. Important quantities characterizing a lipid bilayer membrane include the thickness of the membrane, the surface area per lipid and the tail segment order parameter. The density profile of each component of the DPPC membrane was obtained during the simulation, which is shown in Figure 12, from which we obtained the distance between the phosphate

groups as 3.79 nm, in close agreement with the experimental value of 3.85 nm [66]. The area per lipid of the DPPC membrane was found to be 0.6308 nm^2 in our simulation (Figure 13), which also agrees well with the experimental values, which lie in the range 0.629 ± 0.013 nm^2 at 323 K [67].

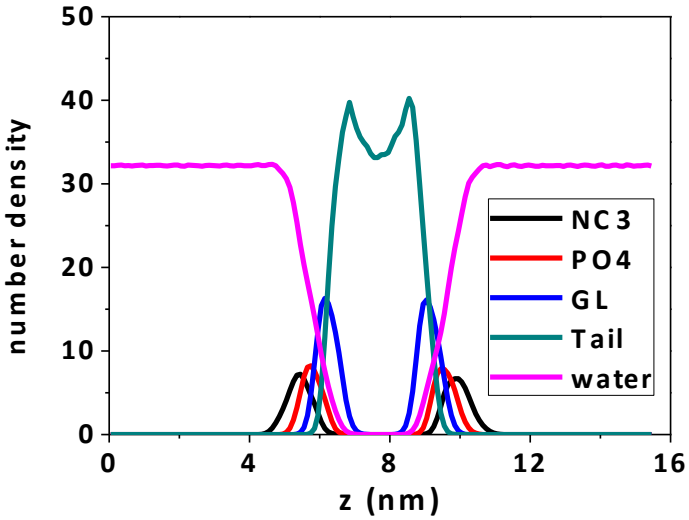

Figure 12. Density profile of components of DPPC membrane along the z direction, (NC_3 represents the choline group, PO_4 the phosphate group, while GL represents the glycerol backbone).

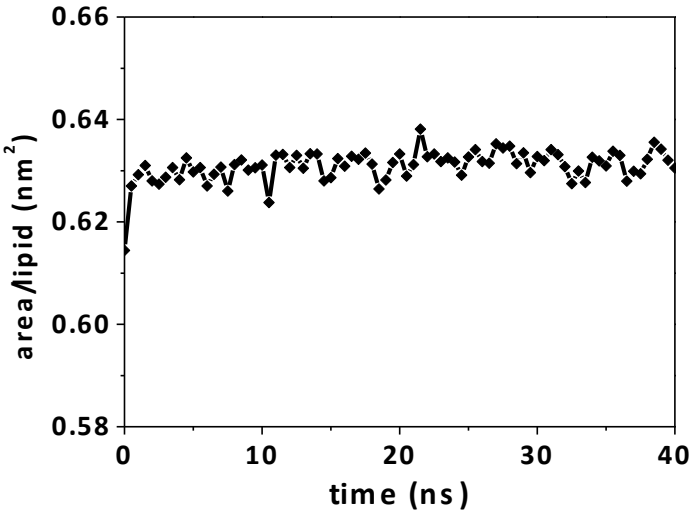

Figure 13. Area per lipid for the DPPC lipid membrane for 40 ns.

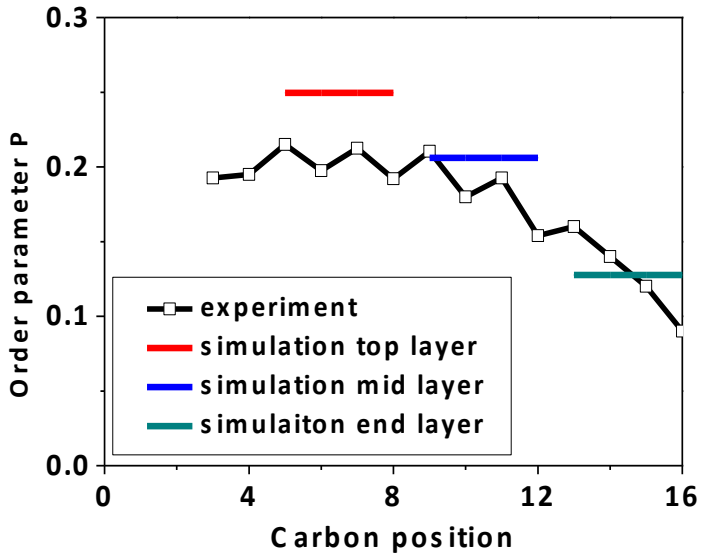

Figure 14. Comparison of tail segment order parameter with experimental measurements [68].

The conformation of the hydrocarbon tails of the lipid is another important property for lipid bilayers. Generally, the conformation and orientation of lipid hydrocarbon tails are highly disordered. A measure of the internal order of a lipid bilayer is the order parameter P,

$$P = \left\langle \frac{3\cos^2\theta - 1}{2} \right\rangle \tag{17}$$

where θ is the angle between the bond and the axis normal to the lipid bilayer [68]. P=1 implies perfect alignment, P=-0.5 anti alignment, and P=0 random orientation. Because we use a coarse-grained scheme, only a limited number of indicators of internal order may be obtained from the simulation. Although we cannot compare directly with C_{n-1}-C_n order parameters derived from experiment and all-atoms simulations, the order parameters can be derived for the four sites that constitute the tail forming three 'bonds' between them and the order parameters for these 'bonds' can be compared with experiments effectively. From the

results shown in Figure 14, we see that our model reproduces the correct trends qualitatively, with our model showing somewhat higher order near the head than the actual DPPC lipid bilayer.

In summary, our simulation results are in reasonable agreement with available experimental results, which validate the effectiveness of the coarse-grained model we are using for the lipid bilayers.

3.2 Bare Gold Nanoparticles (Gold Nanocrystals)

3.2.1 Structure of Gold Nanocrystals

Gold nanocrystals have been demonstrated to have a stable structure that is close to a face-centered-cubic (FCC) structure [69-72] with nearly spherical shape, which corresponds to the nanoparticle, used in this study. In the present work, the structure of the gold nanocrystal was obtained by cutting nearly spherical nanocrystals out of a bulk gold FCC lattice, with various diameters from 0.8 nm to 2.5 nm. Some of the structures of gold nanocrystals in our simulation are shown in Figure 15.

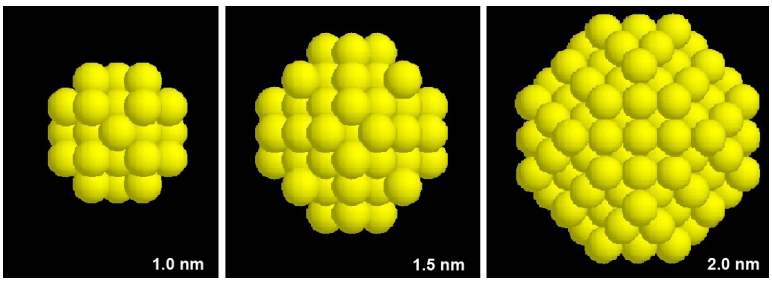

Figure 15. The structure of gold nanocrystals (bare gold nanoparticles) with diameter of 1.0 nm, 1.5 nm and 2.0 nm.

3.2.2 Potential Model for Gold Nanocrystals

The interaction between the gold atoms is also described by Lennard-Jones potentials. Various potential parameters have been used previously for gold atoms, from All-Atoms [64, 70, 73-74] to Coarse-grained (atomistic structure but modeling gold atoms as C-class [33], P-class [75] using MARTINI force fields). Li *et al.* [30] and Lin *et al* [76] have used C-Class and N-Class parameters to investigate the hydrophobicity and size effect of model nanoparticles interacting with lipid membrane. The parameters we used for gold nanocrystals permeation are from All-Atoms simulation in ref. [64, 73], and are listed in Table 3. For the cross-interactions between gold atom sites and lipid/water sites, we use the standard Lorentz-Berthelot mixing rules [77] as a starting point in this study. Several previous studies have shown that AA and CG models can be combined in simulations successfully. Such studies include simulating membrane-bound ion channels [78] and lubricated contact between two planar solid substrates that sandwich a soft film; the results obtained agreed with previous all atom studies [79-80].

Table 3: Potential parameters of gold nanocrystals

Atoms	σ (nm)	ε (KJ/mol)
Au	0.2569	44.19

We also carried out a study with a CG model for the nanocrystal investigated to determine if that would have a significant effect on the permeations being examined in this study. Figure 16 shows a comparison of the results obtained for the permeation velocity

using the CG and AA models for nanocrystals. The permeation velocity obtained for an external force of 170 pN for a 1.0 nm nanocrystal permeation is shown in Figure 16. As can be clearly seen both the CG and AA models exhibit almost identical behavior. The CG model for the nanocrystal had a value of $\sigma_{CG} = 1.2$ nm and $\varepsilon_{CG} = 3.2\ \varepsilon_{AA}$.

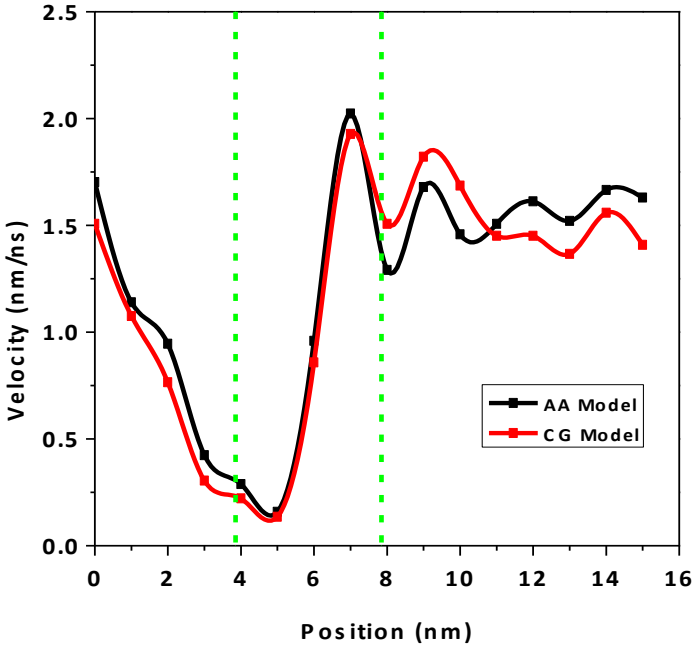

Figure 16: A comparison of velocity profiles of a nanocrystal (modeled using either a AA or CG model) permeating the lipid bilayer membranes.

3.3 Ligand-coated Nanoparticles

3.3.1 Simulations of Ligand-coated Nanoparticles in Solution

As shown in section 3.2, the structure of the gold nanocrystal (nanoparticle without ligands (AuNP_bare)) is obtained by cutting a nearly spherical nanocrystal out of a bulk face-centered-cubic (FCC) structure gold lattice. For the ligand-coated nanoparticles study, we fix the size of gold core as 2.1 nm in the diameter and attach ligands to the surface of

gold nanocrystals by the following procedure: we first put the nanocrystal in the center of a 12.0×12.0×12.0 nm^3 simulation box and fill the box with butanethiol ligands in large excess compared to the number required to form a compact monolayer. A cycled annealing simulation procedure was then followed to condense the ligands onto the surface of the nanocrystal, which is a method also reported by Luedtke *et al.* [81] using atomistic simulations. The temperature was increased from 200 K to 500 K subsequently and then cycled between these temperatures to allow desorption of excess ligand molecules and exploration of stable binding sites. The final number of the equilibrated butanethiol chains on the gold core is 87, yielding a thiolate per surface gold atom coverage of 48.3% (17.9 nm^{-3} in ligand density), which is in the range of experimental coverage measurements, up to 52 ~ 57% for 2.1 nm diameter alkanethiolate gold nanoparticles [82].

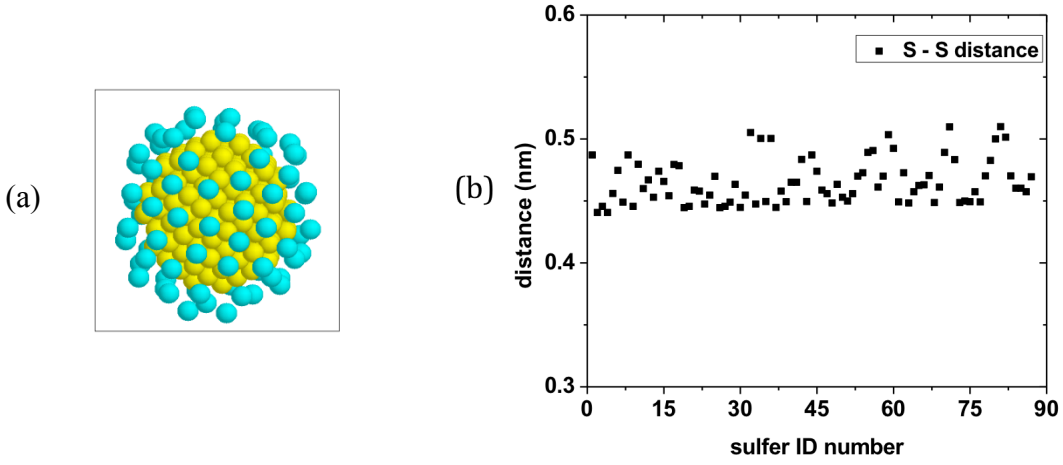

Figure 17. Distribution of surface sulfur atoms (a) and the distance between sulfur-sulfur atoms on the gold core (b).

As shown in Figure 17(a), after the annealing process, the surface sulfur atoms for the nanoparticles are uniformly distributed and the distances between sulfur atoms are in the range of 0.44 ~ 0.51 nm (Figure 17(b)). For studies using variable ligand lengths, the butanethiol ligands (AuNP_SL) are replaced by $R=(CH_2)_8$ and $R=(CH_2)_{12}$ to form gold nanoparticles with uncharged hydrophobic ligands of medium length (AuNP_ML) and long length (AuNP_LL), shown in Figure 18(a).

The 2.1 nm diameter gold nanoparticle used here is smaller than typically used in biomedical application. A wide range of sizes of gold nanoparticles has been studied experimentally for drug delivery and as imaging agents. A size of 1-100 nm or more is easily achieved [83] experimentally. For example, PEG-coated gold nanoparticles (4 nm and 100 nm) have been administered intravenously to mice [84]. Pan *et al.* have investigated the size dependence of the cell toxicity of water-soluble gold nanoparticles ranging from 0.8 to 1.5 nm in diameter in four cell lines and find that all prove most sensitive to gold particles 1.4 nm in size [85]. Hainfeld [86] used gold nanoparticles 1.9 nm in size for imaging in mice. Thus, our 2.1 nm nanoparticles, although small, are of a practically relevant size. Gold nanoparticles used for biomedical applications (gene and drug delivery) are typically larger (20-100 nm) because they are conjugated with various biomolecules or drugs and these sizes are known to cross cell membranes effectively using other mechanisms such as endocytosis, which is not studied in our work [87-89].

In our simulations, the atomistic to coarse-grained mapping strategy is as follows: the gold and sulfur atoms are mapped 1:1 and are fixed rigid and the residues of alkyl chains are 4:1 mapped and flexible (see Figure 18(b)).

(a)

(b)

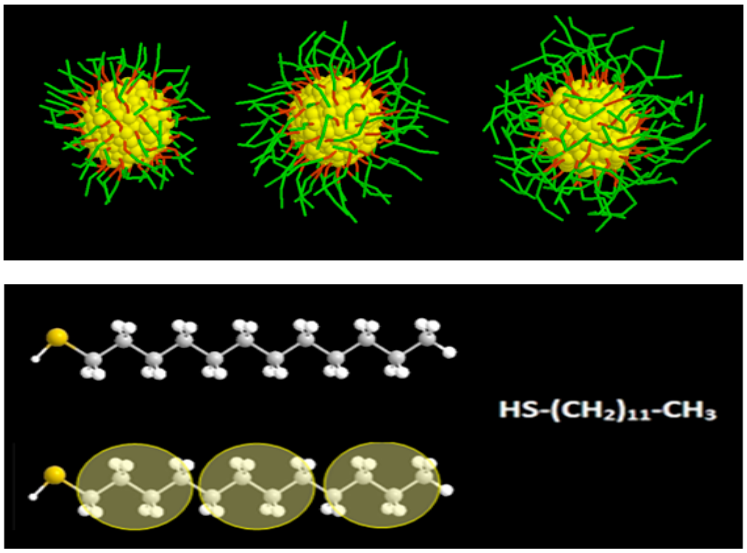

Figure 18. The structure of the ligand-coated gold nanoparticles. (a) The residues are replaced by $R=(CH_2)_n$ to form nanoparticles; shown here are structures for n=4, 8, 12 from left to right; (b) The structure of one alkyl residue and the coarse-grained mapping strategy from atomistic sites to coarse-grained sites.

The interaction between the gold nanoparticle and lipid molecules is described by L-J potentials. For ligand-coated nanoparticles study, since the gold core is embedded inside the nanoparticles, the distance between its surface and the water environment is larger than the cut-off distance, the potential of gold atoms is relatively insignificant. Here, we assign MARTINI C5 type interaction sites for gold atoms, N0 type for sulfur atoms and C1 type for alkyl chains in MARTINI. The classes of interaction sites and their accompanying potential parameters have previously been tested and verified against atomistic simulations by Marrink et al. [41] and we have tested them in our simulation systems against experimental data for lipid membranes shown in section 3.1. The non-bond and bond parameters for the ligands of gold nanoparticles are shown in Table 4. For the cross-interactions between gold nanoparticles and lipid/water sites, we used the standard Lorentz-Berthelot mixing rules as a starting point in this study [77].

Table 4. Nanoparticle force field
(R_0 in nm, K_{bond} in kJ mol^{-1} nm^{-2}, Θ_0 in deg, K_{angle} in kJ mol^{-1} rad^{-2})

Non-bond		Bond			Angle		
Interaction site	Type[(a)]	Connecting block	R_0	K_{bond}	Connecting block	Θ_0	K_{angle}
Au	C5	Au-S	0.445	1250	Au-S-Ligand	180	25
S	N0	S-Ligand	0.445	1250	S-Ligand-Ligand	180	25
Ligand	C1	Ligand-Ligand	0.47	1250	Ligand-LigandLigand	180	25

(a)MARTINI classification

3.3.2 Model Validation for Ligand-coated Gold Nanoparticles in Solution

A range of properties of ligand-coated gold nanoparticles was examined to validate the effectiveness of the model we have adopted for the gold nanoparticles. A 10.8×10.8×10.8 nm^3 simulation box is created with explicit solvent and a gold nanoparticle is placed at the center. First, we calculate the nanoparticle radius of gyration by letting each gold nanoparticle dissolve in hexane solution at 300 K. Two C1 beads having a 0.47 nm harmonic bond between them represent the CG hexane. The particle-solvent system was equilibrated for 20 ns with a time step of 10 fs and the radius of gyration is averaged every 400 ps. Secondly, we calculate the nanoparticle diffusion coefficient by letting each nanoparticle insert into a $CDCl_3$ solution. A C4 bead represents the CG $CDCl_3$ and the simulation setup is identical to the above case. The diffusion coefficient is obtained from the long-time slopes of mean square displacements.

The nanoparticle radius of gyration and the diffusion coefficient for AuNP_ML and AuNP_LL nanoparticles, which are shown in Table 5 and Table 6, are consistent with Lin's coarse-grained simulation report [33]. We also notice that the radius of gyration of our nanoparticles is slightly higher than the experimental measurements, concomitant with a smaller diffusion coefficient in $CDCl_3$ solution compared to the experimental value. These

results are consistent with each other because a larger gyration radius will induce more friction in the solution, thus having a retarding effect on the diffusion. In summary, our simulation results are in reasonable agreement with available experimental results, which validate the effectiveness of the coarse-grained model we are using for the ligand-coated gold nanoparticles. The models described in this chapter have been applied to obtain the results described in the following chapters.

Table 5. Comparison of radius of gyration of the CG gold nanoparticles with simulation reports and experimental measurements

Ligand	Radius of gyration (nm) in hexane		
	Simulation[(a)]	Simulation	Experiment
HS-$(CH_2)_7$-CH_3	0.991		
HS-$(CH_2)_{11}$-CH_3	1.138	1.145 ± 0.004	0.924 ± 0.005

(a) This work

Table 6. Comparison of diffusion coefficient of the CG gold nanoparticles with simulation reports and experimental measurements

Ligand	Diffusion coefficient (10^{-6} cm^2/s)		
	Simulation[(a)]	Simulation	Experiment
HS-$(CH_2)_7$-CH_3	1.310	1.333 ± 0.25	2.6 ± 0.3
HS-$(CH_2)_{11}$-CH_3	1.073	0.918 ± 0.04	2.3 ± 0.2

(a) This work

4 PERMEATION OF NANOCRYSTALS (BARE NANOPARTICLES) THROUGH A LIPID MEMBRANE

It has been shown that the interaction between lipid membranes and nanoparticles and the disruption of lipid membranes are often determined by physicochemical properties of nanoparticles, such as size, shape and surface composition. In this chapter, we employ CG-MD simulations and start with gold nanocrystals (bare gold nanoparticles) as a probe to explore the permeation process of nanocrystals across a DPPC lipid membrane. An external driving force is applied to aid the permeation of various sizes of the gold nanocrystals across the lipid bilayer. The minimum forces needed to penetrate the membrane and the interaction of nanocrystals and lipid bilayers are investigated in our simulations. The elastic and dynamic properties of lipid bilayers, including the local and bulk properties under nanocrystal permeation, which are of considerable fundamental interest, are also investigated in this chapter.

4.1 Introduction

Biological membranes are one of the major structural elements of cells, which play a key role as a selective barrier and substrate for many proteins that facilitate transport and signaling processes. These selective permeable membranes define the boundary and maintain the essential intracellular environment of the cell. Transport of chemical species across biological membranes is of significance in separations, biosensors, pharmacological applications and drug delivery systems. Small molecules such as Xe, O_2 and CO_2 can diffuse

across the cell membranes passively; however, ions, such as Na^+, Ca^{2+}, Cl^-, and larger molecules may not easily cross the cell membranes on their own [90].

Interactions and processes in biological systems involve inherently nanoscale objects; so engineered nanoscale materials allow the possibility of affecting biological processes at a fundamental level. At the same time, the ability of these nanoscale particles to enter and be transported within biological bodies in ways that larger particles cannot, could have adverse toxicity effects [91-93]. Recently, much effort has been focused on interactions between nanoparticles and lipid membranes, experimentally [88, 94-96] and theoretically [24, 30, 33, 35, 97-99]. Investigation of nanoparticles biocompatibility and toxicity has been a growing interest in addressing the impact of nanotechnology on human health and the life environment [100-103]. Therefore, there is a clear need for physical insight into the questions regarding the permeation process of nanoparticles across simpler model membranes, such as lipid bilayers, which can provide some understanding of membrane structural changes during the permeation, in general, and how the nature of the interactions between lipid membrane and chemical species on the surface of the core particle, in particular, determines the details of membrane penetration by nanoparticles.

In previous studies on the small molecule transport across the lipid bilayer membranes, we have successfully studied small molecules, with permeability results in satisfactory agreement with experimental results [65, 104]. We used a coarse-grained model to simulate the gas permeation through pure DPPC lipid bilayers [104] and DPPC lipid bilayers with Outer Membrane Protein A included [65]. In this study, using the Coarse-grained MARTINI force field, we will use various sizes of gold nanocrystals as a probe to explore the transport of nanoparticles across DPPC bilayers and examine the structural and

mechanical properties of DPPC bilayers during the permeation. In our work, an external force was added as the driving force to aid the gold nanocrystals across the lipid bilayer, which mimics the common method used in experiments, using nanoparticle probe tips [7, 17, 105-107]. The minimum forces and pressures needed to penetrate the membrane are investigated in our simulations. We also study the mechanical and structural properties of lipid bilayers, including the local and bulk property changes during the permeation of the gold nanocrystals, which are also of considerable fundamental interest. There are experimental data available for comparison. Nanoparticles with no surface ligands have been used (nickel ferrite particles [108], silica particles [94]) as well as surface-modified nanoparticles (PEG-capped ZnO particles [109], oleic acid coated nickel ferrite [108], polymeric nanoparticles [7, 110], gold nanoparticles with cationic and anionic side chains [92], derivatized single walled carbon nanotubes [93, 111], PEG-coated Fe3O4 [112]), employing atomic force microscopy (AFM) imaging and force measurements, as well as fluorescence imaging and cell metabolic activity. Quantitative force measurements of nanoparticle cell membrane interactions have been reported [110] before too. We use gold nanocrystals (bare gold nanoparticles) in this chapter. In the next chapter, we will use surface-functionalized gold nanoparticles and examine how the nature of lipid-ligand interactions modifies the detailed mechanism of translocation. The findings described in this chapter may lead to better understanding of permeation of lipid membranes by bare nanoparticles, as well as taking a first step towards understanding and predicting cycotoxity of nanoparticles.

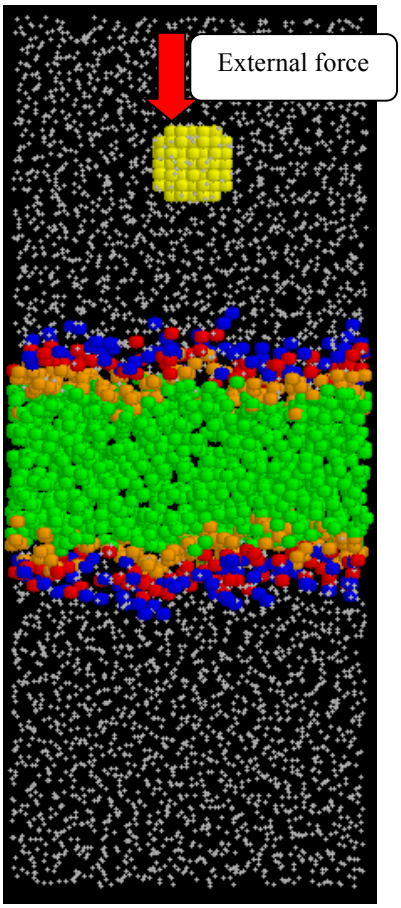

Figure 19. Side view of the simulation system for investigating the transport of a gold nanocrystal across the DPPC lipid membrane. (Yellow dots represent the gold nanocrystal, blue the choline group, red the phosphate group, orange the glycerol group, green the acyl chain tail group, white dots are water molecules). Gold nanocrystals, of sizes from 0.8 nm to 2.0 nm, are introduced into the water phase. A range of external forces is applied as described in the text.

4.2 Simulation of Lipid Bilayer with Gold Nanocrystals

After allowing for the equilibration of the lipid/water system (40 ns), we introduced one nanocrystal into our simulation system, as shown in Figure 19. We note that the results we have reported are for only one nanocrystal permeating the lipid membrane. The results observed would have significantly changed if several nanocrystals were permeating the membrane simultaneously. An external driving force was applied to aid the permeation of

nanocrystals across the lipid membrane. We then performed molecular dynamic simulations in the lipid bilayer system with various sizes of nanocrystals using a range of external forces. The simulation system in this chapter consists of 128 lipid molecules and approximately 3700 CG water molecules, with one rigid-body nanocrystal of the desired size. All the simulations were performed using the LAMMPS simulation package [113]. A Langevin thermostat [114] was applied in the NVT ensemble to maintain the desired temperature. To ensure stability, we used a time step of 10 fs. A typical simulation takes about 0.75 h per ns on Intel Core2Quad CPU system.

4.3 Characteristics and Mechanism of Nanocrystals Permeation

We first examine the minimum driving force needed for the nanocrystals to permeate through the lipid membrane. The minimum driving forces needed for crossing the first and second layers of the lipid are shown in Figure 20 (a). In our simulations we have defined the minimum force as that required to permeate the membrane in 100 ns or less. The minimum force for permeation across the first layer is in the range 55 - 425 pN, and for permeating both layers between 80 - 520 pN. The larger the nanocrystals, the larger the force needed. We also examined the minimum driving pressure (external force/cross sectional area of nanocrystals), which is shown in Figure 20 (b). We found that the pressure needed to permeate the first layer is almost independent of the size of the nanocrystals. For the permeation of both the first and second layers, the required pressure decreased with increase of nanocrystal size. A larger nanocrystal introduces more disruption in the bilayer as it permeates across the first layer. At the same time, the larger nanocrystal is closer to the second layer of the lipid membrane after it gets past the first layer, so it more easily

penetrates the second layer provided it can get across the first layer. This is consistent with the observed minimum pressure for larger nanocrystals being smaller than that for the smaller nanocrystals.

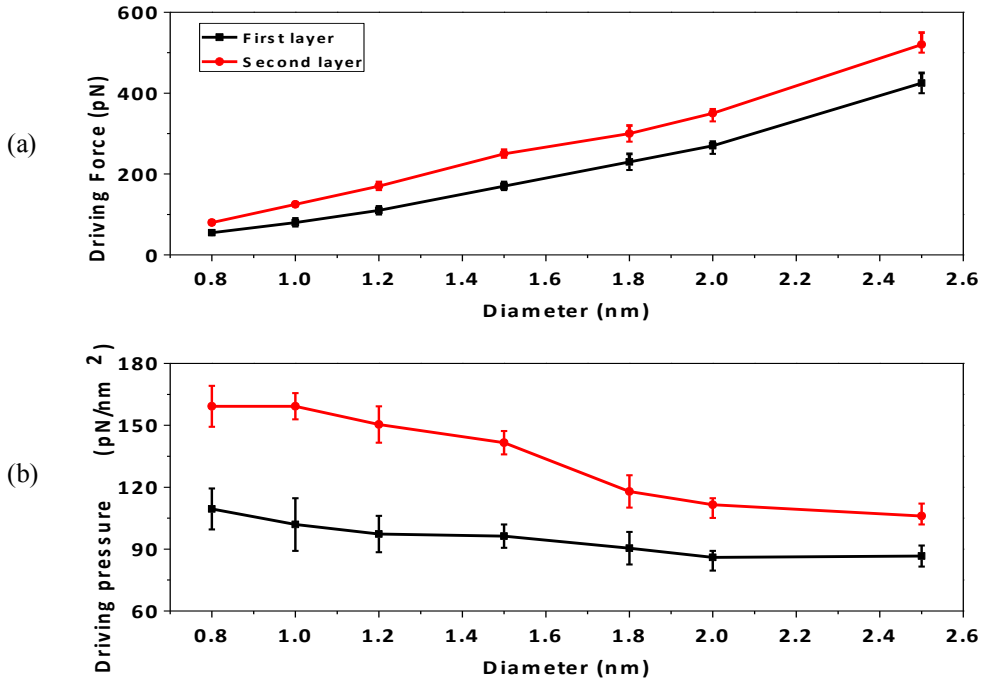

Figure 20. Minimum driving force (a) and pressure (b) needed for various sizes of nanocrystals to permeate the first and second layers of the lipid membrane.

To characterize the dynamics of nanocrystal penetration into the lipid bilayer, we calculate the velocity along the z direction of transport. We consider different sizes of nanocrystals permeating under the same driving pressure (160 ± 5 pN/nm^2) to study the particle size effect. The typical velocity profile for various sizes of nanocrystals under the same driving pressure is shown in Figure 21 (a). The velocity of the nanocrystal decreases when it approaches the lipid head group. The velocity drops by an order of magnitude in the

first head group region. In order to permeate the first layer of the lipid membrane, the nanocrystal has to compress the first layer and separate the head groups apart to make room for its cross sectional area. The resistance from the head group increases in this region, which we measured by letting the nanocrystals permeate at a constant velocity (1.55×10^{-6} nm /fs) through the lipid membrane to obtain the force profile (Figure 21 (b)). Vasir et al. [110] used AFM to measure the force between nanoparticles and cell membrane as the nanoparticle - decorated tip approached and retracted from the cell membrane. The early part of our force profile (Figure 21 (b)), which corresponds to the approach of the nanocrystal to the top layer, follows the same trend as the experimental force profile they generated as their tip with unmodified nanoparticles approached the live cell surface. They described this typical force-distance behavior as follows: As the AFM tip started to compress the cell surface, "a short-range repulsive force was observed due to steric repulsion presented by the viscoelastic surface of the cell." Unlike their experimental curve, our force profile for nanocrystal penetration does not exhibit any adhesion. Our force profile resembles that observed for an Au-coated nanotube tip penetrating the cell membrane in the experiments reported by Vakarelski et al. [107]. Following the initial force increase as the tip approaches the cell membrane, there is a sharp drop in the force exerted by the tip, after which the indentation into the cell continued with little resistance. This drop in force is indicative of the penetration of the nanotube through the cell membrane. Their force profile has a single peak. We have a more detailed force profile in Figure 21(b) because, unlike the experiments, we have better resolution, which allows us to show the variation in the force as the nanoparticle traverses each layer.

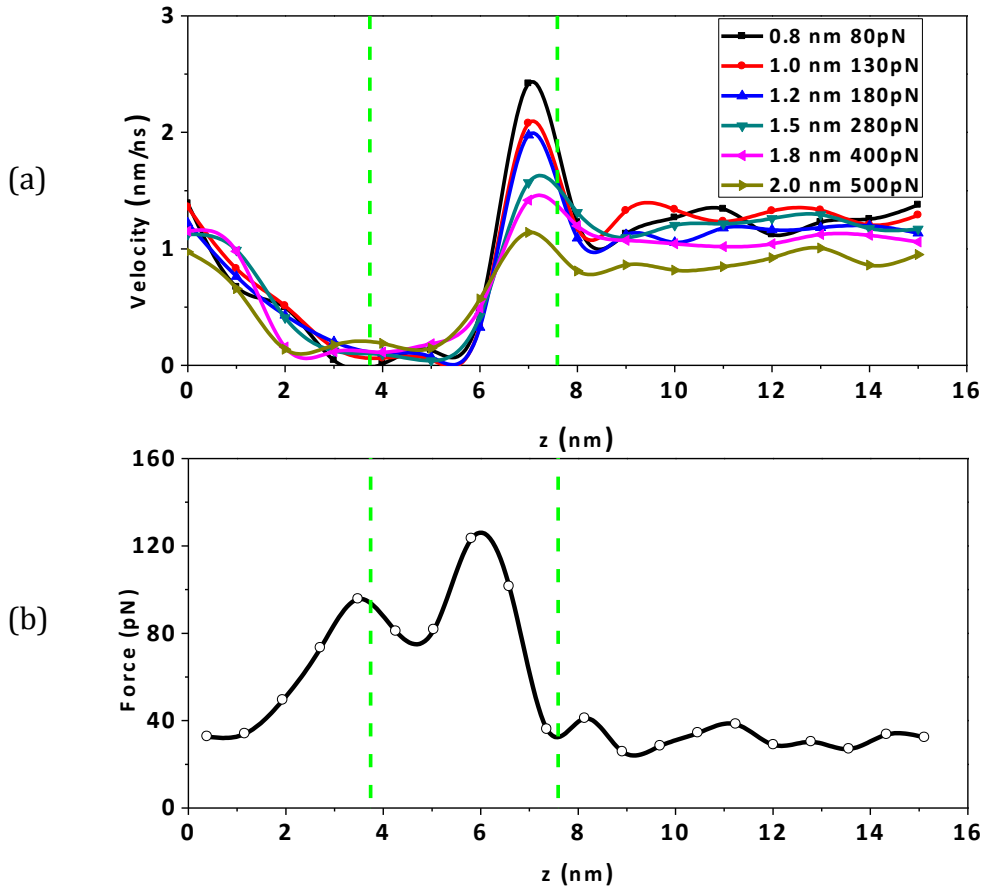

Figure 21. Nanocrystal velocity and force profile during the permeation. Using the same driving pressure, we obtain (a) velocity profiles of nanocrystals; using fixed velocity, we obtain (b) the force profile for the permeation of nanocrystals (1.0 nm). The red solid line indicates the equilibrium position of the phosphate groups.

We have also used the force profile to calculate the Potential of Mean Force (PMF) [115]. The results obtained are shown in Figure 22, where the results have also been compared with normalized experimental results [107]. The experimental results were also obtained by integrating the force profile reported in reference [107]. Since the probe used in the experiments was 25 nm, which is significantly larger than our system we normalized the system size to correspond to our size. In addition we used two energy normalization

methods. (a) In one case we normalized the experimental minimum energy in the PMF profile (not the position of the minimum nor the shape), and (b) in the second case the maximum energy (again not the position of the maximum nor the shape). These two normalizations method are shown to give almost identical results in Figure 22(a) and (b). Our results and those from experiments clearly show that an external force would be necessary to permeate the membrane initially, and once the nanocrystal has permeated the head group it would move rapidly to towards the tail region, as our results have also clearly shown.

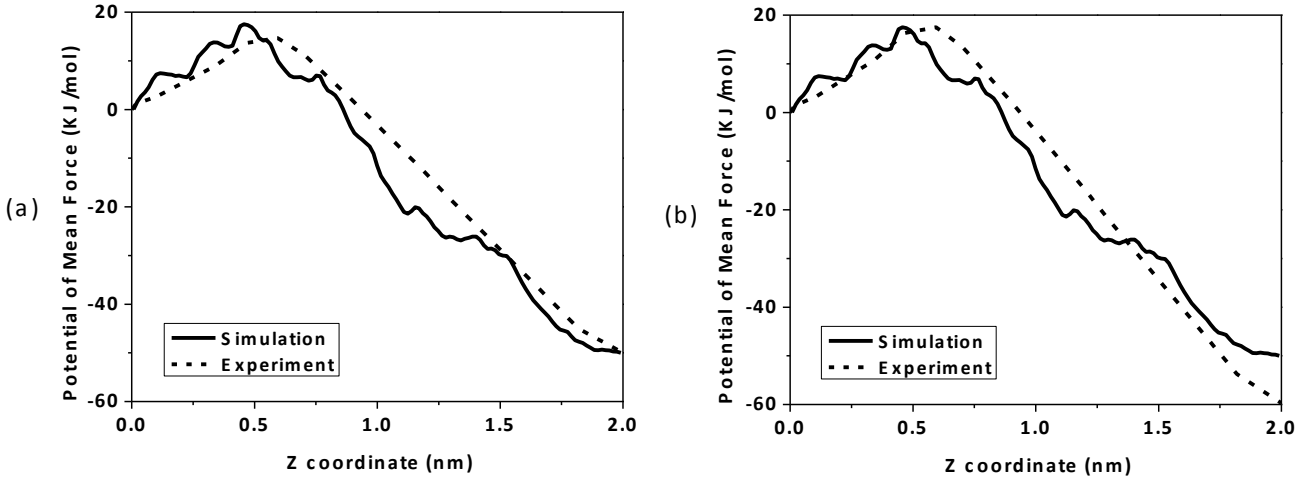

Figure 22: Potential of mean force profiles from simulation and experiment. Experiment value normalized using (a) Minimum value of PMF profile (b) maximum value of PMF profile.

The typical boundary lipid (lipid molecules in contact with the nanocrystals) density profile and the boundary water (water molecules in contact with the nanocrystals) density profile under the same external pressure are shown in Figure 23(a) and Figure 23(b). The boundary lipid density increases along with the nanocrystals permeating into the membrane since the lipid molecules are compressed by the nanocrystals. The boundary water density

shows a reverse trend. Some water molecules enter the lipid bilayer region during the permeation of nanocrystal, compared to the water density profile (purple line) in Figure 23(b) for the unperturbed membrane, which has a sharp drop in the lipid region. This occurs because the penetration of nanocrystal creates a pore in the lipid bilayer and allows some water molecules into the lipid region. The water density profile in Figure 12 is further evidence of the disruption of the lipid bilayer.

To further investigate the pressure effect on the nanocrystals, we specify one size of nanocrystal and carry out the simulations using different external pressures. The velocity profiles, force profiles and the boundary lipid and water density profiles showed the same trends reported in Figure 21 and Figure 23 and hence are not shown here.

We then examine the details of the deformation of the first and second layers of the lipid membrane as the nanocrystal approaches. In Figure 24 we show snapshots at various stages of the penetration process. Further, in order to see the local density changes compared to the rest of the bilayer, in Figure 25 we examine the xy plane density profile of the entire membrane at three stages of the penetration process: at the outset, before penetration of the first layer and before penetration of the second layer. As a complement to Figure 25, we examine in Figure 26 the curvature of the lipid layers at various stages of the penetration process.

The snapshots in Figure 24 (b) show the deformation of the first layer. The second layer of the lipid membrane does not show any significant change during the permeation of the first layer for this size of nanocrystal. The deformation of the first layer induces the deformation of the second layer gradually as the nanocrystals go deeper into the membrane center. Due to the attractive tail – tail interactions of the lipids in the second layer, the

deformation of the second layer is gradual. After the nanocrystal has crossed the first layer and starts to attach to the second layer, the first layer recovers and closes again, as can be seen in Figure 24 (d). At the same time, the second layer starts to be compressed and the alkyl tails start to separate from each other to make room for the nanocrystal, dragging their heads apart and thus the second layer starts to open up. In order to penetrate the second layer, the nanocrystal has to push the tail segments of the second layer away, which will drag the head group eventually. A pore is formed in the head groups of the second layer before the nanocrystal arrives there, which can be clearly seen in Figure 24(d).

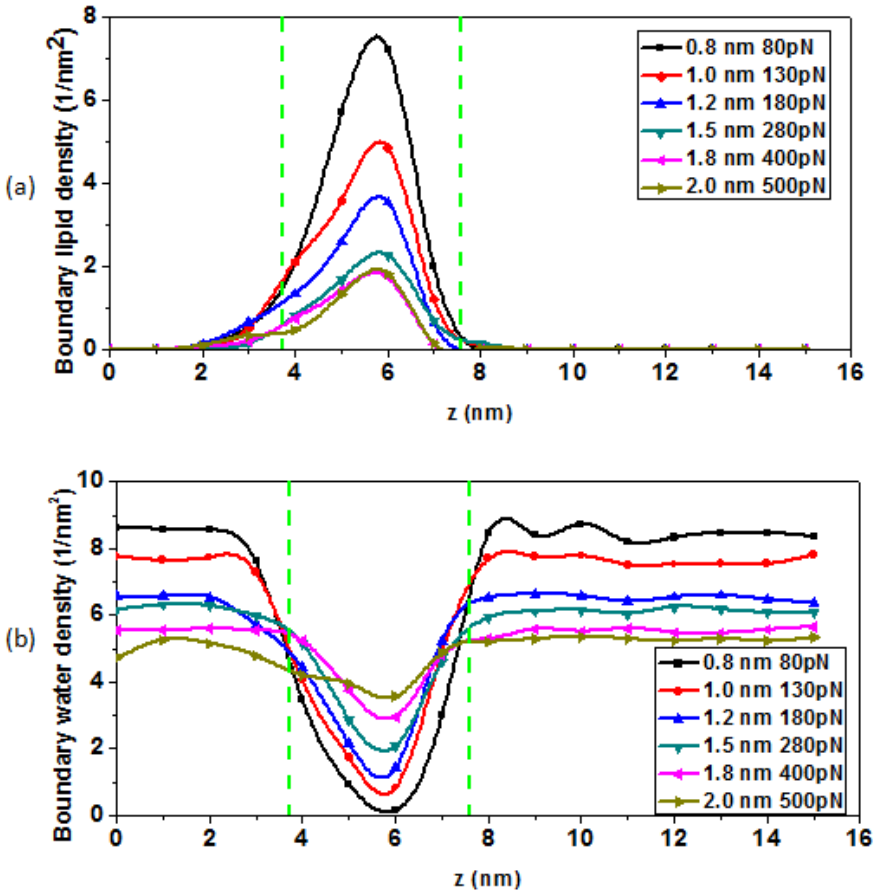

Figure 23. Boundary Lipid and water densities under the same driving pressure during the permeation of nanocrystals. (a) boundary lipid densities and (b) boundary water densities. The red solid line indicates the equilibrium position of the phosphate groups.

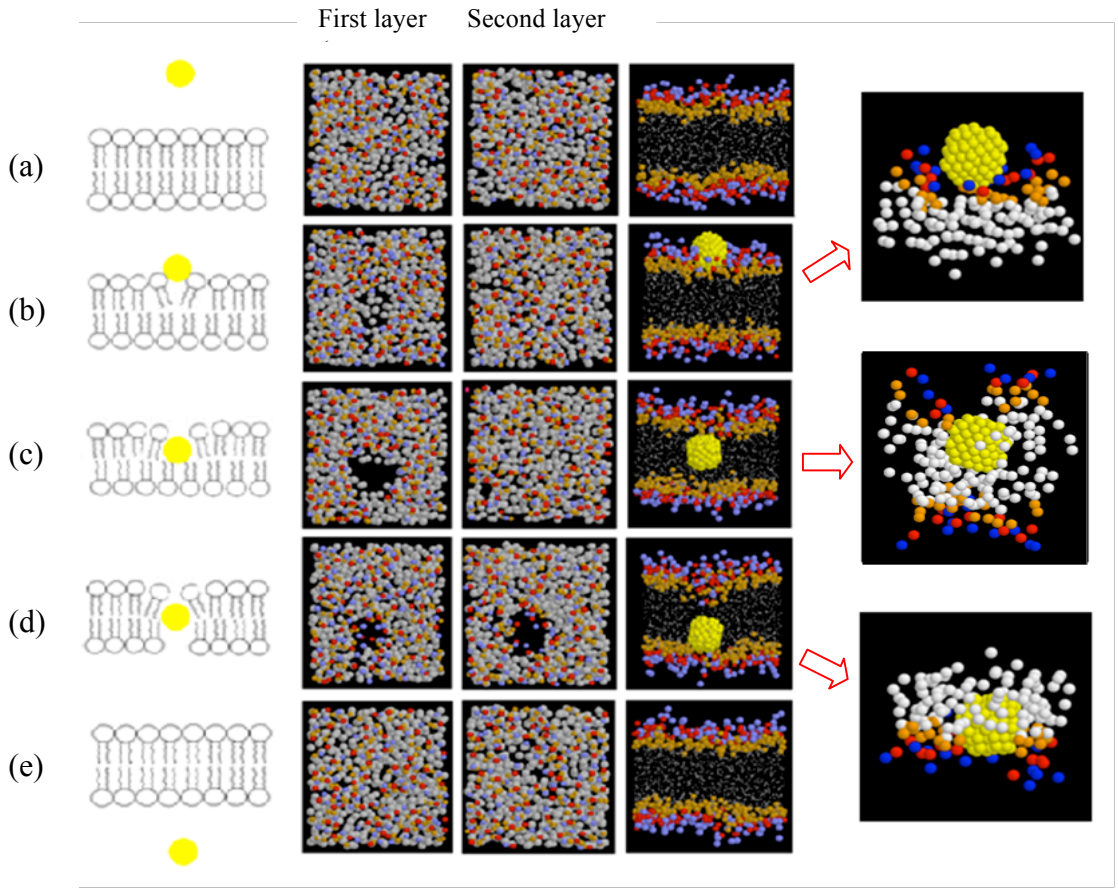

Figure 24. Snapshots in the permeation of the nanocrystal across the lipid membrane. The behaviors of the first and second layers of the lipid are shown. (a) the initial equilibrium configuration, (b) nanocrystal attaches to the first layer, (c) nanocrystal leaves the first layer, (d) nanocrystal attaches to the second layer, (e) nanocrystal leaves the second layer.

The xy-plane density profiles of DPPC lipid bilayer are shown in Figure 25, from which can be seen the local decrease in lipid density before permeating the second layer (blue line), in contrast to the permeation of the first layer (red line). Accordingly, as Figure 21(a), we observe a speed-up in the velocity profile and in Figure 21(b) a significant drop in the force profile as the nanocrystal passes through the second layer. The larger the size of the nanocrystal, the smoother the velocity profile. After a nanocrystal has permeated

through the second layer, both layers tend to recover their original status, as seen in Figure 24(e).

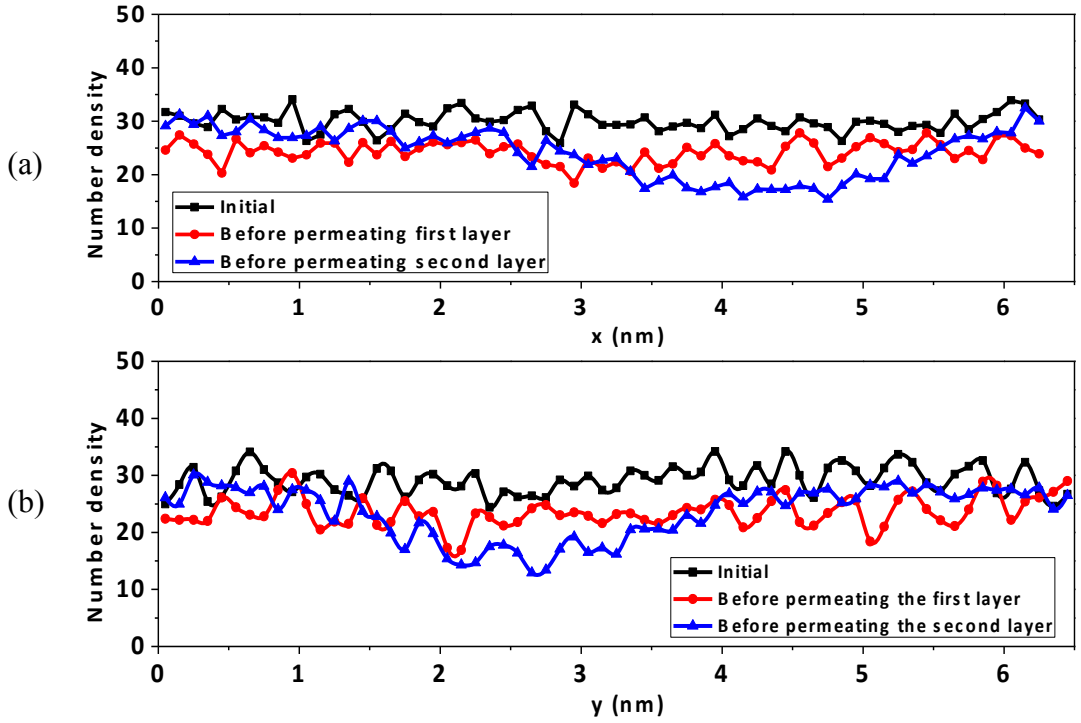

Figure 25. xy-plane density profiles of DPPC lipid membrane before 1.8nm nanocrystal permeates the first and second layers. The star indicates the x or y position of the nanocrystal for each stage. The local decrease in lipid density is seen in the density profile of the second and third stages.

Curvature of the lipid membrane occurs by elastic deformation of the membranes. In order to obtain the lipid membrane curvature profile, we define circular areas at different distances away from the surface of the nanocrystal and then average the z coordinates (normal to the surface of the membrane) of phosphate atoms included in each region. The membrane curvature for the permeation of a 1.8 nm nanocrystal is shown in Figure 26.

When the nanocrystal is attached to the first layer (and the second layer), we observe the obvious curvature. On the other hand, after the nanocrystal has totally penetrated the lipid membrane, the curvatures almost disappear, which shows the elastic property of the lipid membrane.

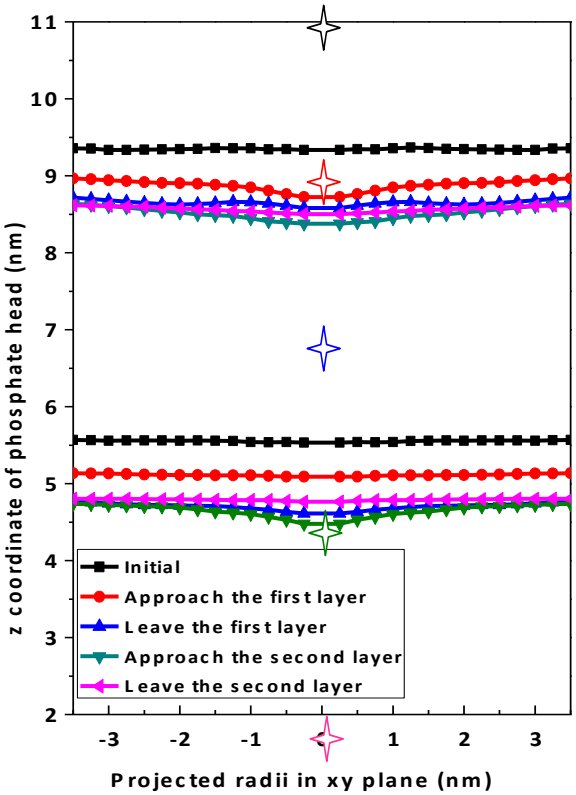

Figure 26. Curvature of first and second layers of the lipid membrane during the permeation of the 1.8 nm nanocrystal is depicted by the z coordinates of the phosphate group in circled shells in the xy-plane. The star indicates the z - coordinate of the nanocrystal for each stage.

Compared to atomistic MD simulations, a Coarse-Graining method represents a system by a reduced number of degrees of freedom. Due to the reduction in the degrees of freedom and elimination of fine interaction details, the dynamics of the coarse-grained

simulation are observed to be accelerated by a constant amount, called the speed up factor, compared to the same system in all-atom representation. Usually, the effective time sampled using CG is 3-6 times larger than the atomistic models [40]. When interpreting the simulation results with the MARTINI CG model, Marrink et al. find that a factor of 4 appears to describe the general dynamics present in many membrane systems quite well. Using this factor gives rates in good agreement with experiment and/or all-atom simulations for a variety of CG-simulated dynamic process (water permeation rates across the membrane [40], lipid lateral diffusion rates [40], aggregation of lipids into bilayers [40] or vesicles [116] and the sampling of the local configuration space of a lipid in a bilayer [117-118]), and they suggest using this factor to find effective times. The effective time for opening up the first layer shown in Table 7 is longer for the larger nanocrystals subjected to the same external forces, which is not surprising.

Table 7. Effective times for opening up the first layer

Diameter (nm)	Driving force (pN)	time (ns)
1.0	150	8
1.2	150	12.1
1.5	150	48.2
1.5	280	17.7
1.8	280	48.7

4.4 Internal Order and Structural Properties of The Lipid Membrane Under Nanocrystals Permeation

It is known that the penetration of nanocrystals can affect the stability and the mechanical strength of the lipid membrane. Microscopy experiments have examined the

formation of nanoscale holes caused by nanoparticles in model membranes [10, 119-120]. Chen et al. [96] observe data that are consistent with dendrimer nanoparticles making 3 nm holes in living cell membranes.

In our simulations, we observe the structural changes of the lipid bilayer at a more fundamental level, including the local and bulk tail segment order parameter, the local tail length of the lipid molecule. We also observe the elastic properties of the lipid bilayer by calculating the thickness change of the lipid membrane and observe whether the thickness of lipid membrane can recover or not after the nanocrystal permeation in our simulation period.

We extend our simulation time so as to observe the nanocrystal permeating the lipid membrane three times and observe the instantaneous thickness changes. The thickness (defined here as the head-to-head distance across the membrane) is shown for the unperturbed membrane (Figure 27(a)). The membrane thickness is shown with perturbation by small (1.0 nm, Figure 27(b)), medium (1.5 nm, Figure 27(c)), and large (2.0 nm, Figure 27(d)) nanocrystals. As seen in the Figure 27(a), the thickness of the lipid membrane oscillates around the equilibrium value stably in the absence of the perturbation of the nanocrystal. The permeation of the nanocrystal affects the thickness of the lipid membrane. As the nanocrystal begins to permeate the surface of the lipid membrane, the thickness starts to increase. After the nanocrystal has moved into the lipid membrane, the thickness of the lipid membrane increases significantly. The larger the nanocrystal, the greater the increase in the thickness of the lipid membrane. For the nanocrystal with diameter of 1.0 nm and 1.5 nm (Figure 27(b) and Figure 27(c)), the thickness of the membrane recovers after the permeation, which means the lipid membrane can heal itself quickly after the perturbation of small nanocrystals. For the 2.0 nm nanocrystal, the thickness of the lipid membrane does not

recover in our simulation period. This is due to the size of the simulation box. Under periodic boundary conditions, the membrane is approached again by the nanocrystal before it has had a chance to recover. We carried out two more simulations with the 2.0 nm nanocrystal to see if we can observe the recovery. After the nanocrystal has permeated through the lipid membrane and almost reached the far wall, we held the nanocrystal in place (this was accomplished by removing the external force on the nanocrystal and tethering it at this desired location) and continued the simulation for an additional 200 ns. We found that the membrane thickness remained elevated. We then carried out an additional simulation with a system size of (12.6 nm$\times$12.8 nm$\times$16.4 nm) and a 2 nm nanocrystal. In this larger simulation system, we did observe healing of the membrane. This result is expected since lipid membranes have been observed to self assemble from even an initial random configuration of DPPC bilayers [65].

The density profile of the DPPC lipid bilayer in the xy-plane shows the damage of the lipid membrane after the permeation of the 2.0 nm nanocrystal (Figure 28 blue line). We find that for the smaller nanocrystals, the xy-plane density profile of the lipid (not shown here) is able to recover its original status, which is almost a uniform distribution in the xy-plane just like the unperturbed lipid membrane. However, for the 2.0 nm nanocrystal, the local density in the region where the nanocrystal penetrates is lower than other regions, which means the local elastic property of the lipid membrane is disrupted by the permeation of the nanocrystal. This is consistent with the much longer recovery of the membrane thickness found in Figure 27(d) for this size nanocrystal.

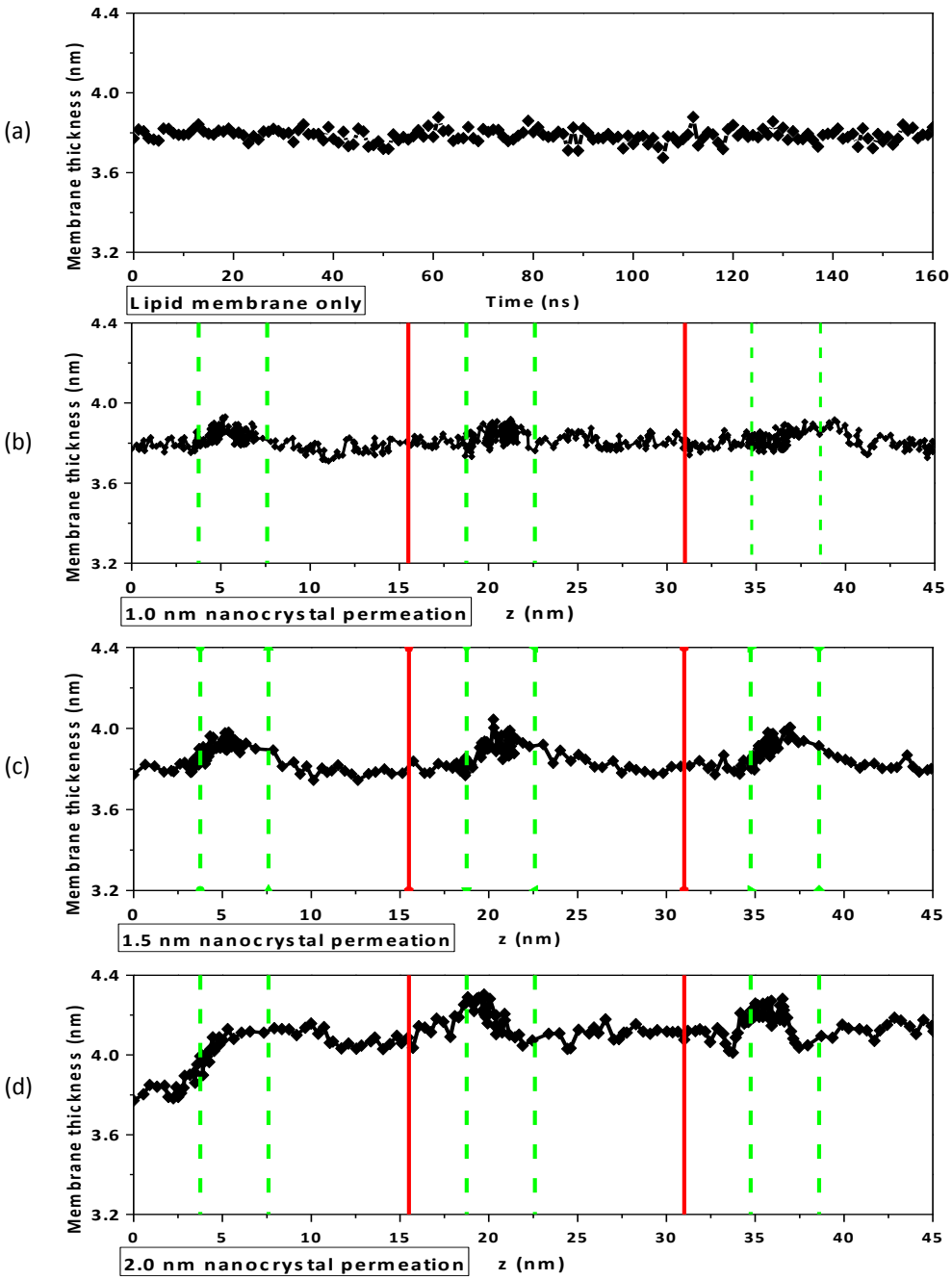

Figure 27. The changes in the lipid membrane thickness during the permeation of the nanocrystals. (a) the lipid-water system without the perturbation of nanocrystal. The extended simulation time permits the observation of the nanocrystal permeating three times through the membrane; instantaneous thickness of the lipid membrane is shown as an indication of the ability to recover. (b) the permeation of the 1.0 nm nanocrystal; (c) the permeation of the 1.5 nm nanocrystal; (d) the permeation of the 2.0 nm nanocrystal. The green dashed line indicates the equilibrium position of the phosphate group and the red solid line indicates the boundary of our simulation box.

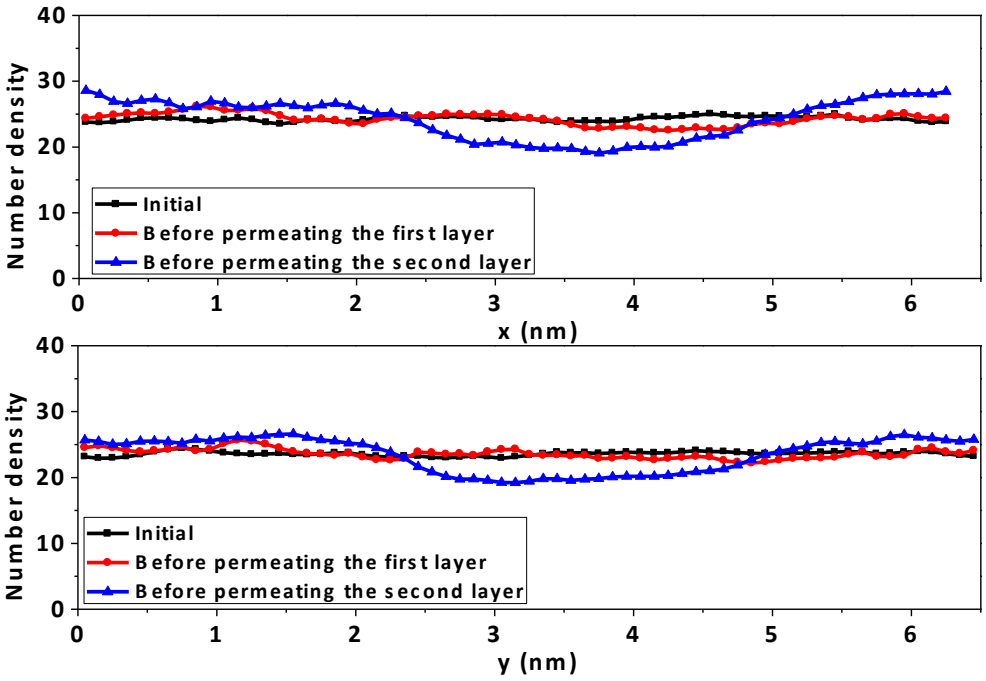

Figure 28. xy-plane density profiles (along x and y) of DPPC lipid membrane subsequent to permeation of both layers by the 2.0 nm nanocrystal. The lipid membrane suffers considerable damage after the perturbation of the 2.0 nm nanocrystal, as shown by the blue line. The star indicates the x or y position of the nanocrystal.

We calculated the effective permeation time for three successive permeations, which are listed in Table 8. The results shown are for three sizes with equal pressure (the force would vary as the square of the nanocrystal diameter). For the 1.0 nm and 1.5 nm nanocrystals, the effective times for the last two permeations are slightly different from the first permeation time. However, for the 2.0 nm nanocrystals, the permeation time for the last two permeations are obviously reduced, which is caused by the reduced local density and the disruption of the lipid membrane already mentioned above which has not had sufficient time to heal. We also notice that the permeation time for larger nanocrystals is shorter than those smaller ones in our cases. This has also been reported previously [34] and the most

likely explanation is that the larger particles can affect the internal structure more easily and create larger holes, which facilitate somewhat faster permeation. The permeation time for the second and subsequent permeations is usually shorter; between the first and second permeation enough time has not elapsed to allow the lipid to fully heal.

Table 8. Effective times (ns) for three permeations

Diameter (nm)	Particle volume (nm^3)	1^{st}	2^{nd}	3^{rd}
1.0	0.523	28.7	29.9	29.4
1.5	1.766	26.7	24.8	23.6
2.0	4.187	9.2	6.8	6.4

We also calculated the order parameter of the tail segment to characterize the internal order of the lipid membrane when the nanocrystals are in the lipid membrane region. The bulk order parameter is shown in Figure 29. We call it bulk order parameter because the value is averaged over all lipids, not only the lipids at the local site of the nanocrystal. Overall, the bulk order parameters change only slightly upon the insertion of the nanocrystals; minor structural changes are also observed from Wong-Ekkabut et al's work in the simulation of C_{60} insertion into a bilayer [98]. The bulk order parameter of the tail segment is a little bit larger compared to the unperturbed lipid membrane. The larger the inserted nanocrystal, the larger the bulk order parameter. We believe this phenomenon is due to the decrease of the dynamic space for the lipid membrane after the insertion of the nanocrystal, which induces lower mobility and lesser extent of isotropic averaging for lipid molecules of the entire lipid bilayer.

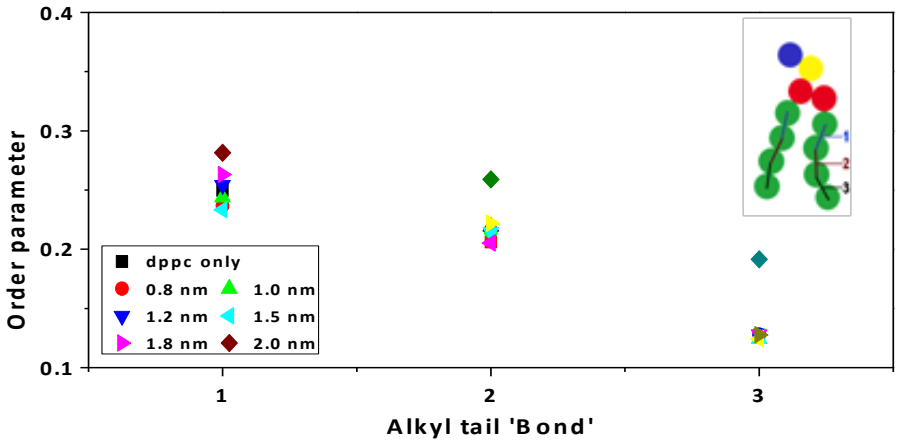

Figure 29. Bulk order parameter of the tail segments, (bond defined as in Section 2.3, with 'bond 3' corresponding to the end segment of the alkyl tail in the DPPC molecule) for the entire membrane during the permeation of various sizes of nanocrystals.

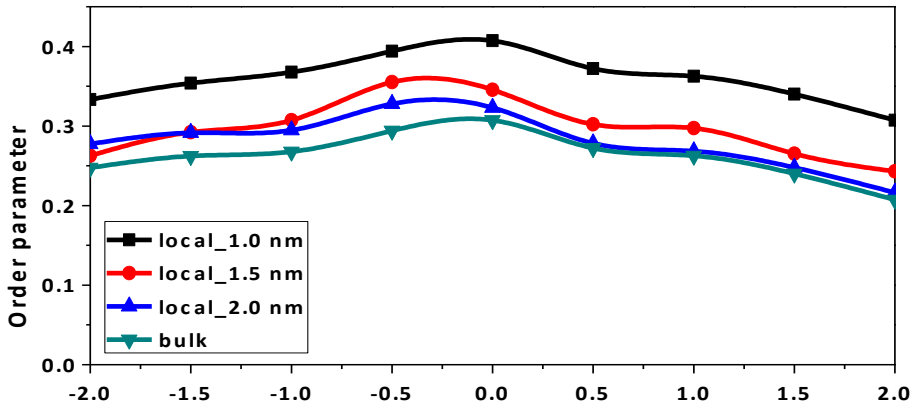

Figure 30. Typical local order parameter of 'bond 1' in the tail segments of lipids within 1.0, 1.5, 2.0 nm from the surface of the 1.8 nm nanocrystal. For 'bond 2' and 'bond 3', similar phenomena are observed (not shown).

We obtain further the local order parameter, which is an average over the lipids at the local site. We take the nanocrystal as the center and calculate the order parameter for those lipid molecules 1.0 nm, 1.5 nm and 2.0 nm away from the nanocrystal surface during the permeation. It can be observed in Figure 30 that the structural change for those lipid

molecules closer to the nanocrystal is more obvious than for those farther away. The tails of the boundary lipids are more ordered than the remote lipids since the dynamic space for the local lipid molecules is compressed much more than for the remote lipid molecules.

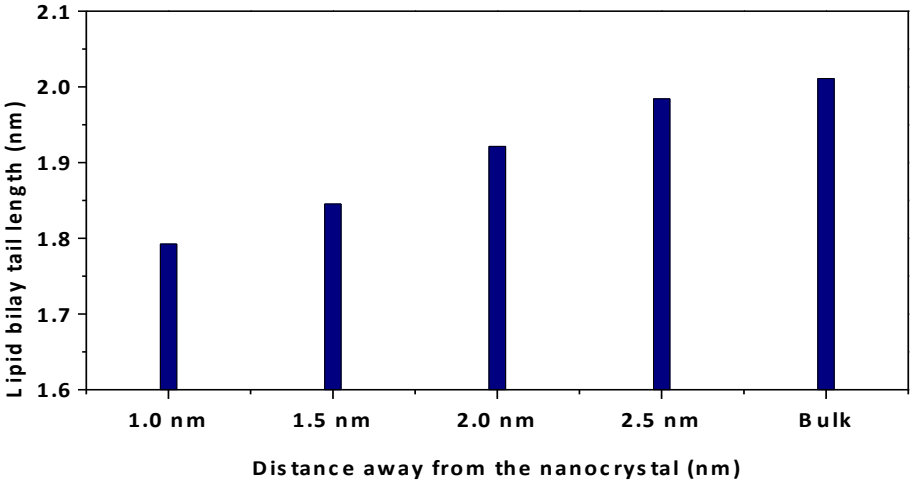

Figure 31: The average lengths of the tail segments of lipid within 1.0, 1.5, 2.0, 2.5 nm around the 1.8 nm nanocrystal during the permeation are compared with that for the unperturbed lipid.

Finally, we obtain the bulk and local average tail length of the lipid molecules (Figure 31) by calculating lipid tail end-to-end distances. From our simulations, the average tail length of the lipid bilayer without the perturbation of the nanocrystals is 1.944 nm. During the permeation, the average length of the tails is shorter for those lipids close to the nanocrystal. The closer the lipid, the shorter the tails, which is not surprising because compression by the nanocrystal results in bending of the lipid tails in the local region. Since the nanocrystals are moving under an external force and it is possible/likely that local equilibrium has not been achieved around the nanocrystals. We therefore also compared our

results for the bulk order parameter and local order parameter shown (Figure 29 and 30) with cases when the nanocrystals permeated the membrane at half the average velocity (where it can be assumed that the system would be closer to quasi-equilibrium). Within the accuracy of the simulations we detected no differences in our results.

In the next chapter we will discuss the permeation of ligand-coated nanoparticles through a lipid membrane.

5 PERMEATION OF LIGAND-COATED NANOPARTICLES THROUGH A LIPID MEMBRANE

Surface modification of the nanoparticle offers the possibility of creating site-specific carriers for both drug delivery and diagnostic purposes. In this chapter, we use CG-MD simulations to explore the permeation characteristics of ligand-coated nanoparticles through a model membrane. We compare permeation behaviors of ligand-coated nanoparticles with bare nanoparticles to provide insights into how the ligands affect the permeation process. As with gold nanocrystals, the minimum driving force for nanoparticles to penetrate the membrane and the permeation characteristics of nanoparticle are investigated. The structural properties of both nanoparticles and lipid membrane during the permeation are also examined in this chapter.

5.1 Introduction

Recently, experimental techniques have been reported [121-123] to synthesize nanoparticles with well-controlled size, geometry and surface coatings. Designing multifunctional nanoparticles for biomedical application requires fundamental understanding of the interactions between nanoparticles and biological membranes, which remains largely unknown. It has been shown that such interactions are often determined by general physicochemical factors of nanoparticles and the characteristics of the environment such as the type of membrane and the interaction with other biological entities present in the system [87, 112, 124]. It has also been demonstrated in many cases that the details of molecular structure of the ligands and their distribution on the surface can have a profound effect on the mechanism by which the nanoparticle is transported across the membrane or

incorporated into the cell [125-126]. At the same time, the ability of these engineered nanoparticles, which are expected to be used increasingly in industry, to enter and be transported within biological bodies in ways that larger particles cannot, may have concomitant adverse toxicity effects [91-93]. Investigation of nanoparticles biocompatibility and toxicity has been a growing interest in addressing the impact of nanotechnology on human health and the life environment [100-103].

In the last chapter, we used a coarse-grained model to simulate the permeation process of gold nanocrystals (gold nanoparticles without surface ligands) across a model lipid membrane and obtain the membrane response in terms of structural and mechanical properties of the lipid membrane under the perturbation of nanocrystals of various sizes. In this chapter, we extend our studies to functionalized nanoparticles with surface ligands and explore how those ligands affect the details of the permeation process. Uncharged hydrophobic ligands of different lengths were investigated here and an external force was added as the driving force to aid nanoparticles across the lipid bilayer. The external force is a mechanical force that is applied on the nanoparticle. It mimics the force a nanoparticle can experience during its transport inside body. In real systems it can be a result of collisions, external magnetic fields [127], or a random external force due to radiation [128]. In some experiments, penetration of nanoparticles across the bilayer has been aided by an external force, for example by using a nanoinjector [105]. The nanoparticle-lipid interaction was investigated in our simulations, in which the potential of mean force profile, the minimum forces needed to penetrate the model membrane were obtained and the permeation characteristics for nanoparticles with and without ligands were examined. We also studied

the structural properties of both the nanoparticles and lipid bilayers during the penetration, including local and bulk properties in this chapter.

5.2 Simulation of lipid membrane with nanoparticles

We perform molecular dynamics simulations for a lipid membrane system with one nanoparticle. The model membrane investigated here consists of DPPC (C_{16}) lipid bilayer. The lipid membrane/water system consists of 512 DPPC molecules and 11828 CG waters (4 water molecules in each CG water) in a $12.6 \times 12.8 \times 16.4$ nm^3 simulation box. We have previously shown in chapter 3 that this bilayer membrane self-assembles from the isotropic solution of lipids in CG simulations and that the properties of the self-assembled bilayers are in good agreement with experimental measurements, which validate the effectiveness of the coarse-grained model we are using for the lipid bilayers. We have also shown that the coarse-grained model can be used for the nanoparticle construction effectively in Chapter 3.

After allowing the equilibration of the lipid-water system (50 ns), we introduced one gold nanoparticle with flexible ligands into our simulation system, as shown in Figure 32. To make a room for the nanoparticle, roughly 800 CG water molecules were removed. All the simulations were performed using the LAMMPS simulation package [113]. A Langevin thermostat [114] was applied in the NVT ensemble to maintain the desired temperature at 323K.

An external driving force was applied to aid the permeation of the nanoparticle across the lipid membrane. We note that the results we report here are for a single nanoparticle permeating the lipid membrane. The results observed may significantly change if several nanoparticles were permeating the membrane simultaneously.

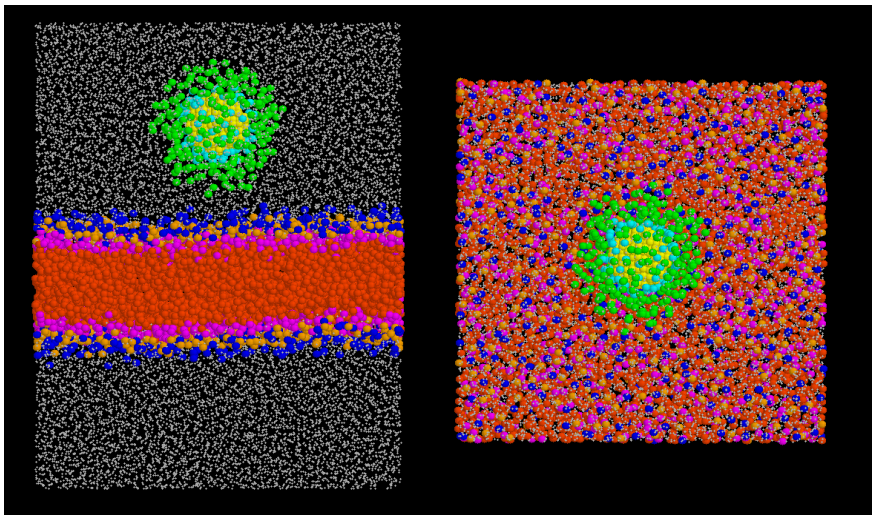

Figure 32. Side and top view of the simulation system for investigating the transport of a nanoparticle across the DPPC lipid membrane. (Yellow dots represents the gold core, cyan the surface sulfur atoms, green the hydrophobic chains, blue the choline group, orange the phosphate group, magenta the glycerol group, red orange the acyl chain tail group, white dots are water molecules).

5.3 Comparison of the Permeation Characteristics for Bare and Ligand-coated Nanoparticles

We first examine the minimum driving force needed for the nanoparticles to permeate through the lipid membrane. The minimum driving force for crossing the first and second layers of the lipid membrane are shown in Figure 33. In our simulations we have defined the minimum force as the smallest force required to permeate the membrane in 100 ns. Our minimum force for nanoparticles permeating across the first layer is in the range of 175 - 225 pN, and 350 pN – 550 pN for permeating both layers. The forces we have used are generally within the general range. The interaction forces applied to cell membranes, which are not large enough to cause cell rupture, using AFM probe tips coated with NPs is in the range (50pN and 1200pN) [110]. For example, in the Vakaresko experiments, AFM

20-25 nm tips applied loads of only 100-200 pN [110]. The external forces used in our simulations are of the same order of magnitude.

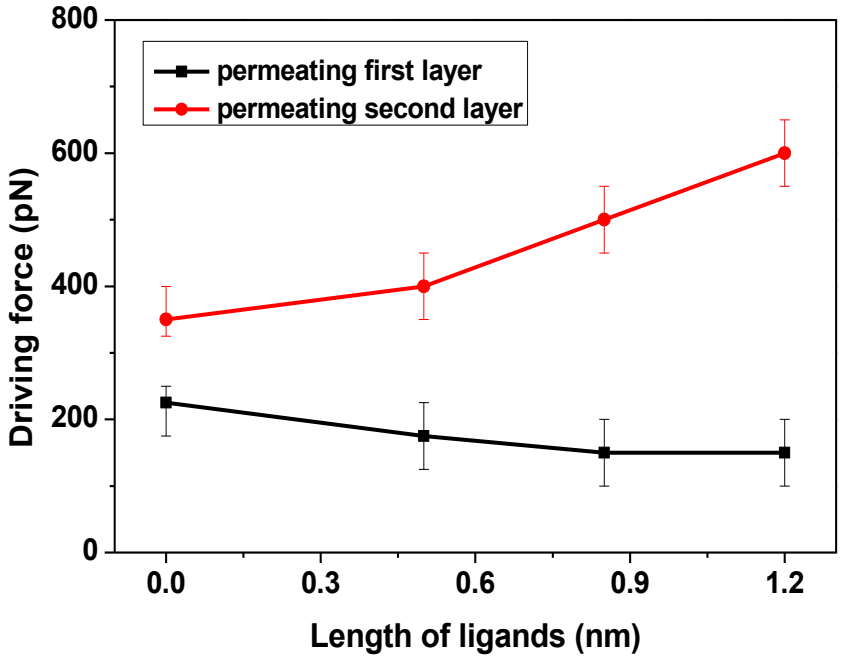

Figure 33. Minimum driving force for nanoparticles permeating the first and second layers of the lipid membrane.

To permeate the first layer, the force needed for a nanoparticle with ligands, small, medium and large (AuNP_SL, AuNP_ML and AuNP_LL) is smaller than for a nanoparticle without ligands (AuNP_bare). Compared to the bare nanoparticle, the ligands introduce more disruption in the first layer as the ligand-coated nanoparticles get close to the surface of the first layer under the same external forces, making it easier to open up the lipids to accept the nanoparticles into the bilayer. Figure 35 also illustrates these differences. For this type of nanoparticle in the range of ligand lengths studied, we also find the force needed for

ligand-coated nanoparticles decreases a little bit with the increase of ligand length on permeating the first layer. For the permeation of both first and second layers, the required force increases as the ligand length increases. Due to the interaction between hydrophobic ligands and hydrophobic lipid tails, a larger force is needed for ligand-coated nanoparticles to permeate the second layer, resulting in a larger force needed for the permeation. Therefore, the longer the length of the ligands, the larger the force needed for penetration. Since we are using the same gold core for all the simulations, the effective nanoparticle size is increasing with increasing ligand length. In the previous bare nanoparticle study, we had also found the larger the nanocrystal, the larger the force need for permeation.

We also obtain and compare the potential of mean force (PMF) profiles for bare and ligand-coated nanoparticles. We constrain the nanoparticles and move the nanoparticles at the constant velocity of 0.1025 m/s through the simulation box. This nanoparticle velocity used here is much larger than experimentally obtainable (which would require simulations almost 400 times longer [129]). However, we believe our simulations still represent the permeation process realistically. This is demonstrated by the recovery the lipid layer between two permeation cycles indicating no permanent damage to the membrane even at these higher velocities, and results obtained in other simulations using similar velocities. The force on the nanoparticles is measured and integrated over the positions to obtain the PMF profile. This standard integration method was also described in reference [115]. The PMF profile of nanoparticles is shown as a function of position along the z-direction (direction of nanoparticle motion), calculated from the water phase to the center of lipid phase, are shown in Figure 34.

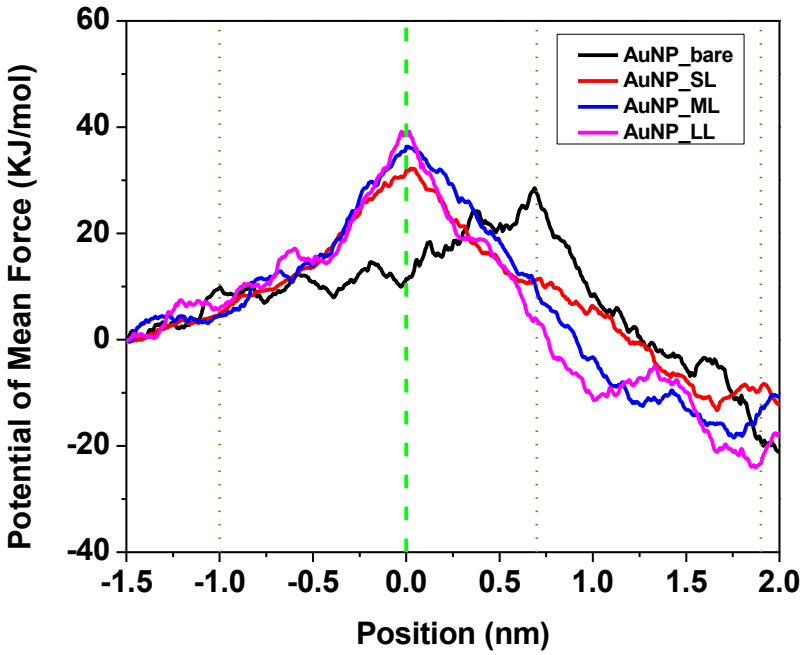

Figure 34. Potential of mean force profile for the permeation of nanoparticles through the first layer of the membrane bilayer. (The x-axis refers to the position of the center-of-mass of the nanoparticle, the green dashed line indicates the interface between water phase and lipid phase and the dotted lines indicate the positions corresponding to the snapshots shown in Figure 35.)

Our results show that the ligand-coated nanoparticles as well as the bare nanoparticle show a strong preference for the center of membrane, however there are energy barriers at the water-lipid interface as the nanoparticle is moving closer to the lipid membrane, preventing the nanoparticle from moving into the membrane spontaneously. Therefore, an external force is necessary for nanoparticles to penetrate into the membrane initially, and once the nanoparticles have permeated the head group they would move towards the center of the membrane. We do note that if several nanoparticles were to attempt this simultaneously, it is conceivable that one would have enough energy to overcome this barrier spontaneously without the need for an artificial external force. The PMF profiles of

our hydrophobic nanoparticles show agreement with those of fullerenes [25-27, 98] and nanoparticles [33] having hydrophobic nature in previous studies. The longer the ligand length, the larger the energy barrier encountered at the interface and the lower PMF is found in the interior of the lipid membrane. If Figure 33 is compared with Figure 34, there appears to be an apparent inconsistency. While the minimum force decreases with the length of the ligand ($F_{LL}^{min} < F_{ML}^{min} < F_{SL}^{min}$), the energy barrier at the interface shows an opposite trend. The minimum force is a point property, while the PMF is an integral property. When the ligands are longer, the region of interaction between the nanoparticle and interface increases, which leads to a larger energy barrier, even though the minimum force needed was lower for the longer ligands.

Another interesting observation relates to the position of the peak of the energy barriers. For a bare nanoparticle the barrier is at about 0.7 nm inside the interface. The bare nanoparticle touches the interfaces at a center-of-mass distance about 1.0 nm away from the surface. At that point the nanoparticle faces resistance from the lipid bilayer until it is about 0.7 nm into the interface. At this point the nanoparticle is essentially sucked into the center of the bilayer as the head groups begin to realign and the tails push the nanoparticle into the bilayer center. The snapshots for the permeation of bare nanoparticle through the first layer of lipid membrane are shown in Figure 35. For nanoparticle with ligands, the ligands play a crucial role in opening up the lipid bilayer interface, so the energy barrier peak roughly corresponds to the nanoparticle center-of-mass being at the interface. The position of the peak is slightly inside the interface for the shortest ligands, since they cause the least disruption inside the lipid interface. Once the ligands are inside the bilayer they can easily

open the lipid tails and move to the center of the bilayer. Figure 35 also shows nanoparticle with ligands as it moves in the bilayer.

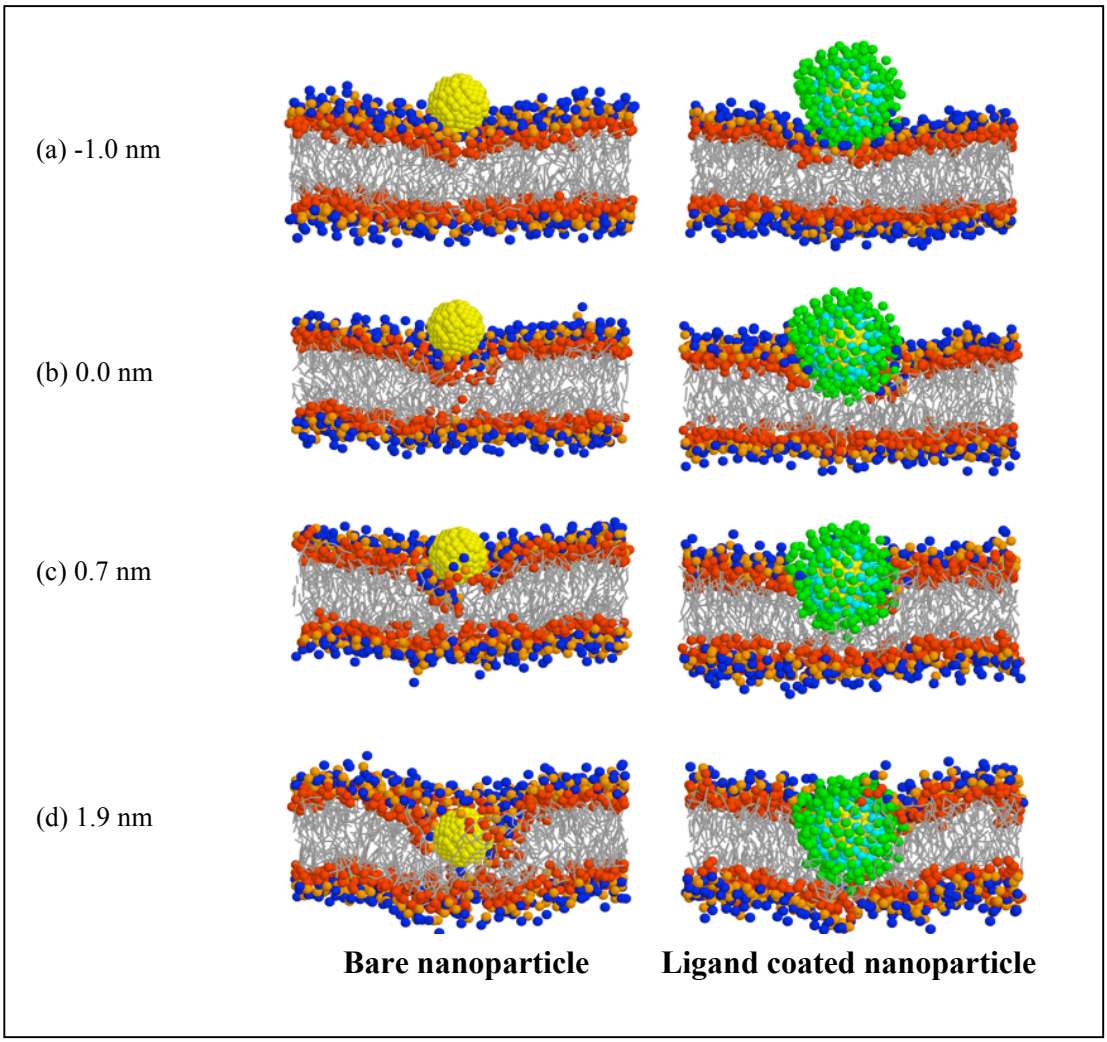

Figure 35. Snapshots for the permeation of bare and ligand-coated nanoparticles (AuNP_ML) through the first layer of lipid membrane.

To compare the dynamic characteristics of nanoparticles with and without ligands during the permeation process, we plot the velocity and force profile along the direction of motion of nanoparticles (z direction). We consider AuNP_bare, AuNP_SL, AuNP_ML and

AuNP_LL nanoparticles permeating under the same driving force (600 pN) to study how the ligands change the permeation dynamics. We obtain the force profile by letting the nanoparticles permeate at a constant velocity (0.41 m/s) through the lipid membrane. Typical velocity profiles and force profiles for the permeation are shown in Figure 36 and 37. As we trace out the changes on the velocity and force profiles during the permeation process, our understanding of the molecular events is aided by examining the changes in the distribution of the lipid molecules in front of the nanoparticle (in the direction of its motion) at the same time. For this purpose, we obtained the lipid membrane xy-plane density profiles and the radial density profiles. These were obtained by calculating the number density of lipid molecules in front of the nanoparticles (in the direction of motion) and are shown in Figure 38 (a) and (b) respectively. We discuss the profiles in Figure 36 and 37 enlightened by lipid molecule distributions in Figure 38.

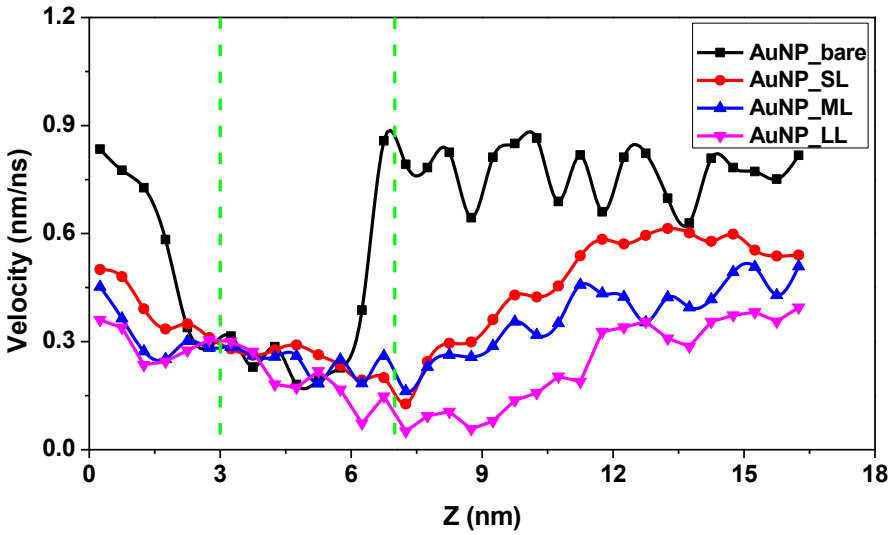

Figure 36. Velocity profile of gold nanoparticles (z component) for nanoparticle permeation under the same driving force (600 pN). The green dashed line indicates the equilibrium position of the phosphate head groups.

For all nanoparticles, the velocity decreases when nanoparticles approach the head groups of the lipid membrane and the resistance increases gradually in this region. Therefore, an external force would be necessary to permeate the membrane initially. In the entry region (2.5 – 4 nm in the z-axis in Figure 36 and 37), in order to permeate the first layer of the lipid membrane, the nanoparticle has to compress the first layer and push the head groups apart in order to make room for its cross-sectional area. Therefore, the velocity of the nanoparticle decreases in this region and the resistance from the head group increases continuously in this region accordingly.

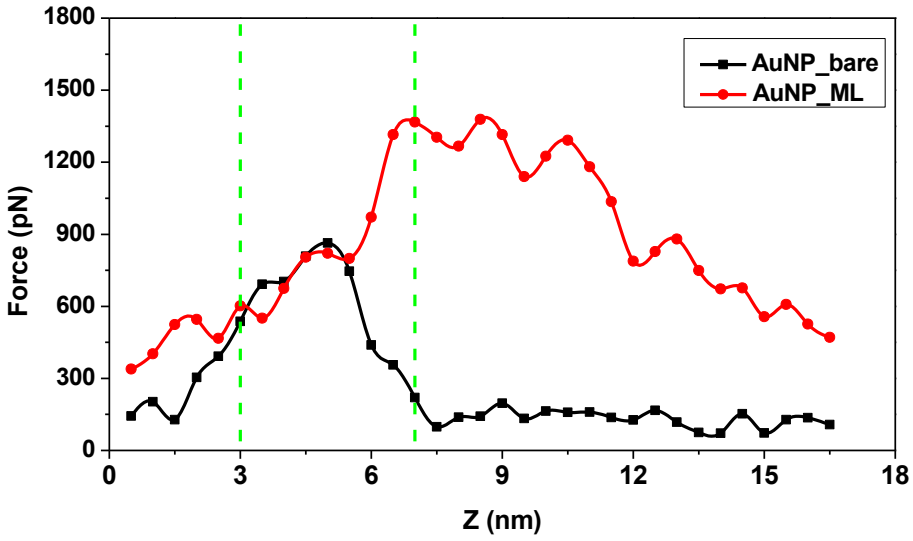

Figure 37. Force profiles of gold nanoparticle (AuNP_ML nanoparticle) under a fixed velocity (0.41 m/s). The green dashed line indicates the equilibrium position of the phosphate head groups.

As the nanoparticles move deeper into the membrane center (4 – 5.5 nm in the z-axis in Figure 36), the velocity of nanoparticles slows down further. The deformation of the first layer induces the deformation of the second layer gradually, maintaining a pore in the

direction of motion of the nanoparticle. The xy-plane density profile and the radial density profiles, shown in Figure (38(d) and (e)), are the same for all the nanoparticles we investigated in this region. Therefore, the size of the effective pore created in the membrane remains the same as the entry region (Figure 38(f)). Thus, similar velocity and force curves for AuNP_bare, AuNP_SL, AuNP_ML and AuNP_LL nanoparticles are obtained in this region.

After the bare and ligand-coated nanoparticles attach to the second layer and move through the exit region (5.5 – 7.5 nm in the z-axis in Figure 36), the xy-plane density profiles and the radial density profiles begin to show different delineations, resulting in differences in permeation behavior in this region. As seen in our previous report, when the bare nanoparticle has totally crossed the first layer, the first layer starts to recover, the second layer is to be compressed and the tails of second layer separate from each other, dragging the head group apart to form a pore in the second layer even before the nanoparticle arrives there. Accordingly, a speed-up in the velocity profile (Figure 36) and a significant drop in the force profile (Figure 37) are observed as the AuNP_bare nanoparticle passes through the second layer. The xy-plane lipid density profile (Figure 38 (g)) shows the recovery of lipid membrane as the bare gold nanoparticle moves through the exit region. The peak at 1.7 nm in the radial lipid density profile (Figure 38(h)) drops significantly because the bare gold nanoparticle pushes the lipid molecules away and the number of lipid molecules in front of the nanoparticle decreases, resulting in the reduction of the effective pore size created in the lipid membrane in this region (Figure 38(i)).

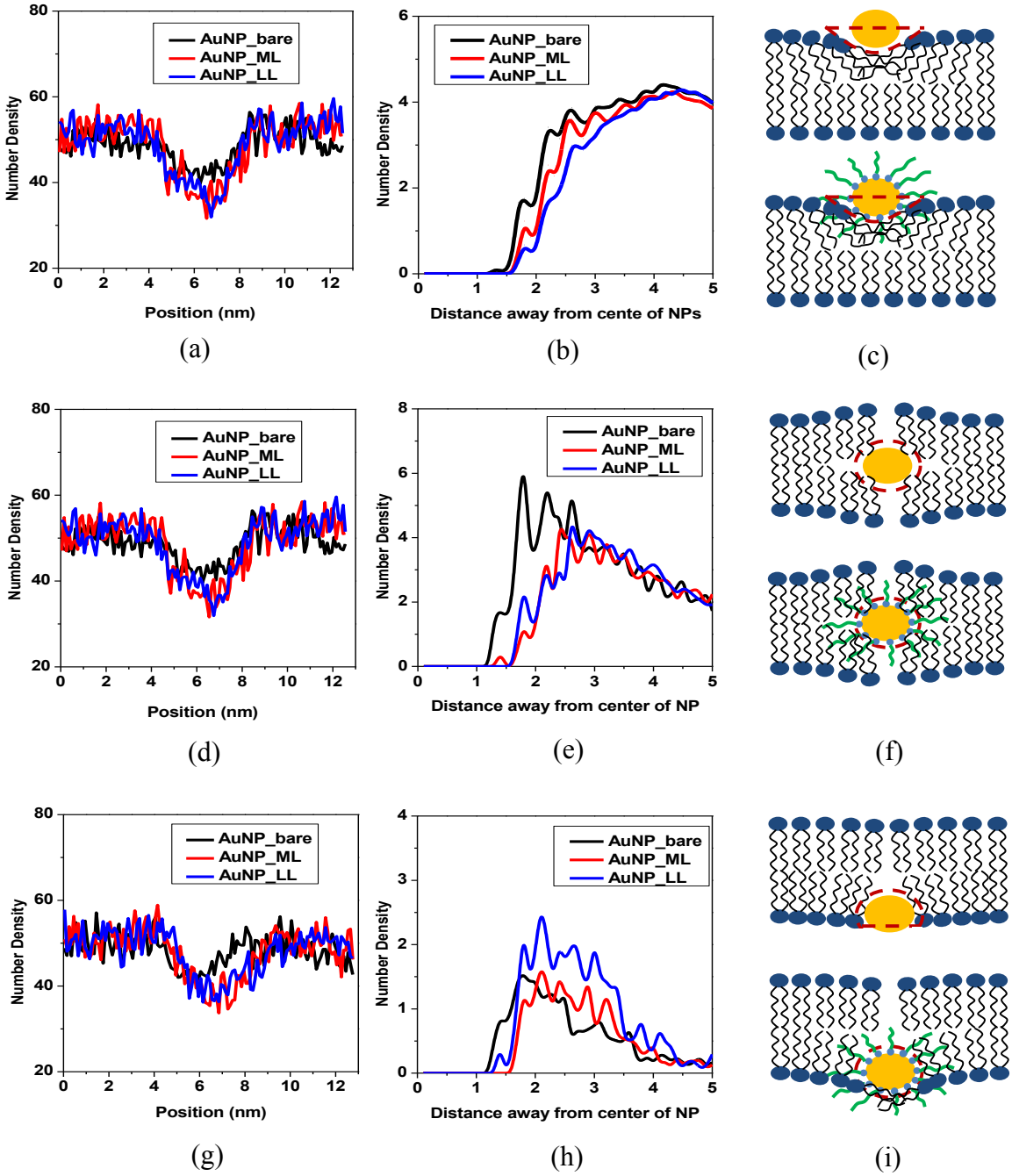

Figure 38. Illustrations and x-plane lipid membrane density profile and radial density profiles for those lipid molecules in front of the nanoparticles (AuNP_bare, AuNP_ML and AuNP_LL nanoparticles are shown here). (a-c) Nanoparticles in the entry region; (d-f) Nanoparticles inside the membrane; (g-i) Nanoparticles in the exit region. Y-plane lipid membrane density profiles show the same trend as x-plane's, which is not shown here. The dashed red line in (c), (f) and (i) shows the effective size of pore created in the lipid membrane.

In contrast, the ligand-coated gold nanoparticles (AuNP_SL, AuNP_ML and AuNP_LL) move more slowly in the exit region and exhibit a minimum in the velocity profile (Figure 36) after these particles have crossed the second layer. Due to the attractive interactions between lipid tails and ligands, the resistance continues to rise for these nanoparticles and achieve a maximum after they cross the second layer (Figure 37). As shown in xy-plane lipid density profile (Figure 38 (g)), compared to bare nanoparticle, the local decrease in the lipid density profile does not obviously recover, which means that the recovery of the lipid membrane is slower after permeation for ligand-coated gold nanoparticle in comparison to that for bare gold particles. In the radial density profile (Figure 38 (h)), we find the peak at a distance 1.7 nm from the center of the gold core and the magnitudes of the peaks remain the same, so the effective pore still exists in the exit region for ligand-coated nanoparticles (Figure 38 (i)). The entanglement of ligands and lipid molecules causes the gold nanoparticles with ligands to move more slowly in this region, in comparison to the bare gold particles. Thus once the nanoparticles enter the exit region of the bilayer, the ligand-coated nanoparticles exhibit behaviors different from the bare nanoparticle.

We now examine more clearly the effective pore created by the passage of the nanoparticle. We see the density profiles in the xy-plane show similar behavior for all nanoparticles. The peak in the radial density profile is located at about 1.7 nm away from the center of the gold core for all three nanoparticles, which means similar effective pores in the lipid membrane are created by bare and ligand-coated nanoparticles (Figure 38(c)) in this region. We also observed that some water molecules entered the lipid bilayer region during the permeation of nanoparticles, in contrast to the water density profile for the

unperturbed membrane. This occurs because the penetration of nanoparticles creates a pore in the lipid bilayer and allows some water molecules into the lipid region. This is further evidence of the disruption of the integrity of the lipid bilayer by the perturbation of a nanoparticle.

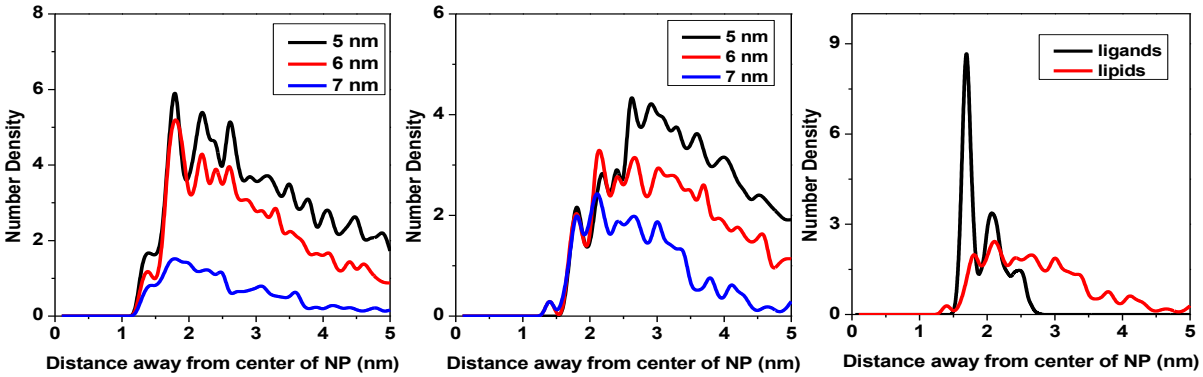

Figure 39. Distribution of ligands and lipids from the center of the gold core during the permeation of nanoparticles from the center of the bilayer to the exit region of the lipid membrane (AuNP_bare and AuNP_LL nanoparticles are shown here). (a) radial density profiles for AuNP_bare nanoparticle; (b) Radial lipid membrane density profiles for AuNP_LL nanoparticle; (c) Radial lipid membrane and ligands density profiles for AuNP_LL nanoparticle (7 nm in Figure 35).

In figure 39 we show the change of effective pore size in the lipid membrane by obtaining the radial lipid density profile along the direction of motion of a nanoparticle permeating the second layer, in the region starting from the center of lipid membrane (at 5.0 nm in Figure 36) to the head group of the second layer (at 7.0 nm in Figure 36). The density of lipid molecules around the bare nanoparticles (Figure 39(a)) drops significantly during its penetration of the second layer, indicating that the effective pore size reduces in this region. On the other hand, for nanoparticles with ligands (Figure 39(b)), no significant differences

are found for the density of lipid molecules around the nanoparticles, indicating the effective size of the pore is maintained in this region. The radial density profile for ligands and lipids are together shown in Figure 39(c), illustrating that some lipid molecules move inside the nanoparticle ligand region, resulting in the entanglement of lipid molecules with ligands. Because this occurs for ligand-coated nanoparticles, the effective size of the pore resulting from the boundary lipid molecules does not change significantly in the exit region during the permeation. The velocity remains slow and the force is higher, as seen in Figure 36.

Furthermore, we studied the orientation of boundary lipid molecules during the nanoparticle permeation process. We define a vector pointing from the lipid head group to the bead at the end of the lipid tail and calculate the tilt angle between this vector and the z-axis (normal to the surface of the lipid membrane). The lipid molecular orientation profiles for the permeation of the nanoparticles are shown in Figure 40 (a) and (b), for the entry region and the exit region, respectively. In the entry region, boundary lipid molecules have similar tilt angles when accepting both bare and ligand-coated nanoparticles. The angle for the majority of lipid molecules is in the range of 20 to 60 degrees, while around 20 percent of the lipid molecules have smaller or larger angles. On the other hand, in the exit region, the lipid molecule orientations for AuNP_bare and AuNP_LL nanoparticles show different trends. For the AuNP_bare nanoparticle, most lipid molecules are observed to tilt in the range of 0 to 40 degrees. Smaller numbers of lipid molecules are tilted by larger angles. For the bare gold nanoparticle, the lipid molecules in the exit region tilt less than in the entry region. This occurs because of the decreased dynamic space for lipid molecules in this region, resulting from the push back by the bare nanoparticle.

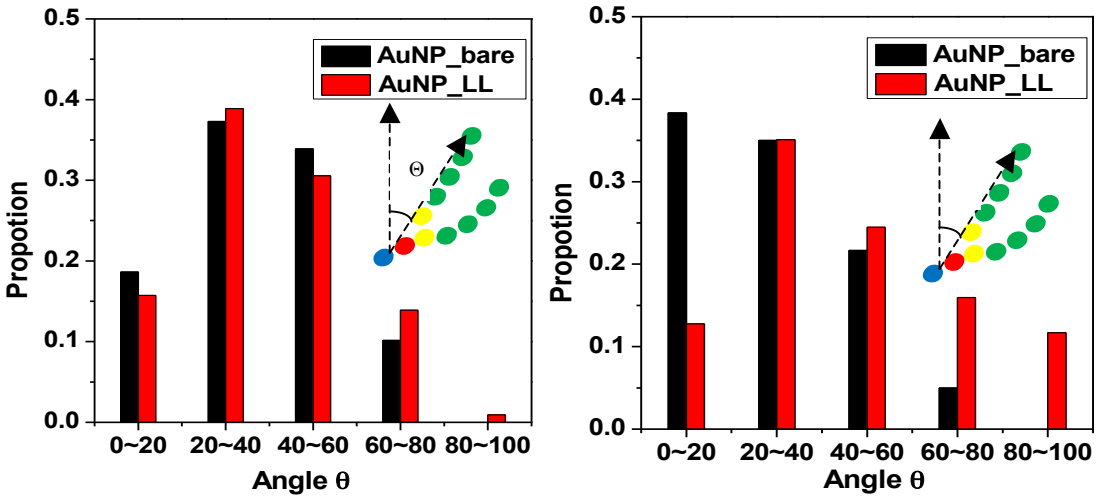

Figure 40. Orientation of lipid molecules close to the nanoparticle during permeation while nanoparticles (a) in the entry region and (b) in the exit region.

In contrast, for the ligand-coated nanoparticle, the distribution of tilt angles is wider and more uniform, compared to the bare gold nanoparticle. Around 10 percent of lipid molecules have large tilt angles (that is above 90 degrees), showing the tilt towards the membrane surface in this region. The tilting of lipid molecules maintains the effective size of the pore during nanoparticle permeation of the second layer. The interpretation in Figure 40(b) can also be seen in the snapshots in Figure 41(a) and (b). We see from Figure 41(a) that the bare gold nanoparticle creates a hole before the nanoparticle reaches the head groups of the lipid membrane and Figure 41(b) shows that the tails of lipid molecules move towards the ligand region and becomes entangled with the ligands, which results in the large tilt angle seen in Figure 40(b).

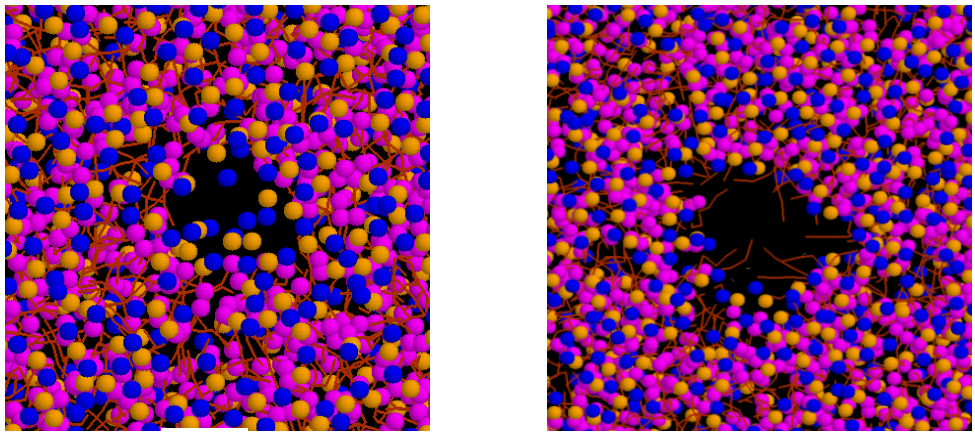

(a) (b)

Figure 41. Top view of the second layer of the bilayer when the bare nanoparticle (a) and AuNP_LL nanoparticle (b) is in the exit region. (Blue dots represent the choline group, orange the phosphate group, magenta the glycerol group, red orange the acyl chain tail group, gold nanoparticle and water molecules are hidden here).

5.4 Internal Order and Structural Properties of the Lipid membrane and Nanoparticles Under the Permeation

We obtain the bulk and local structural properties, including the thickness of lipid membrane, tail length of lipid molecule and tail segment order parameter when bare and ligand-coated nanoparticles are in the lipid membrane region. Figure 42-44 illustrates that the lipid membrane exhibits similar bulk properties during the permeation of bare or ligand-coated nanoparticles. The membrane thickness is shown for the pure membrane and under the perturbation of a nanoparticle bare or ligand-coated in Figure 42. The thickness of the lipid membrane starts to increase once the nanoparticles permeate the surface of the lipid membrane, compared to its equilibrium undisturbed condition. After the nanoparticles move into the membrane, the thickness of the membrane elevates significantly from its equilibrium value. Longer ligands induce more perturbation in the lipid membrane, resulting in a greater increase in the thickness. We observe that the thickness of the lipid membrane

recovers after perturbation by all three nanoparticles. This is expected since lipid membranes have been observed to self-assemble even from an initial random configuration of lipids in solution.

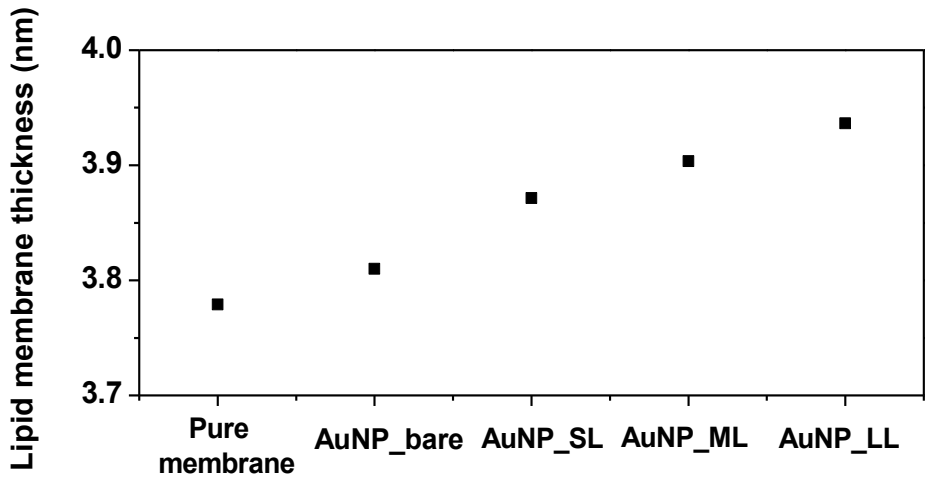

Figure 42. Average length of lipid tail segments during the permeation of AuNP_bare, AuNP_SL, AuNP_ML and AuNP_LL nanoparticles.

Furthermore, we obtain the bulk and local average tail length of the lipid molecules by calculating lipid tail end-to-end distances. Accompanying the increase in the thickness of the lipid membrane, the tail length of the lipid in the bulk also increases during the permeation of nanoparticles, which is shown in Figure 43. We observe that the longer the ligands, the greater the increase of membrane thickness and tail length it will induce. Moreover, the average length of the tails is shorter for those lipids closer to the nanoparticles because of compression by the nanoparticle during passage. Similar behavior is observed for both the bare nanoparticle and the ligand-coated nanoparticle.

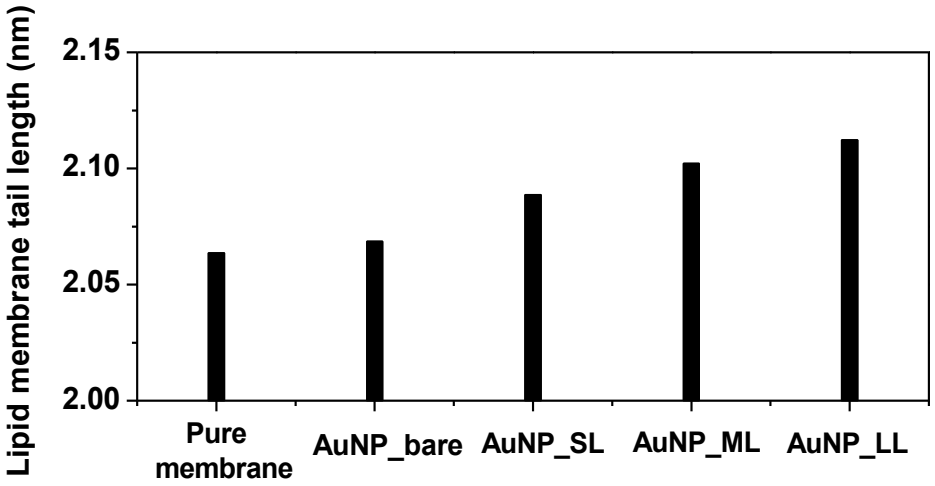

Figure 43. Order parameters of tail segment of lipid molecules during the permeation of AuNP_bare, AuNP_SL, AuNP_ML and AuNP_LL nanoparticles.

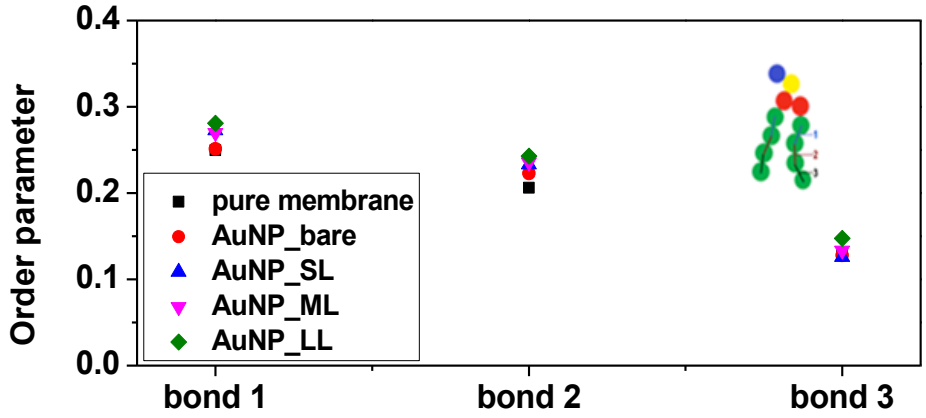

Figure 44. Thickness of lipid membrane during the permeation of AuNP_bare, AuNP_SL, AuNP_ML and AuNP_LL nanoparticles.

We also calculated the order parameter of the tail segment of the lipid membrane to characterize the internal order of the lipid membrane when the nanoparticle is in the lipid membrane region. The order parameter in the bulk is shown in Figure 44. Overall, the bulk order parameters change only slightly upon the insertion of the nanoparticles; minor

structural changes are also observed from Wong-Ekkabut *et al.*'s work in the simulation of C_{60} insertion into a bilayer [98]. The bulk order parameter of the tail segment is slightly larger compared to the unperturbed lipid membrane. We believe this phenomenon is due to the decrease of the dynamic space for the lipid membrane after the insertion of the nanoparticle, which induces lower mobility and lesser extent of isotropic averaging for lipid molecules of the entire lipid bilayer.

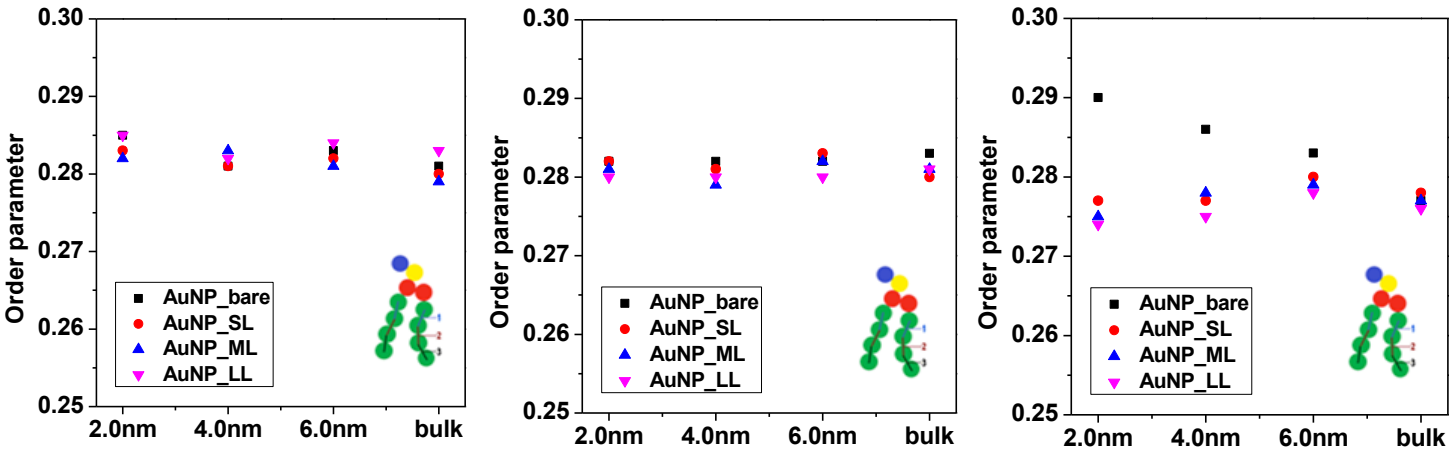

Figure 45. Order parameter of lipid molecule tail segment (bond 1) during the permeation of AuNP_bare, AuNP_SL, AuNP_ML and AuNP_LL nanoparticles for lipid molecules local to the nanoparticle (a) in the entry region; (b) inside the membrane; (c) in the exit region.

Furthermore, we calculate the order parameter for those lipid molecules 2.0 nm, 4.0 nm and 6.0 nm away from the center of nanoparticles. It can be observed in Figure 11 that the local order parameter (bond 1) for bare and ligand-coated nanoparticles shows similar behavior when these particles move into the membrane and stay inside the membrane (Figure 45(a) and (b)), which means the ligands do not have a significant effect on the local

order parameter in these two regions. In the exit region (Figure 45(c)), the tails of the boundary lipids are more ordered during the permeation of a bare gold nanoparticle since the dynamic space for local lipids is more compressed. However, for ligand-coated nanoparticles, local lipid molecules keep their order parameter by changing their orientation. The order parameters for bond 2 and 3 show the same trends reported in Figure 45 and hence are not shown here.

In our simulations, we also observe the structural changes of the ligand-coated nanoparticle. We calculate the size of nanoparticles, which is the average distance from the gold center to the last bead of the nanoparticle (Figure 46(a)). Like the order parameter of the lipid membrane, we obtain the order parameter for the ligands to study how the structure of the nanoparticle itself changes during permeation (Figure 46(b)). It is observed that the size of the nanoparticle increases when it moves into the lipid membrane region, which accompanies the stretching of surface ligands when the particle is in this region. The hydrophobic property of nanoparticles makes it energetically favorable to stay inside the membrane. At the same time, due to the decrease of dynamic space, the ligands become more ordered, compared to their equilibrium value in the aqueous phase. When the nanoparticles move out of the membrane, the size of the nanoparticle reaches a maximum. This occurs because the drag force from lipid molecules makes the ligands stretch more, which may significantly disturb the structure of the ligands of the nanoparticle, making the nanoparticle less compact. We do observe that ligands become less ordered in this region. Furthermore, we notice that the effective size increase of nanoparticles is smaller for those with longer ligands. Also, the bond closer to the surface of gold core (bond 1) is more ordered than the remote ligand bond (bond 2), which indicates that during the permeation

process the nanoparticle with short ligands is more rigid than nanoparticles with long ligands.

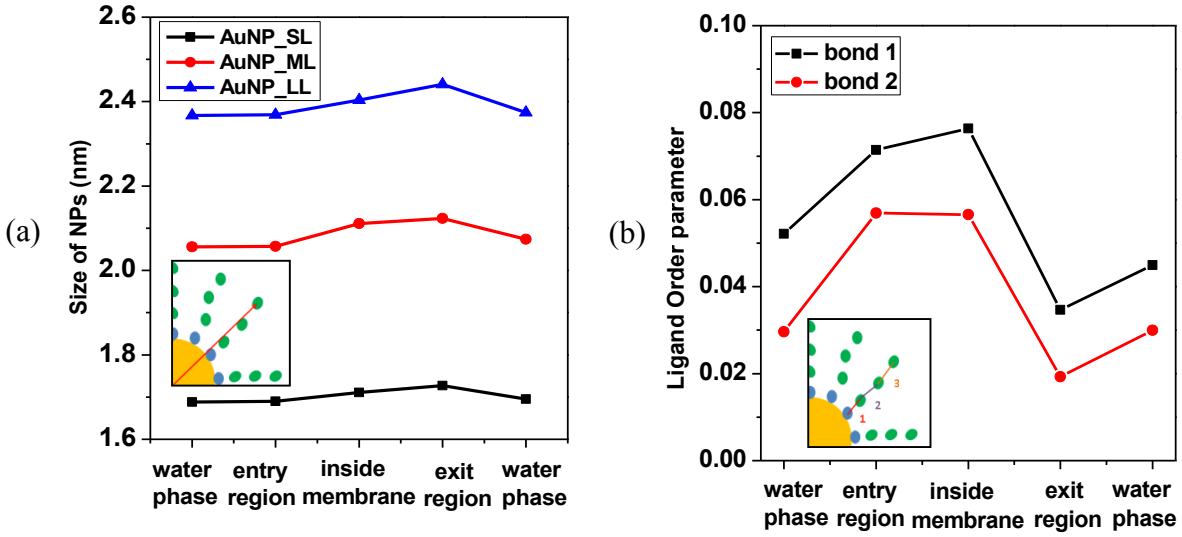

Figure 46. Structural properties of ligand-coated nanoparticles during the permeation process. (a) Size changes for nanoparticles (with various ligand lengths); (b) Order parameter changes of nanoparticle ligands (for AuNP_ML nanoparticle).

As stated in this chapter, water molecules tend to enter the lipid membrane during nanoparticle permeation. In the next chapter, we examine both water and ion leakage into the membrane (cytotoxicity) during nanoparticle permeation.

6 NANOPARTICLE PERMEATION INDUCES WATER PENETRATION, ION TRANSPORT AND LIPID MOLECULE FLIP-FLOP

Nanoparticles are generally considered excellent candidates for targeted drug delivery. However, ion leakage and cytotoxicity induced by nanoparticle permeation is a potential problem in such drug delivery schemes because of the toxic effect of many ions. In this chapter, we carry out a series of CG-MD simulations to investigate the water penetration, ion transport and lipid molecule flip-flop in a protein-free phospholipid bilayer membrane under nanoparticle permeation. The effect of ion concentration, pressure differential across the membrane, nanoparticle size and permeation velocity have been examined in this chapter.

6.1 Introduction

Although water penetration and ion transport in living cells are mainly governed by specific water and ion channels, lipid membranes themselves are not perfect barriers. Instead, water molecules, ions and other hydrophilic molecules have been observed to leak passively in small amounts across a membrane [130-131]. This passive permeation of water molecules and ions is a highly concerted process in which solvent, ion and the pore formation in the membrane are coupled [132]. Such ion leakage and water transport have attracted significant attention because functioning membranes strive to maintain the ionic electrochemical gradient in a variety of activities such as ATP synthesis and transport of nutrients.

Pore formation in membranes during the permeation of nanoparticles has been reported experimentally recently [94]. It has been suggested that water-conducting pores,

which appear in the membrane as defects, can provide a pathway for the translocation of ions [132-139]. Ion leakage and cytotoxicity induced by nanoparticle permeation is a potential problem in drug delivery schemes because of the toxic effect of many ions. Although molecular dynamics simulations have been carried out for nanoparticles in lipid bilayers [25, 35, 97, 140-146], water penetration and ion transport during the permeation of nanoparticles has not been investigated systematically previously. Some important unanswered questions include: How many water molecules and ions may leak during nanoparticle permeation? How do water and ion leakages depend on the physical properties of the nanoparticle (size, shape, permeation velocity)? What if the surrounding environment changes, such as pressure gradient or concentration gradient between two sides of the membrane? How do individual lipid molecules in the immediate vicinity respond when nanoparticle, water and ions permeate simultaneously? The study of nanoparticle permeation mediated water and ion transport through the cell membranes is inherently challenging due to the complexity of the system. Therefore, there is a clear need for physical insight that can help address these and other questions. In a large context, it would be of interest to determine how the nature of such transport and the interactions between lipid membrane and nanoparticles, in particular, may determine the biocompatibility and toxicity of nanoparticles.

Some molecular dynamics simulations studies have been conducted on pore-formation coupled to ion permeation, water penetration and lipid flip-flop in the lipid membrane systems recently [132-136]. In nearly all the previous simulations, the pore formation was induced by an electric field or ionic imbalance between two sides of the membrane. For example, Kandasamy and Larson systematically changed the potential

difference across the bilayers by explicitly varying the number of anions and cations in the two water compartments. At a large enough charge imbalances, dielectric breakdown occurs, leading to the formation of water pores in the bilayers. Anions and cations then translocate through the pore [135]. Gurtovenko *et al.* and Kandasamy *et al.* studied water and ion transport in the protein-free lipid membranes driven by transmembrane ionic charge imbalance [135-136]. Gurtovenko *et al.* explored the lipid flip-flop mechanism induced by a transmembrane ion density gradient [147]. Tepper *et al.* simulated the permeation of protons and ions across lipid membrane by calculating the potential of mean force for the proton and ion of interest as a function of its position in the membrane [132]. Bennett *et al.* described simulations of lipid flip-flop by calculating the potential of mean force using five different models varying from AA, bundled AA, CG (MARTINI), polarizable CG and a CG model with a softer water potential in three different membranes [148]. Given the coarseness of the MARTINI model and the complexity of the flip-flop process and pore formation, the similarity on the PMFs found is encouraging [148].

In chapters 4 and 5, we used the MARTINI coarse-grained model to investigate the permeation characteristics of bare nanoparticles and ligand-coated nanoparticles across model lipid membranes. We also examined the response of the membrane in terms of the structural and mechanical properties of the lipid membrane under the perturbation of nanoparticles. We have observed the formation of transient pores in the membrane during nanoparticle permeation, which motivated us to investigate comprehensively ion transport and water penetration phenomena induced by nanoparticle permeation. In this work, we monitor water molecules in the membrane, ion penetration events, lipid flip-flop phenomena and other characteristics of lipid membranes during the permeation of nanoparticles. The

effect of ion concentration gradient, pressure differential across the membrane, nanoparticle size and permeation velocity are examined. The findings from our work will lead to a better understanding of passive water and ion transport during permeation of nanoparticles and help in developing more efficient nanocarrier drug delivery systems while avoiding cell cytotoxicity.

6.2 Simulation System Setup

The lipid membrane system in the present work consists of 512 DPPC molecules and approximately 23000 CG waters (4 water molecules in each CG water) in a 12.8×12.6×22.2 nm^3 simulation box. We have previously shown that this bilayer membrane self-assembles from the isotropic solution of lipids in CG simulations in Chapter 3 and that the properties of the self-assembled bilayers are in good agreement with experimental measurements, which validate the effectiveness of the coarse-grained model we are using for the lipid bilayers.

To replicate the actual experiments in which the membrane was supported on a pore-spanning solid to prevent the entire membrane from moving, we simulated a solid support by tethering the boundary lipid molecules to their initial position with a harmonic spring force. Lipids 1 nm from each end (about 8% of the total membrane width) are tethered in our simulation system. Two impermeable walls are inserted in our simulation system, separating the water phase into two independent compartments, as seen at the top and bottom of the simulation box in Figure 47. These two walls are impermeable to water and ions and are cut from a face-centered cubic (FCC) structure. To create a pressure differential

across the membrane, the wall on the topside is moved towards the lipid bilayers at a velocity 0.025 m/s for 10 ns and the system is then allowed to relax for another 10 ns for equilibrium. We created three pressure differentials by repeating this movement three times. The top wall is moved by a total distance of 0.75 nm, creating a maximum pressure differential of 300 bars between two sides of the lipid membrane. Our studies indicate that after 10 ns relaxation, the lipid membrane does not change significantly and appears to be close to equilibrium. For simulations involving ions, sodium and chloride ions are added to the water phase by replacing randomly chosen water molecules. We inserted each of 600 sodium and chloride ions, corresponding to a concentration of about 1.3 mole percent (the saturation limit of salt in water is 1.8 mole percent). We inserted equal number of sodium and chloride ions in both water compartments to examine a system with no concentration gradient across the membrane (equal ion concentrations on both sides). In further studies, we only include sodium and chloride ions in the top compartment to examine systems with ion concentration gradients (unequal ion concentrations).

After allowing the equilibration of the system, we introduce one bare gold nanoparticle into our simulation system, as shown in Figure 47. The structure of the gold nanoparticle is obtained by cutting nearly spherical nanocrystals out of a bulk gold FCC lattice. In this study, various sizes of nanoparticle are investigated, from 1.0 nm to 4.0 nm in diameter. We also examined the effect of the nanoparticle permeation velocity in this study, by inducing the nanoparticle to permeate at various velocities in the range of 0.35, 0.525, 0.7 and 1.4 m/s respectively (velo1/2/3/4).

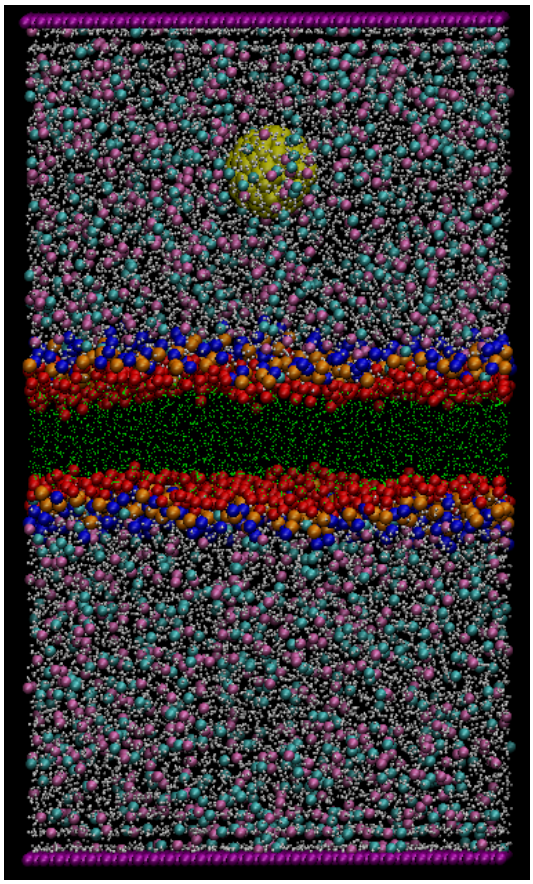

Figure 47. The simulation system for investigating the nanoparticle permeation induced water penetration and ion transport (Yellow represents the gold nanoparticle, Cyan represents the Sodium ions, while purple dots are Chloride ions).

In this study, the number of CG water molecules reported in the interior of the membrane corresponds to water molecules in the hydrophobic interior of the membrane. This region is defined as a slice extending 0.75 nm on either side of the center of the membrane. The water molecules located at the openings of the pore are therefore not counted. A penetration event is defined as the diffusion of an ion moving from one boundary (defined by the average position of phosphate groups) in one layer to the other. Finally, we define a flip-flop occurrence as an event in which a lipid molecule moves from one leaflet of the bilayer to another. Lipid flip-flop is infrequently observed in fully intact

bilayers due to the high free energy barrier involved in moving the polar head groups through the hydrophobic core. In intact planar-supported lipid bilayers, sum- frequency vibration spectroscopy has been used to measure the intrinsic rate of a flip-flop for bilayers consisting of protonated and perdeuterated lipids. An average free energy barrier for flip-flop of 220 kJ/mol for DPPC and two other lipids, 105 kJ/mol for DSPC was found [149-150]. This phenomenon has been observed experimentally during lipid fusion or under the perturbation of bilayer-disrupting peptides [151]. Electric pulses have also been shown to enhance the transbilayer mobility of phospholipids [152].

6.3 Lipid Membrane under Compression

The two walls we designed are impermeable to water or ions and the lipid bilayers are located at the center of the simulation box as seen in Figure 47. The equilibrated density profiles of phosphate groups and water molecules along the z-direction in lipid/water system are shown in Figure 48 (a). The thickness of lipid membrane, which is obtained from the distance between the phosphate groups, is 3.78 nm, in close agreement with the experimental value of 3.85 nm [67]. The upper impermeable wall was then moved toward the lipid bilayers to create the pressure differential in our simulation system. To maintain the stability of the system, low compression rates (0.025 m/s) and long relaxation times (10 ns) between each wall movement were used in this work. From the comparison of the density profiles of phosphate group and tail group of the lipid membrane (Figure 48(b) and (c)) under various pressure differentials (press1/2/3) after the relaxation time compared with the original system (press0), the structure of the lipid membrane does not change significantly.

The thickness of the lipid membrane shrinks by only 3.2 % under a 300 bar pressure differential between the two sides of the membrane, which is shown in Table 9.

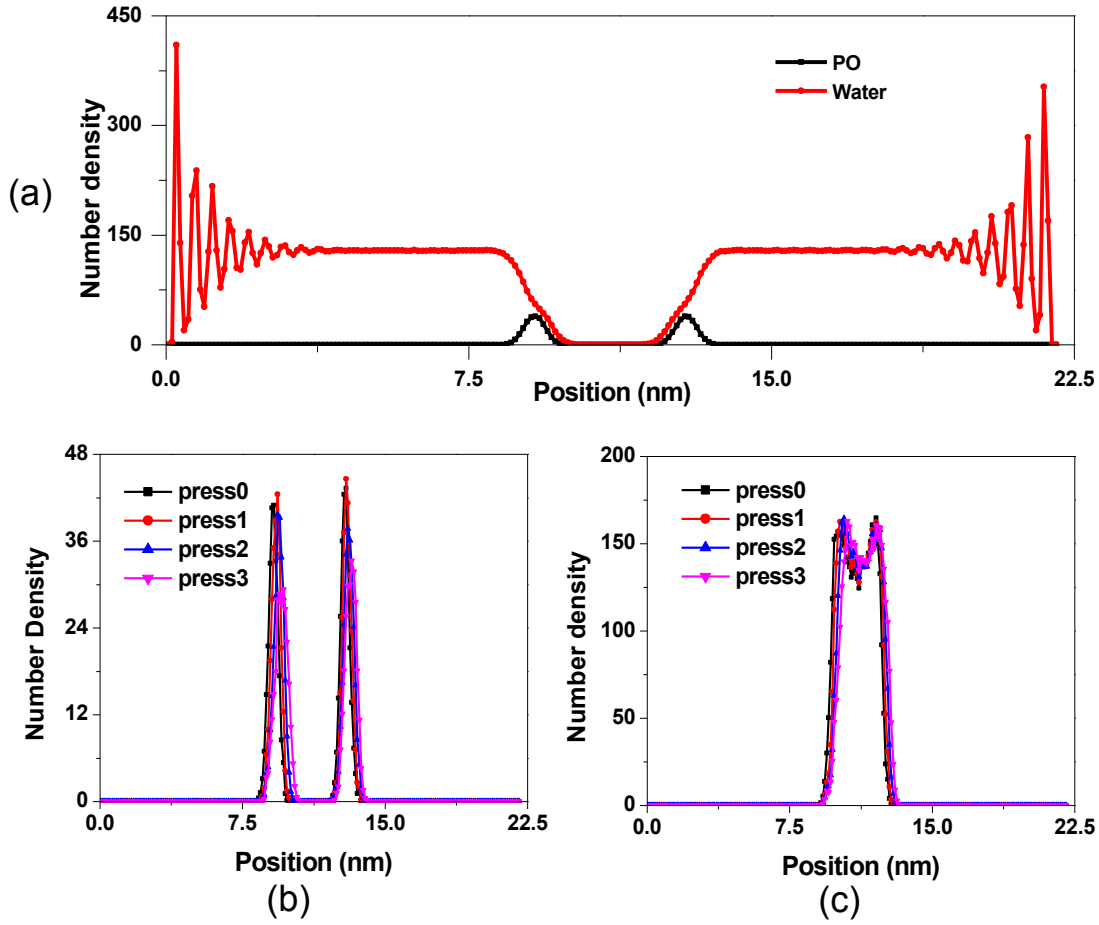

Figure 48. Density profiles of components of DPPC membrane along z direction. (a) Equilibrated lipid/water system after the insertion of two impermeable walls without compression. (b) Density profiles of phosphate groups under various compression. (c) Density profiles of tail groups under various compression.

Table 9. The thickness of lipid membrane under various pressure differences.

Simulation system	Thickness (nm)
Press0	3.78
Press1	3.74
Press2	3.69
Press3	3.66

6.4 Water Penetration

Microscopy experiments have examined the formation of nanoscale holes caused by nanoparticles in model membranes. For example, Chen *et al.* observed dendrimer nanoparticles making 3.0 nm diameter holes in living cell membranes [96]. In our previous simulation of the permeation of various sizes of nanoparticles (bare and ligand-coated nanoparticles) across the lipid membrane, we also observed the pore formation inside the membrane. In this chapter, we have focused on water penetration more comprehensively. We have investigated the dependence of water penetration on nanoparticle size, permeation velocity, pressure and ion concentration gradient.

As is seen in Figure 49, water molecules start entering the lipid bilayer region when the nanoparticle touches the first layer of the membrane. The lipid molecules are compressed when the nanoparticle permeates the membrane, inducing defects in the interior of the membrane and a pore is therefore created. The number of water molecules entering the membrane increases as the nanoparticle moves through the membrane. The deeper the nanoparticle goes into the membrane, the more water molecules are observed. The number of water molecules penetrating the membrane is higher while the nanoparticle is permeating the head group of the first lipid bilayer. It slows down somewhat while it is permeating the tail region of the first bilayer. It increases significantly once more while the nanoparticle permeates the tail region of the second lipid bilayer. The structure of the lipid bilayer maintains its integrity until the nanoparticle starts permeating the second layer tail region. Once it enters this exit region the membrane structure is significantly disturbed as confirmed by the lipid order parameter, which has been shown in chapter 5. This then results in a significant increase in the pore size and the resultant water molecules inside the membrane.

When the nanoparticle leaves the membrane and enters the second water phase, water molecules also move out of the membrane. This exit of water molecules results from the recovery of the membrane and the hydrophobicity of the lipid membrane interior.

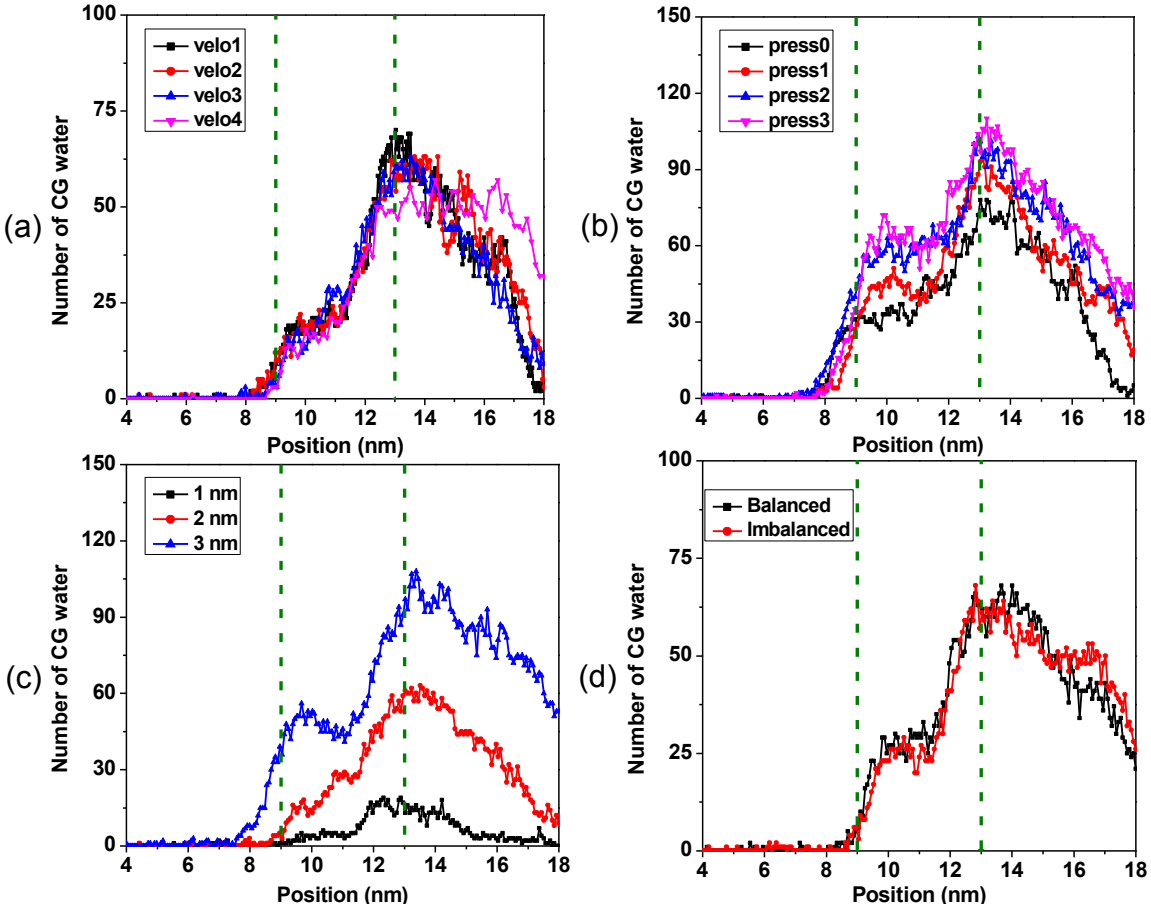

Figure 49. Number of water molecules in the interior of membrane under various conditions. (a) The nanoparticle permeation velocity effect, which is from 2.0 nm nanoparticle, balanced concentration and press1 system. (b) The pressure effect, which is obtained from 3.0 nm nanoparticle, 0.7 m/s nanoparticle permeation velocity and imbalanced concentration system. (c) The size effect, which is obtained from balanced concentration, 0.7 m/s nanoparticle permeation velocity and press2 system. (d) The potential gradient effect, which is obtained from 2.0 nm nanoparticle, 0.7 m/s nanoparticle permeation velocity and press3 system. (The green dash line indicates the equilibrated position of phosphate groups)

The number of water molecules inside the membrane does not appear to be affected by the permeation velocity of the nanoparticle. However, the rate of recovery of the lipid membrane, as indicated by the exit of the water molecules from inside the membrane, decreases with the nanoparticle permeation rate, as can be seen in Figure 49(a). The smaller the permeation velocity, the easier for lipid membrane to recover after the nanoparticle permeation. An increase in the pressure differential between the two sides of the membrane increases water penetration (Figure 49(b)). More water molecules enter the membrane interior when the nanoparticle is permeating under high-pressure differentials. The recovery of the membrane also slows down under larger pressure-differentials. Larger nanoparticles also lead to more water inside the lipid membrane, as seen in Figure 49(c). In addition, larger nanoparticles disturb the internal structure of the membrane, which in turn elevates the changes in the local order parameter (chapter 5), and therefore makes it harder for the membrane to recover. Finally, we found that ion concentration gradients across the membrane as described in the studies below do not affect water penetration in the membrane (Figure 49(d)).

6.5 Ion Transport

We now examine ion transport induced by nanoparticle permeation. Due to the coulombic interaction between charged lipid head groups and the ions and the hydrophobic properties inside the membrane, these ions get bound to the lipid head groups and are therefore unable to penetrate to the center of membrane on their own. The snapshots of a nanoparticle-mediated ion transport are shown in Figure 50. When the nanoparticle touches the membrane surface, some ions are pushed into the water-membrane interface, along with

the deformation of the first layer and the formation of water pore inside the membrane. As the nanoparticle permeates farther inside the membrane, most ions return to the water/membrane interface, except for a few ions that continue to move along with the nanoparticle. These ions translocate to the center of the membrane once the nanoparticle moves completely across the first layer. Once the nanoparticle begins to enter the tail group of the second bilayer, as was reported earlier a larger pore is created inside the membrane. This increases the number of water molecules in the membrane, which also leads to a corresponding increase in the number of ions inside the membrane. The number of ions inside the membrane reaches its maximum value as the nanoparticle is exiting the membrane.

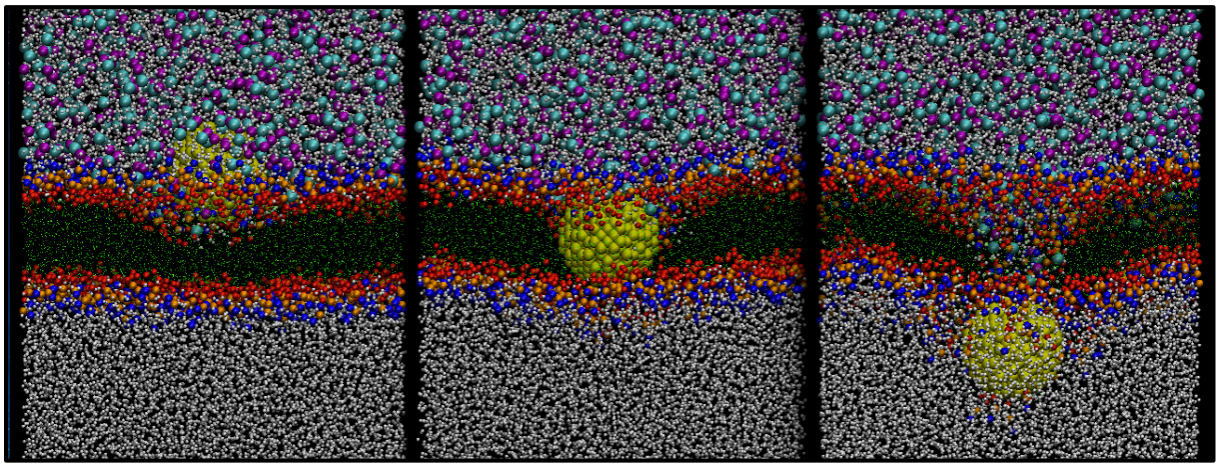

Figure 50. Typical snapshots for the water and ion translocation mediated by a 3.0 nm nanoparticle permeating the membrane.

A summary of the 32 independent simulations to monitor the ion penetration events is presented in Table 10. An ion penetration event as described earlier is defined as the

diffusion of an ion moving from one boundary that is the average position of phosphate groups in one layer to the other. Ion penetration is clearly sensitive to the size of nanoparticles. For diameters in the range of 1.0 – 4.0 nm, the number of permeation events increase exponentially as the size of nanoparticle increases. No ion penetration event is observed during the permeation of the 1.0 nm nanoparticle, which is not shown in Table 10. Larger nanoparticles increase the size of the created pore, which increases the incidence of penetration events for the ions. If we examine the case of no ion concentration gradient and press1 system as an example, 4 ion penetration events with a 2.0 nm nanoparticle, 14 for a 3.0 nm nanoparticle, while the number of penetration events reaches 119 with a 4.0 nm nanoparticle. With zero external pressure and no concentration gradient we still observed ion penetration accompanying permeation of nanoparticles larger than 1.0 nm diameter.

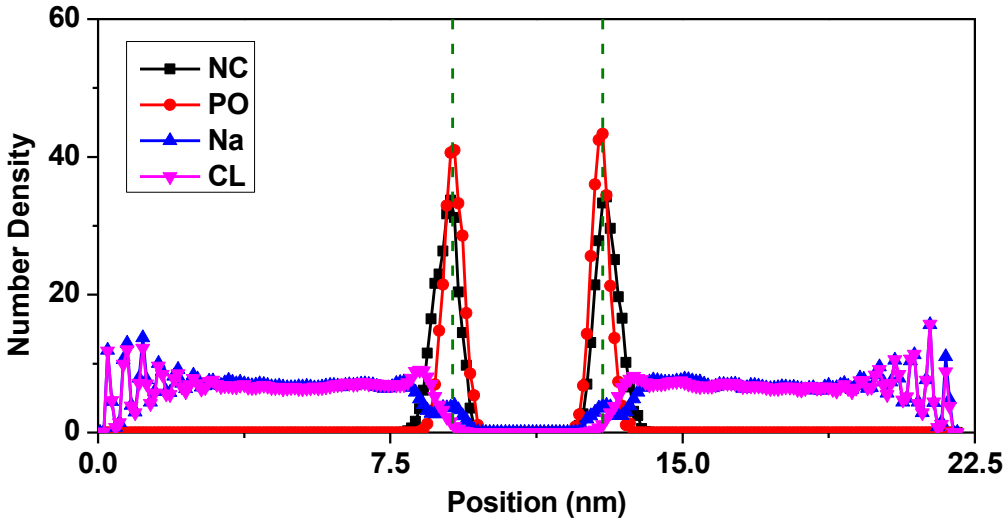

Figure 51. Density profiles of Sodium and Choline ions, chlorine and phosphate groups of equilibrated lipid/water/ion system.

Table 10. Summary of ion penetration events under various conditions.

size (nm)	concentration	pressure	velocity	Na^+	Cl^-
2	balanced	press1	velo1	0	1
2	balanced	press1	velo2	1	1
2	balanced	press1	velo3	0	0
2	balanced	press1	velo4	1	0
2	balanced	press0	velo2	2	0
2	balanced	press2	velo2	0	0
2	balanced	press3	velo2	0	1
2	imbalanced	press1	velo1	0	0
2	imbalanced	press1	velo2	0	0
2	imbalanced	press1	velo3	1	1
2	imbalanced	press1	velo4	0	0
2	imbalanced	press0	velo2	2	0
2	imbalanced	press2	velo2	0	0
2	imbalanced	press3	velo2	0	0
3	balanced	press1	velo1	1	2
3	balanced	press1	velo2	2	3
3	balanced	press1	velo3	2	2
3	balanced	press1	velo4	2	0
3	balanced	press0	velo2	2	2
3	balanced	press2	velo2	2	2
3	balanced	press3	velo2	3	2
3	imbalanced	press1	velo1	2	2
3	imbalanced	press1	velo2	1	4
3	imbalanced	press1	velo3	2	3
3	imbalanced	press1	velo4	2	2
3	imbalanced	press0	velo2	2	2
3	imbalanced	press2	velo2	4	3
3	imbalanced	press3	velo2	6	4
4	balanced	press1	velo1	9	15
4	balanced	press1	velo2	13	18
4	balanced	press1	velo3	12	20
4	balanced	press1	velo4	12	20

The equilibrated density profiles of sodium and chloride ions on both sides of the membrane in the absence of nanoparticles are shown in Figure 51. We observe that the sodium ion concentration peak is near the position of the phosphate group, while for

chloride ions, a peak is observed in the interfacial layer near the membrane. The results in Table 10 do not show any selectivity for ions for penetration of nanoparticles up to 2.0 nm in size. This is most probably because the pores formed are not large enough for the hydrated ions, for all pressures and concentrations. For 3.0 nm particles, the nanoparticle permeation velocity does not appear to change the ion penetration events, as was observed in the case of water (see Figure 49(a)). In the case of unequal sodium chloride concentrations, the overall number of penetration events is larger compared to equal concentrations. The pores created here are large enough for hydrated ions to move inside the pore, so the additional chemical potential gradient due to unequal ion concentrations provides an additional driving force to facilitate ion transport. However, we do not observe any ion selectivity, either for 2.0 nm or 3.0 nm nanoparticle permeation. In the case of equal concentrations, pressure differentials do not appear to affect the ion penetration rate or selectivity. For the unequal concentrations, the overall ion penetration events increase significantly between the lowest pressure and higher pressures, but we do not observe any clear indication of selectivity. Therefore it appears that the combination of the chemical potential and hydrostatic driving force facilitates ion flow in the pores. In the absence of a chemical potential driving force, pressure differences alone cannot overcome the flow barriers in the transient pores created by the 3.0 nm particles permeating the membrane. With even larger particles, every factor that previously did not affect ion permeability or selectivity becomes important. For example for 4.0 nm particles, permeation velocity of the nanoparticle, which played no role previously, affects both the ion permeation rate and selectivity. There appears to be a bias for chloride transport. This has to do with the lower surface charge density of chloride ions which makes the hydrated ions more flexible, which

enables chloride ions to more easily pass inside the pores formed. The latter behavior has been also observed in semirigid pores such as carbon nanotubes [153]. Simulations of ion permeation of in pre-formed tension-stabilized pores in DPPC by Leontiadou *et al.*[134] also show that for larger pores (1.8 nm in radius), the chloride ion flux was an order of magnitude larger than that of the sodium ions.

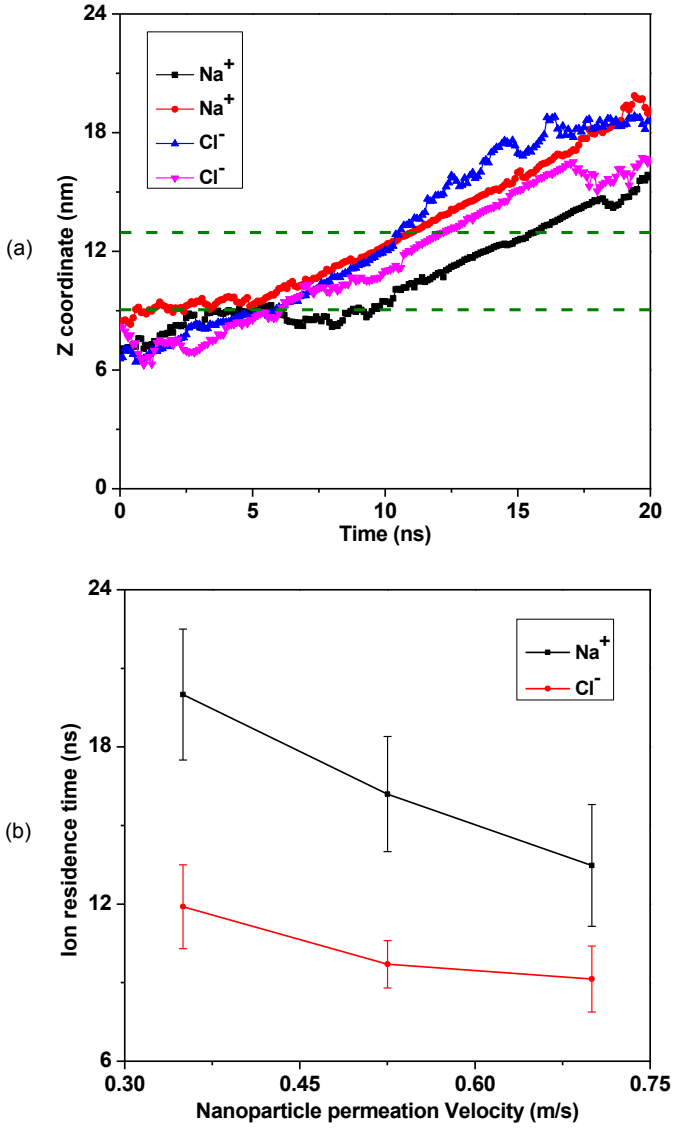

Figure 52. Typical Na+ and CL- ion trajectory (a) and ion residence time (b) in the membrane the nanoparticle permeation. (Green dash line indicates the equilibrated position of phosphate group). The two Na^+ and Cl^- are randomly chosen.

Figure 52(a) shows typical ion trajectories for two randomly chosen sodium and chloride ions, from which we see the sodium ions present a strong tendency to stay in the lipid membrane head group region once they get close to the first layer of the membrane, while chloride ions prefer to stay in the interfacial layer near the membrane. Once chloride ions touch the membrane, they quickly penetrate and cross the membrane. The average residence times for sodium and chloride ions inside the membrane are shown in Figure 52(b). Although the residence time for both sodium and chloride ions have a wide variation, the residence time for sodium ions is much longer than for chloride ions. Such anionic selectivity has also been reported experimentally for large pores stabilized by specific cationic lipids [154] and theoretically from Leontiadou et al. 's work [134] and Gurtovenko's work [136], in which the water pore is mediated by external electronic field and ion potential gradient.

6.6 Lipid Molecule Flip-Flop

When a lipid molecule moves from one leaflet of the bilayer to another, it is said to have flip-flopped. The lipid molecule flip-flop phenomenon (transmembrane lipid translocation) is of significant biological importance because such translocation process is involved in a variety of properties and functions of cell membranes, such as membrane asymmetry and stability [155], modulation of the activity of membrane proteins [156] and programmed cell death [157]. Molecular simulations can provide insight to understand the molecular mechanisms of such flip- flops. To complete the permeation of chemical species across a biological membrane, lipid molecule flip-flop may take place with the help of proteins or without them. There are strong indications that lipid translocation across a lipid

membrane is a pore-mediated process and a major fraction of flip-flops takes place through defects in the lipid membranes [158-161].

During the nanoparticle permeation process, we witness spontaneous translocation of lipid molecules from one membrane leaflet to another following the formation of a water-conducting pore inside the membrane. When the nanoparticle gets close to and begins to permeate into the membrane, the head groups of lipids in the first layer are compressed to make room for the nanoparticle cross-sectional area and the lipid tails are separated apart. At the same time, water molecules start to penetrate into the membrane, pushing some lipid molecules toward the center of the membrane. Those lipid molecules may therefore have a chance to cross the hydrophobic core region as part of the transient water-conducting pore. We found some lipid molecules undergo flip-flop events very quickly, while most of the flip-flopped lipid molecules spend some time to overcome the high free energy barrier involved in moving the polar head groups through the hydrophobic core. Nevertheless, our observations typified by the snapshots in Figure 53, on the basis of approximately 500 flip-flop events observed in all our simulations, indicate that lipid molecules undergoing the process progress through a series of similar-looking stages. As a lipid molecule moves along the z-direction from one layer to the other, an end-over-end molecular rotation occurs, during which the two alkyl tails open up and then come together again. The snapshots of six typical lipid molecule flip-flop events observed in our simulation are shown in Figure 53. In Figure 53 (a), we display 10 snapshots of a particular lipid undergoing a flip-flop. In the process, it undergoes conformational changes and overall rotation while translating along the z direction. In Figure 53 (b), each of the 5 lipid molecules being observed likewise

translated along the z direction, but to save space we suppress the z translation in this part of the figure.

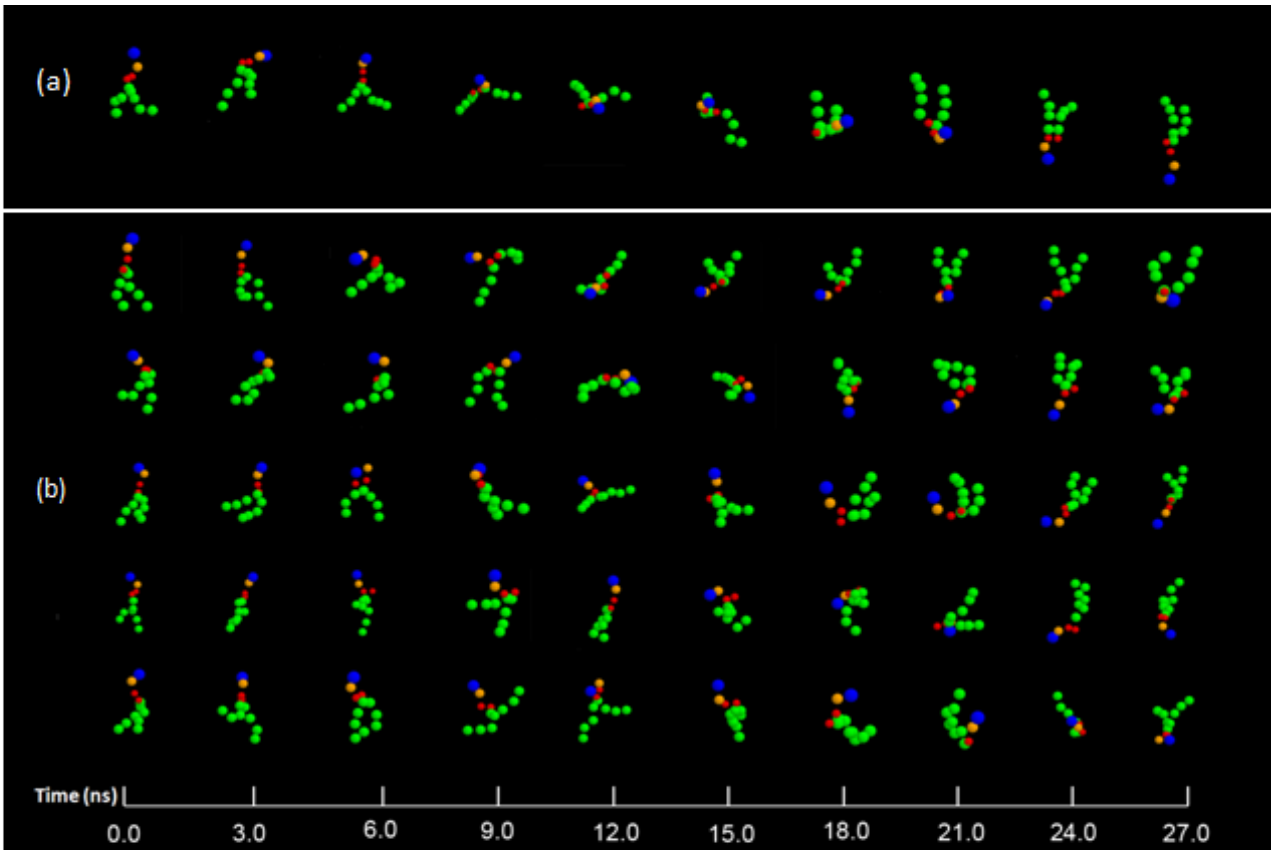

Figure 53. The scheme (a) and the snapshots (b) of typical lipid molecule flip-flop events observed in our simulation, which are obtained from 3.0 nm nanoparticle permeation (0.525 m/s permeation velocity) under unequal ion concentration and press1 system.

The water molecules in the transient pore play a role in the flip-flop events. Water interaction with the polar head groups assist in the process. The instantaneous number of water molecules in the interior of the membrane and the number of lipid molecules no longer present in their original layer are shown in Figure 54. The water molecules included in the count are those whose z coordinates are within 1.5 nm of the center of the membrane.

The lipid molecules included in the count are those whose head group z coordinates are no longer within 3.0 nm of their original equilibrium position. The lipid flip-flop events start to show up when the nanoparticle permeates into the membrane. As the nanoparticle permeates deeper into the membrane, the number of flip-flop events increases, reaching their maximum where the water molecules in the interior of the membrane reach their maximum. In the snapshots in Figure 55, only the slice of the simulation box that includes the nanoparticles is shown for clarity, and only the lipid molecules (not water or ions) in the marked region are shown in the inset. These lipid molecules are in configurations typical of stages in the flip-flop process shown in Figure 53. This confirms our interpretation of the summary in Figure 55, that most of the flip-flop events occur in the "wake" of the nanoparticle with high incidence of water molecules inside the membrane accompanying the flip-flopping lipid molecules.

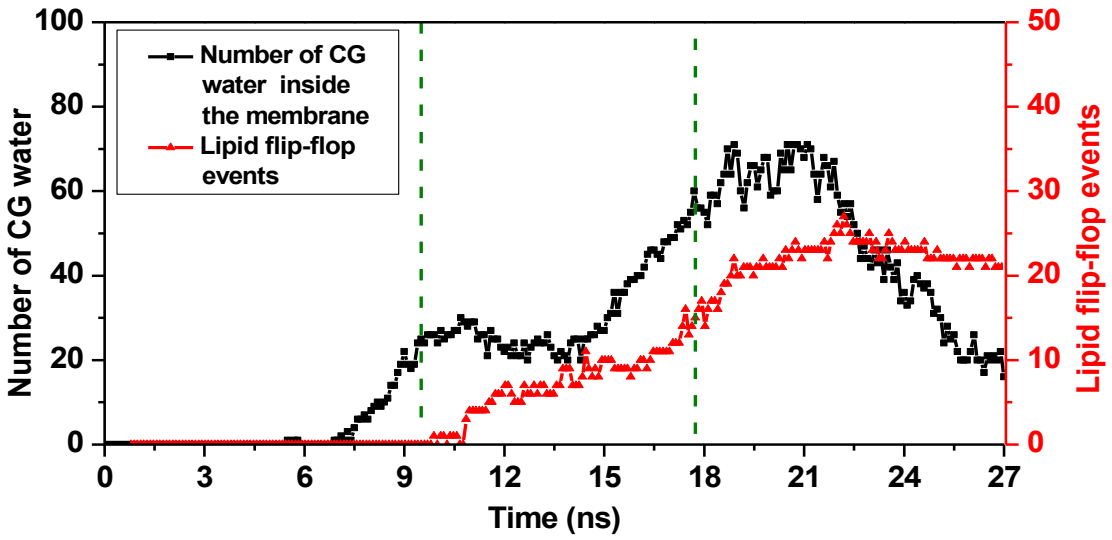

Figure 54. Number of water molecules in the interior of membrane and the instantaneous lipid molecule flip-flop events, which are obtained from 3.0 nm nanoparticle permeation (0.525 m/s permeation velocity) under unequal ion concentration and press1 system. (The green dash line indicates the time during which the center of the nanoparticle is within the membrane.)

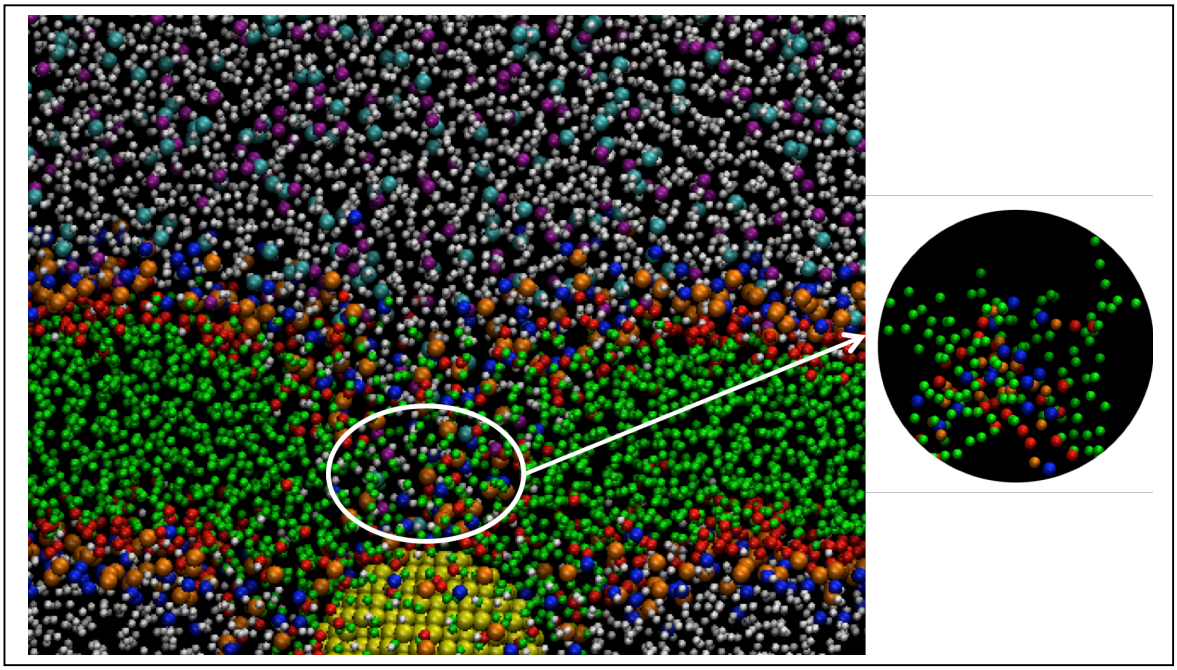

Figure 55. Snapshot showing lipid molecule flip-flops as the nanoparticle is moving out of the membrane. For clarity only a section of the simulation box is shown. The inset shows only the lipid molecules in the marked region.

The stages in the mechanism of lipid flip-flop events we observed in our simulations are in agreement with the observations from atomistic simulations by Gurtovenko *et al.* [147], where the lipid flip-flops in a pre-formed pore are induced by a transmembrane ion density gradient. Both "fast lipid flip-flops" (10 – 20 ns) and "slow flip-flops" (up to 130 ns) are observed in their simulations [147]. In our simulations, the time for the lipid flip-flop relates to the nanoparticle permeation velocity because the occurrence of water-conducting pores in the membrane is caused by the permeation process of nanoparticle. In a typical simulation run (a few examples are shown in Figure 53), the time for lipid molecule flip-flops varies from 3 ns to 27 ns, which is well in agreement with atomistic simulations if we consider the speed-up factor of 4 in our coarse-grained simulations.

We investigated how the number of incidences of flip-flops varies with conditions. Figure 56 (a-c) summarizes the correlation of lipid flip-flop events observed with nanoparticle size, permeation velocity, pressure and ion concentration differential. We found the number of lipid molecules that flip-flop decreases as we increase the nanoparticle permeation velocity (Figure 56 (a). Larger permeation velocities lead to shorter lifetime of pores in the interior of the membrane, which diminishes the available time for such flip-flops. As seen in Figure 57, the lifetime of the transient pore decreases significantly when the permeation velocity is below 0.7 m/s, while there is no significant change when the permeation velocity is above 0.7 m/s. We therefore observed that when the permeation velocity is over 0.7 m/s, for most cases, the number of lipid flip-flops reach a limiting value and no longer change with velocity. The number of lipid flip-flops decreases with the pressure differential between two sides of the membrane (Figure 56 (a)). Although the penetration of water molecules increases as the pressure increases, higher pressures lower the mobility of the lipid molecules because of membrane compression, making flip-flops less frequent. As seen in Figure 56 (b) and (c), the number of flip-flopped lipid molecules is affected by the ion concentration differential and the size of the nanoparticle. A concentration gradient between two sides of the membrane, as shown earlier, facilitates ion transport through the water pore. Such ion transport quickly discharges the transmembrane ionic charge imbalance and makes the water pore more stable [136], which can lead to enhanced flip-flops. Also, with larger diameter nanoparticles, higher water and ion penetration is observed; both in turn increase the number of lipid molecule flip-flops that occur.

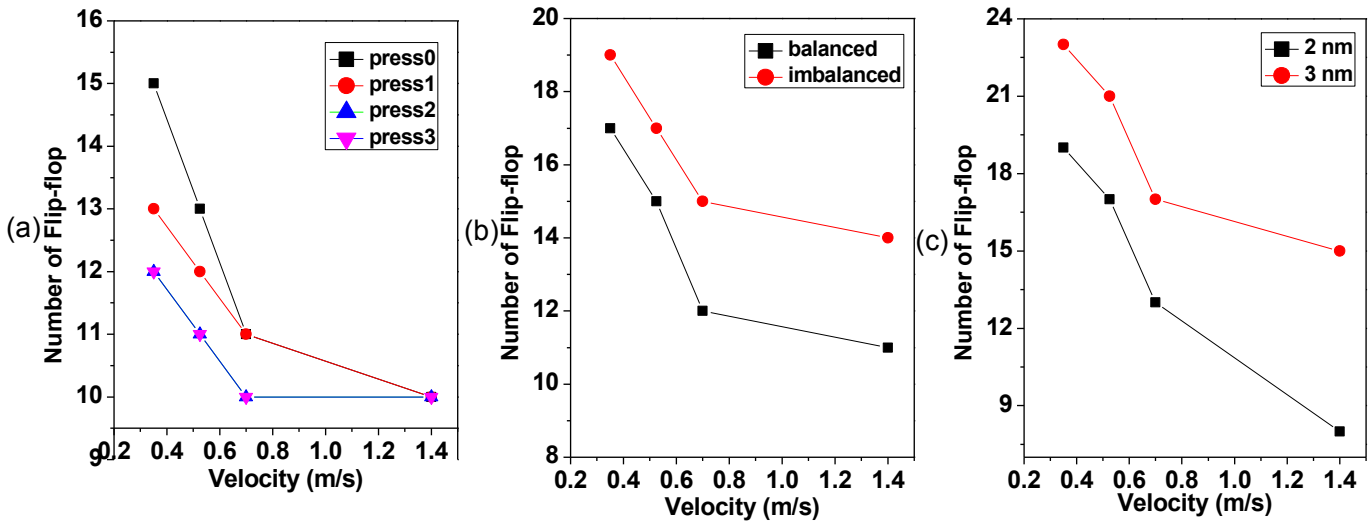

Figure 56. Lipid molecule flip-flop events under various conditions. (a) The effect of pressure differential and nanoparticle permeation velocity, which data is obtained from simulations with 2 nm nanoparticle and equal ion concentration. (b) The effect of potential gradient, which data is obtained from simulations with 3 nm nanoparticle under press1. (c) The effect of nanoparticle size, which data is obtained from simulations with unequal ion concentration under press1.

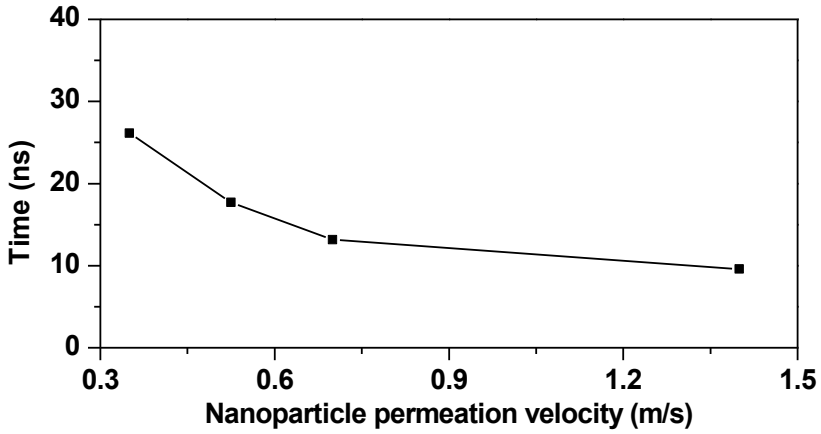

Figure 57. Pore lifetime as a function of nanoparticle permeation velocity (data obtained from simulations with 2.0 nm nanoparticle under equal ion concentrations and under press2).

6.7 After The Permeation

It is known that the permeation of nanoparticle and the accompanying water and ion flux can affect the stability and the mechanical strength of the lipid membranes [88]. It is therefore important to understand if and how a membrane recovers following the nanoparticle permeation. We have investigated the thickness, order parameter and related properties to understand the nature of any permanent changes, if any, occur following the nanoparticle permeation. To observe the recovery of the lipid membrane, we held the nanoparticle in place and continued the simulation for an additional 10 ns after the nanoparticle has permeated the lipid membrane and reached the other side. (This was accomplished by stopping the movement of the nanoparticle and tethering it at the bottom end of the system – see Figure 47.) We refer to the property averages obtained in the additional 10 ns as "at the end"; and the property averages for the equilibrated unperturbed membrane as "at the beginning".

The thickness of the lipid membrane begins to increase once the nanoparticle reaches the surface of the lipid membrane, compared to its equilibrium undisturbed condition. After the nanoparticle moves into the membrane, the thickness of the membrane increases quite significantly from its equilibrium value. Larger nanoparticles induce more perturbations in the lipid membrane, resulting in a greater increase in the thickness. In all the simulations we have carried out here, we observed that the thickness of the lipid membrane completely recovers after permeation by a nanoparticle, which confirms the healing ability of membranes. Figure 58 shows the density profiles of phosphate and tail groups at the beginning and at the end in two typical simulations (Case1: 2 nm nanoparticle, 0.7 permeation velocity, equal ion concentration and press3 system; Case2: 3 nm nanoparticle,

1.4 m/s permeation velocity, unequal ion concentration and press1 system). The density profiles for phosphate and tail groups change slightly after the nanoparticle permeation. This is expected since lipid membranes have been observed to self-assemble even from an initial random configuration of lipids in solution in our work. We witnessed a few lipid molecules being dragged out to the bulk solution, making the bare nanoparticles appear as a ligand-coated nanoparticle. This explains the small peak observed in the density profile (Figure 58) of phosphate and tail groups at the end of our simulations.

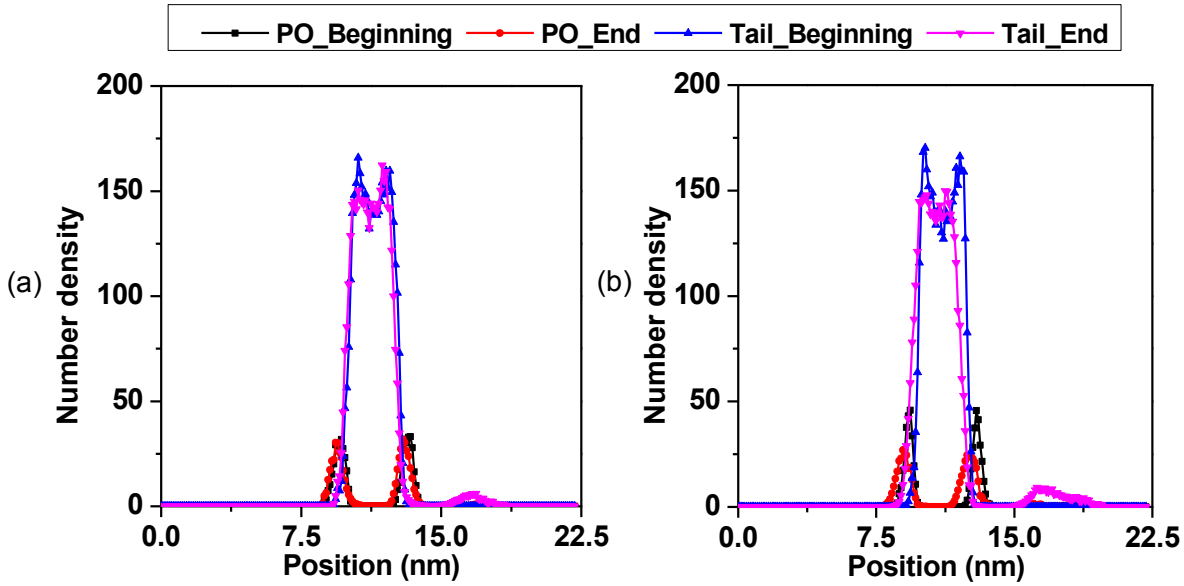

Figure 58. Comparison of density profiles of PO and tail groups of DPPC membrane along z direction at the beginning of the simulation and at the end of the simulation after tethering the nanoparticle for 10 ns. (a) Case 1: Simulation system with 2 nm nanoparticle, 0.7 m/s permeation velocity, balanced concentration and press3 system. (b) Case 2: Simulation system with 3 nm nanoparticle, 1.4 m/s permeation velocity, imbalanced concentration and press 1 system.

We also monitored the tail segment order parameter. The order parameter is slightly larger during the nanoparticle permeation, compared to the unperturbed lipid membrane, which is consistent with our previous work in chapter 4 and 5. This is due to the decrease of the dynamic space for the lipid membrane after the insertion of the nanoparticle, which

induces lower mobility and lesser extent of isotropic averaging for lipid molecules of the entire lipid bilayer. However, 10 ns after the particle has permeated, the order parameter reverts back to the unperturbed value. Since the lipid molecules had been individually tagged, we found a small fraction of the first layer lipids in the second layer and vice versa, after recovery of the membrane. Since both layers had the same lipid composition to start with, this leads to no net change in the lipid composition of the two layers. Overall the membrane shows excellent recovery to its original structure.

In the study discussed here, a force was applied only one side of the membrane to develop a pressure imbalance, we study the effect of an external pressure applied on both sides of the membrane to investigate changes in its mechanical and structural properties under such compression in the next chapter.

7 INVESTIGATION OF THE COMPRESSIBILITY OF A LIPID MEMBRANE

The ability of cell membranes to deform is important for many biological processes including membrane fission and fusion, intracellular transport of materials and intracellular endocytic trafficking. Experimental techniques developed for measuring deformations include and atomic force microscopy, X-ray diffraction, and fluctuation spectroscopy. Such experiments are both time consuming and expensive. Molecular dynamics simulations are therefore an attractive alternative to reduce the number of experimental studies, and to extrapolate to conditions that are difficult to access experimentally. In this chapter a more direct route to obtain the compressibility of membranes is presented. Comparing with previous simulations and experimental results validates this method. We have also used this method to predict membrane behavior for conditions not studied experimentally.

7.1 Introduction

Lipid bilayers form the basic structural framework of biological membranes and act as substrates for other species such as proteins to function effectively. The ability of cell membranes to deform is important for many biological processes such as membrane fission and fusion (important in understanding many virus infections [162]), intracellular transport of materials (key to cellular entry mechanisms[163]) and intracellular endocytic trafficking (critical importance in viral assembly and budding [164-165]) etc. Membrane mechanical properties such as compressibility play a key role in understanding the deformation behavior of cellular membranes. For example, the elastic behavior of lipid bilayer is closely related to the stability and activity of biological cells [166]. Red blood cells while capable of assuming many shapes are only biologically active when they are in the biconcave shape. It is also

well documented that external pressure on biological systems can excite membranes. The reversal of anesthesia by application of a sufficiently large hydrostatic pressure is one such example [167]. Finally, the mechanical stability of cells is often destroyed when a membrane is under electric force compression [168]. It is therefore not surprising that understanding the compressibility of membranes is key to predict membrane behavior and will be the main focuses of present study described here. In this chapter, we will present a simplified approach for investigating the compressibility of lipid membranes. The new method can measure membrane compressibility very efficiently using smaller system sizes, while providing detailed information on how the lipid membrane reacts to different external forces such as compression, permeation of molecules, and deformation. These external forces generally lead to changes in membrane thickness and shape. Our MD results are also compared with previous MD studies and available theoretical and experimental results, and are used to gain insight into many observed phenomena.

7.2 Simulation Setup

We use the system setup shown in Figure 59 to study the compressibility of the DPPC phospholipid bilayers membrane under external pressure. The lipid bilayer was formed by self-assembly and size of the simulation system is $6.32\times6.46\times11.5$ nm^3. The pressure on the membrane was created by incorporating two impermeable thermally fluctuating walls at the top and bottom of the system (orange wall shown in Figure 59). These two walls are impermeable to water and were cut from a face-centered cubic (FCC) structure. To create an external pressure the walls were moved towards the lipid bilayers (in the directions denoted by the arrows in Figure 59) at a rate of 0.27 m/s for 1 ns and then the

system was allowed to relax for 2 ns. Our studies indicate that after 2 ns the system did not change significantly and appeared to be close to equilibrium. The pressure on the membrane was then measured and membrane thickness was calculated from the density profiles collected during the relaxation period. This procedure was repeated and resulted in developing pressures of up to 68.6 kbar.

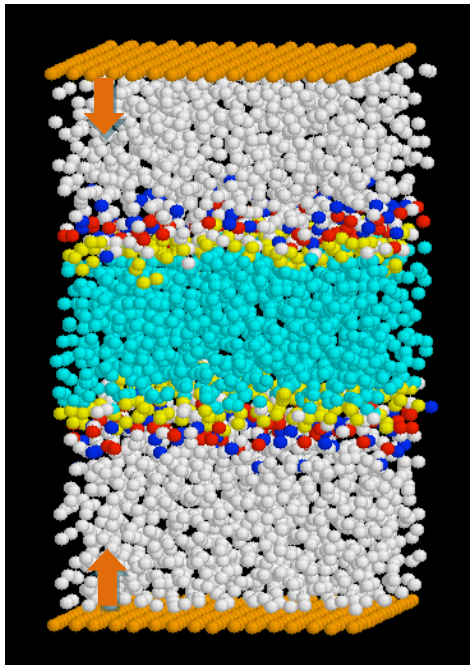

Figure 59. Schematic of the simulation system to examine the compressibility of DPPC lipid membranes under pressure. Blue dots represent the choline group, red the phosphate group, yellow the glycerol group, cyan the acyl chain tail.

7.3 Compressibility of Lipid Membrane

We designed the two walls to be impermeable, and located the lipid bilayer at the center of the simulation box (see Figure 59). When the walls move towards the center of the simulation box, water can transmit the applied external force and the lipid membrane is

compressed. The pressure on the membrane was calculated from the net force on the wall, that is, the net force exerted from water molecules on the lower side of the upper wall and on the upper side of the lower wall. This pressure should closely match the pressure on the lipid membrane since it is a connected continuous system at equilibrium or very close to it. Also to avoid water freeze during compression, 0.1 mole percent of antifreeze molecules were added according to the MARTINI force field [41].

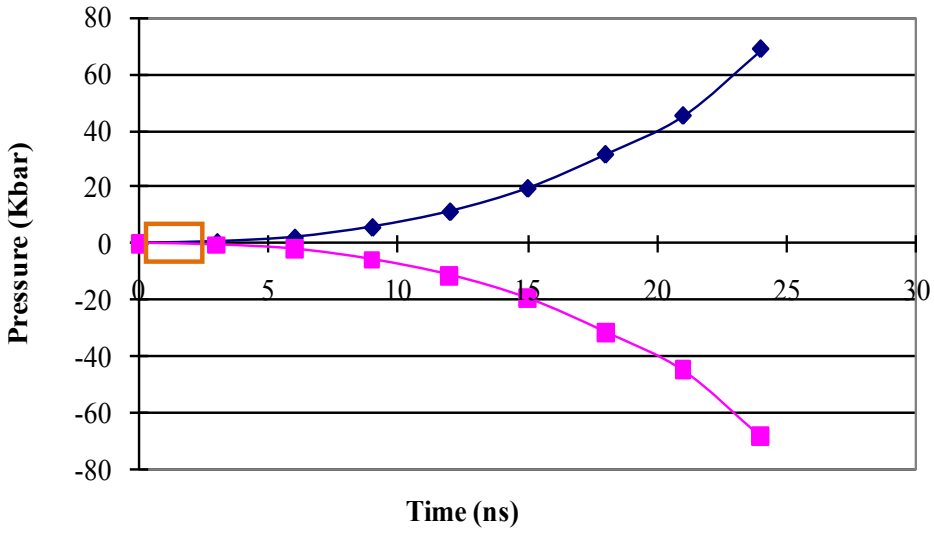

Figure 60. Pressure variations during the compression process, blue is pressure on upper wall, red is pressure on lower wall, orange box shows experiment range.

The pressure on the walls as measured during the compression is shown in Figure 60. The pressure at the beginning of compression cycles was not calculated, since initially the walls are away from the lipid-water system (but within the cut-off distance) and for low pressures the statistical scatter in the measured pressure is comparable to the actual pressure value. The orange window in Figure 60 denotes the usual experimental measurement range

and the figure clearly shows how simulations allow us to extrapolate experimental studies to much higher pressures that are not possible in experiments (can only measure pressure up to 2 Kbar). Thus our simulations can be used to determine membrane behavior at pressures not easily accessible experimentally.

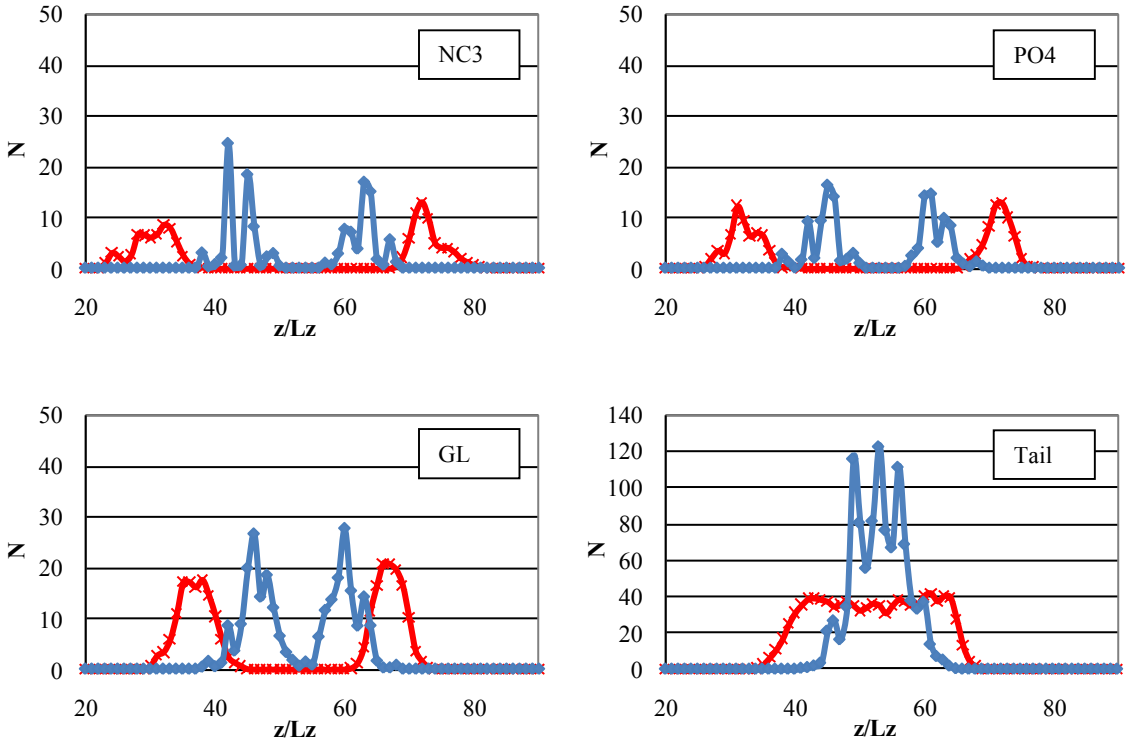

Figure 61. Lipid density profiles at the beginning and the end of compression (Red from beginning of compression, Blue from end of compression; NC3 choline group, PO4 phosphate group, GL glycerol group, Tail acyl chain group)

During the compression, changes in overall atom positions can be expressed as density profile changes. Density profile of each group of atoms of the lipid at the beginning and at the end of the compression cycle is shown in Figure 61. The density profiles in

general become more non-uniform (structured) during compression to a more solid-like state as a result of the compression of the lipid bilayer. We noticed that significant density profile changes happen at pressure range up to 10 Kbar, which suggests the lipid membrane is more compressible in this range. Also the most significant component profile change is observed for the acyl tail, which shows the largest change in the number density, and exhibits the formation of a very distinct solid-like structure. In addition from the density profile it is evident that most of the compression is resulting from the compaction of the tail section, which is not surprising considering the structure characteristics of bilayers. As will be discussed later the orientation order parameter of the tail section also confirms such behavior.

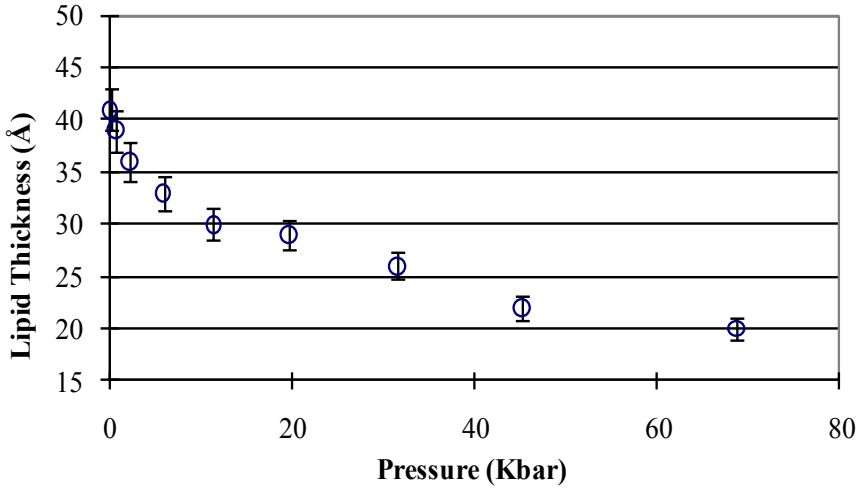

Figure 62. Changes in membrane thickness with pressure.

The thickness of the lipid membrane as a function of pressure is shown in Figure 62. The membrane thickness was obtained from the distance between the phosphate head groups of the upper and lower layers of the lipid membrane in the density profile.

The compressibility behavior of the membrane appears to be very sensitive to pressure. In the experimental pressure range (2 Kbar), high compressibility is observed. In the intermediate range (up to 10 Kbar), the compressibility is reduced but still appreciable. At high pressures (above 10 Kbar), it became almost incompressible. These observations also led Evans and Hochmuth to conclude that membranes are similar to "incompressible" fluids [169]. In our simulation, we also observed that to completely compress the lipid membrane, a large pressure (above 10 Kbar) needs to be exerted.

We also looked into the tail orientation of the lipid molecules during the compression process. The order parameters were measured during relaxation period after each compression step. Bond 1 to 3 in molecule schematic shows the connections between the four tail atoms on each tail. As shown in Figure 63, the order parameter of the lipid tail decreased during the process, which indicates that the lipid tails went from largely aligned along the normal axis to a more random arrangement. At the beginning (no compression) the lipid is at its most aligned state with order parameters in agreement with previous simulation studies. As the pressure along the normal to the bilayer increases, the free space available for the tail segments decreases and their movement becomes constrained at different orientations. At the highest compression state the tail segments start to show anti-alignment behavior and the order parameter even becomes negative, which means the tails bend towards the lipid bilayer surface because of compression.

Our results show that pressure has significant effect on the structure of lipid membranes, in addition to decreasing the thickness of lipid membrane thickness. Changes in orientation of lipid components, as a result of compression, have been found to affect the lateral diffusion rate. For example, it was found that at 2 Kbars, the lateral diffusion of a

fatty acid in a red blood cell membrane is reduced by a factor of ten [170], which would have a significant effect on cell functions such as signaling. From our simulations results, we believe that the lateral diffusion will be further suppressed at higher pressures. At a pressure of 10 Kbar, the cell signaling function could be severely impaired.

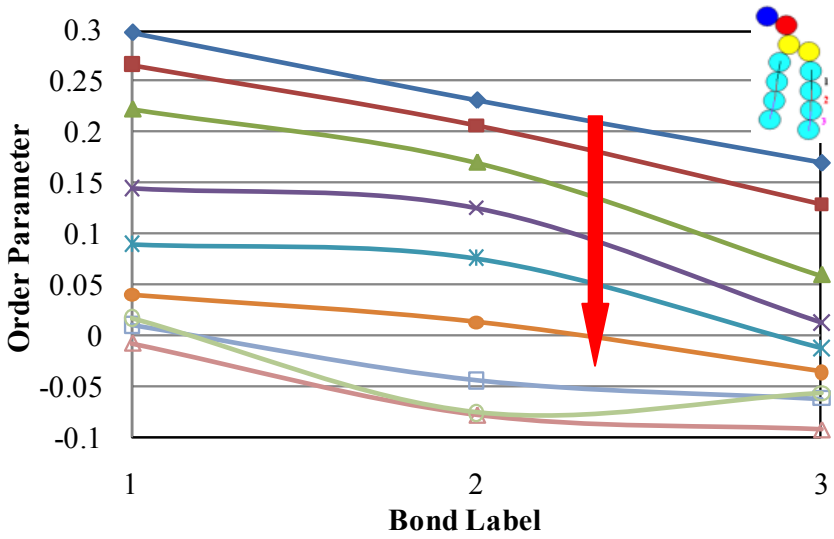

Figure 63. Lipid tail segment order parameter change during the compression, red arrow shows direction of changes along the process.

We calculated the compressibility of the lipid membrane from the pressure exerted on it and the change in thickness of the lipid membrane. The compressibility of the lipid membrane K is defined as follows:

$$K(P) = \frac{1}{V_{atm}}\left(\frac{\partial V}{\partial P}\right)_T \tag{17}$$

Here, V is the lipid volume and V_{atm} is the lipid volume at atmospheric, P is pressure. Since the membrane width is fixed in our studies, the volume of the lipid is proportional to the thickness of the lipid membrane. This leads to a more simplified definition of the compressibility in our case to

$$K(P) = \frac{1}{h_{atm}} \left(\frac{\partial h}{\partial P} \right)_T \tag{18}$$

By measuring the thickness changes during the compression, we can calculate the compressibility K using equation18 and the results are shown in Figure 64.

Figure 64 shows that we are able to calculate the compressibility for pressures up to 45 Kbar (about ten times the experimental range). The estimated values of compressibility from our simulations in the experimental pressure region (0 ~ 2 Kbar) are between -0.088 to -0.019 $Kbar^{-1}$, which agrees well with experimental measurements by Scarlata [170] who measured the compressibility of DMPC at 40˚C, and reported values in the range -0.088 to -0.057 $kbar^{-1}$ from different probe positions. Our results are also in agreement with measurements that are in the range of -0.01 to -0.06 $Kbar^{-1}$ obtained for oriented DPPC and DPPC/Cholesterol multilayers by neutron diffraction [171]. Our results also show that there is no significant change in compressibility beyond 2 Kbar. It has been previously suggested that high hydrostatic pressures may also cause the elimination of some integral membrane proteins due to increased lipid packing [171-172]. In a previous study, we have studied the gas permeation through lipid membrane embedded with OmpA channel, a common protein channel in lipid membranes. Proteins have intrinsic compressibility of ~ 0.01 $kbar^{-1}$, which is lower than the typical lipid bilayer compressibility of -0.01 to -0.06 $kbar^{-1}$ [172]. It will

therefore also be of interest to determine the effect of proteins on the compressibility of lipid membranes.

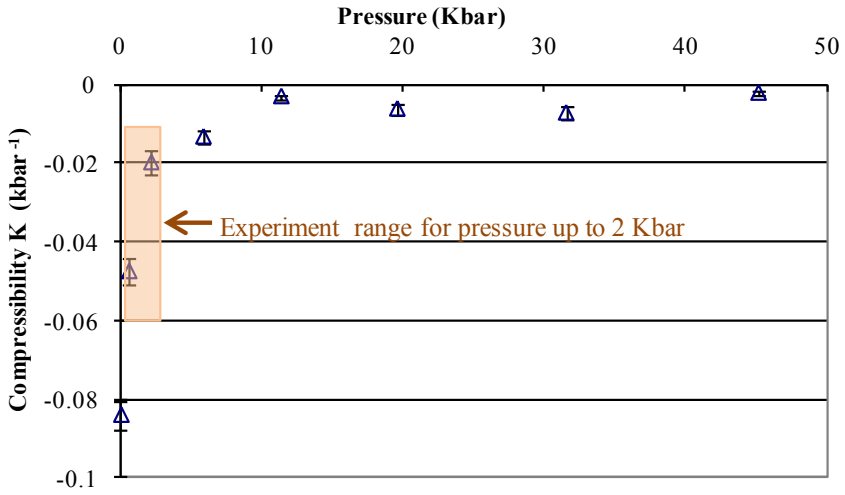

Figure 64. Compressibility as a function of pressure.

Our results indicate that MD is a particularly effective method to study compressibility because experiments under high pressures are very challenging. Although many experiments have been done to measure lipid compressibility, most of these measurements have been carried out only at pressures up to 2 Kbar because of equipment limitations [66].

8 SUMMARY AND CONCLUSIONS

How nanoparticles interact with biological membranes during their permeation process is of significant importance in determining the toxicity of nanoparticles as well as their potential applications in phototherapy, imaging and gene/drug delivery. Because of their importance in these applications, nanoparticle permeation process and nanoparticle-membrane interactions have been extensively investigated in theoretical, computational and experimental studies. In this work, molecular dynamics simulations have been employed to study of permeation of nanoparticle through a model membrane. We used gold nanoparticles as model nanoparticles and a self-assembled DPPC lipid bilayer as our model membrane. The processes of interest, such as membrane self-assembly, nanoparticle permeation and ion leakage during the nanoparticle permeations were examined over long time and length scales using CG simulations. Atomistic simulations are limited to the size and time scales. A coarse-grained approach was therefore adopted in this work.

In the first chapter, we introduced the biological background of the system of interest (membranes and nanoparticles). We elaborated on the importance of the nanoparticle permeation process and nanoparticle-membrane interactions; how computer simulations and molecular modeling can be instrumental in gaining information about them and reviewed the state of the art in this field.

A short description of the methodology used in this work followed in Chapter 2. The principles of molecular dynamics, inter- and intramolecular potential and some implementation issues employed in this work were reviewed. Some basic ideas of different force field regimes were presented. We then introduced the model used in this study.

Specifically, a short description of the MARTINI coarse-grained model, the molecular mapping and the representation of lipid molecules and lipid membrane were presented.

In Chapter 3, we focused on the simulation of self-assembly process of lipid membrane and the construction of nanoparticles. A series of simulations were then reported to validate the coarse-grained model for lipid membrane system and nanoparticles. We compared the membrane thickness, area per lipid and tail segment order parameter of lipid membrane with available experimental measurement. We also compared the ligand coverage, diffusion coefficient and radius of gyration of ligand-coated gold nanoparticles with experimental values. It was shown that the MARTINI coarse-grained model is able to reproduce the same bilayer and nanoparticles structure similar to those obtained from atomistic model and experimental measurements.

In Chapter 4, we presented a series of simulations for the translocation of nanocrystals (bare nanoparticles) across the lipid membrane using coarse-grained molecular dynamics simulations. Various sizes of nanocrystals were reported in this chapter. The velocity profile and the force profile of the nanocrystal during the translocation of the nanocrystal across the lipid bilayer were obtained, as well as the changes in local structure (boundary lipid density and water density) arising from the interaction between the nanocrystal and the lipid membrane. The minimum force and pressure for a nanocrystal to penetrate the lipid bilayer is dependent on particle size. We found that the minimum pressure for penetrating the first layer is almost independent of the size of the particles while the minimum pressure for permeating both layers is smaller for the larger size particles. We obtained detailed information on the force profile as the nanocrystal penetrates the lipid membrane, compared those results to experiments, which are unable to resolve passage

through two layers in similar details. Observation of the lipid curvature profile shows the elastic property of the lipid membrane during the penetration by a nanocrystal. The thickness of the lipid membrane shows rapid recovery to its original size. We also found that the order parameter of the tails of the bulk lipids change only slightly during the permeation of nanocrystals, while the tails of those surrounding lipids are more ordered than the remote lipids. The average length of the lipid tails is shorter for those lipids close to the nanocrystal.

In Chapter 5, we extended our studies to ligand-coated nanoparticles. We compared the permeation behavior of bare nanoparticles with ligand-coated nanoparticles and examined how the surface ligands change the details of the permeation process. We investigated uncharged ligands with various ligand lengths We found that the minimum force for penetrating the first layer is smaller while the minimum force for permeating both layers is larger, compared with bare nanoparticles. The effective size of the pore created by a ligand-coated nanoparticle in the lipid membrane remains the same as the nanoparticle moves inside the membrane and it is essentially independent of the length of ligands within our studied range. The effective pore size decreases when bare nanoparticles (having no ligands) move out of the membrane, while remaining the same for nanoparticles having surface ligands. Accordingly, the tilt angle for lipid molecules close to the nanoparticle is similar for all nanoparticles in the entry region. We observed larger lipid tilt angles in the local lipid molecules when ligand-coated nanoparticles are in the exit region, which is not observed for bare nanoparticles. The thickness of the lipid membrane and the lipid tail length recover after the permeation is completed, which points to the elastic nature of the lipid bilayer membrane. We found that the lipid tail segment of the bulk lipids changes only slightly during the permeation for all nanoparticles. In the exit region, the tails of the

surrounding lipids are more ordered during the permeation of bare nanoparticles than for nanoparticles with ligands. We also studied the structural properties of ligand-coated nanoparticles themselves. We found the size of the nanoparticles and their ligand order parameters elevate when they move into the membrane. The size of nanoparticles reaches the maximum value in the exit region, while the ligand order parameter decreases significantly in this region.

In Chapter 6, we reported our investigation of the nanoparticle permeation induced water penetration, ion transport and lipid molecule flip-flop phenomenon in a lipid membrane. The effect of ion concentration, pressure differential across the membrane, nanoparticle size and permeation velocity were examined. We found the number of water molecules in the membrane during the nanoparticle permeation increases with the nanoparticle size and with the pressure differential across the membrane, but is unaffected by the nanoparticle permeation velocity or the ion concentration gradient. Ion penetration is sensitive to the size of the nanoparticle as well as the ion concentration gradient between two sides of the membrane; no anion/cation permeation is found under small nanoparticle permeation (1.0 nm); anion selectivity is observed when the size of the nanoparticle reaches 4.0 nm. We also investigated the lipid molecule flip-flop phenomena during the nanoparticle permeation. We found the number of lipid molecule flip-flops increases with the size of the nanoparticle and the ion concentration gradient, while it decreases with the pressure differential and the nanoparticle permeation velocity. The ability of the lipid membrane to recover has been demonstrated under the various conditions we have examined in this work. There is no resulting net change in lipid composition of the two layers in the case of symmetrical bilayers. However in biological lipid membranes having mixed compositions

which are inherently asymmetrical in the two layers, there is a strong possibility of changes in composition. This may have some physiological consequences. The findings described in this work should lead to a better understanding of passive water and ion transport and lipid flip-flops during the permeation of nanoparticles and should help in developing more efficient nanocarrier drug delivery systems while avoiding cell cytotoxicity.

Finally, in Chapter 7, we investigated the mechanical properties of DPPC lipid bilayers using CG-MD simulations. This method is shown to be very effective for studying the behavior of membranes under external forces. This is confirmed by the good agreement with previous simulation and experimental studies. We have also reported results at state conditions not previously been measured in experiments such as the compressibility of lipid membrane under high pressures (up to 45 Kbar), as well as properties not previously studied experimentally.

In summary, it has been shown that the lipid membrane self-assembly process, nanoparticles construction, permeation of nanoparticles (including bare and ligand-coated nanoparticles) through lipid membranes, water penetration, ion transport and lipid molecule flip-flop phenomenon under the nanoparticle permeation as well as the mechanical properties of lipid membrane are within the copability of coarse-grained molecular dynamics simulations. Overall, this work has demonstrated that coarse-grained simulation models can be used to address biologically relevant processes. The findings in this work will lead to better understanding of mechanisms for translocation of nanoparticles across lipid membranes, may facilitate in developing efficient nanocarrier systems for intracellular delivery of therapeutics and better understanding of the mechanisms for cytotoxicity of some types of nanoparticles.

CITED LITERATURES

1. *Singer, S.J. and G.L. Nicolson, The Fluid Mosaic Model of the Structure of Cell Membranes. Science, 1972.* ***175****(4023): p. 720-731.*

2. *Balali-Mood, K., T.A. Harroun, and J.P. Bradshaw, Molecular dynamics simulations of a mixed DOPC/DOPG bilayer. European Physical Journal E, 2003.* ***12****: p. S135-S140.*

3. *Iijima, S., Helical Microtubules of Graphitic Carbon. Nature, 1991.* ***354****(6348): p. 56-58.*

4. *Popielarski, S.R., S.H. Pun, and M.E. Davis, A nanoparticle-based model delivery system to guide the rational design of gene delivery to the liver. 1. Synthesis and characterization. Bioconjugate Chemistry, 2005.* ***16****(5): p. 1063-1070.*

5. *Patil, Y.B., et al., The use of nanoparticle-mediated targeted gene silencing and drug delivery to overcome tumor drug resistance. Biomaterials, 2010.* ***31****(2): p. 358-365.*

6. *Dhoke, S.K. and A.S. Khanna, Electrochemical behavior of nano-iron oxide modified alkyd based waterborne coatings. Materials Chemistry and Physics, 2009.* ***117****(2-3): p. 550-556.*

7. *Leroueil, P.R., et al., Nanoparticle interaction with biological membranes: Does nanotechnology present a janus face? Accounts of Chemical Research, 2007.* ***40****(5): p. 335-342.*

8. *Allen, T.M. and P.R. Cullis, Drug delivery systems: Entering the mainstream. Science, 2004.* ***303****(5665): p. 1818-1822.*

9. *Fischer, R., et al., Break on through to the other side - Biophysics and cell biology shed light on cell-penetrating peptides. Chembiochem, 2005.* ***6****(12): p. 2126-2142.*

10. *Leroueil, P.R., et al., Wide varieties of cationic nanoparticles induce defects in supported lipid bilayers. Nano Letters, 2008.* ***8****(2): p. 420-424.*

11. *Maynard, A.D., et al., Safe handling of nanotechnology. Nature, 2006.* ***444****(7117): p. 267-269.*

12. *Oberdorster, G., E. Oberdorster, and J. Oberdorster, Nanotoxicology: An emerging discipline evolving from studies of ultrafine particles. Environmental Health Perspectives, 2005.* ***113****(7): p. 823-839.*

13. *Mironava, T., et al., Gold nanoparticles cellular toxicity and recovery: Effect of size, concentration and exposure time. Nanotoxicology, 2010.* ***4****(1): p. 120-137.*

14. *Herbig, M.E., et al., The cell penetrating peptides pVEC and W2-pVEC induce*

transformation of gel phase domains in phospholipid bilayers without affecting their integrity. Biochemistry, 2006. ***45****(11): p. 3598-3609.*

15. *Takeuchi, T., et al., Direct and rapid cytosolic delivery using cell-penetrating peptides mediated by pyrenebutyrate. Acs Chemical Biology, 2006.* ***1****(5): p. 299-303.*

16. *Thoren, P.E.G., et al., Uptake of analogs of penetratin, Tat(48-60) and oligoarginine in live cells. Biochemical and Biophysical Research Communications, 2003.* ***307****(1): p. 100-107.*

17. *Hong, S.P., et al., Interaction of polycationic polymers with supported lipid bilayers and cells: Nanoscale hole formation and enhanced membrane permeability. Bioconjugate Chemistry, 2006.* ***17****(3): p. 728-734.*

18. *El-Sayed, I.H., X.H. Huang, and M.A. El-Sayed, Surface plasmon resonance scattering and absorption of anti-EGFR antibody conjugated gold nanoparticles in cancer diagnostics: Applications in oral cancer. Nano Letters, 2005.* ***5****(5): p. 829-834.*

19. *Zhang, Z.Y. and B.D. Smith, High-generation polycationic dendrimers are unusually effective at disrupting anionic vesicles: Membrane bending model. Bioconjugate Chemistry, 2000.* ***11****(6): p. 805-814.*

20. *Hong, S.P., et al., Interaction of poly(amidoamine) dendrimers with supported lipid bilayers and cells: Hole formation and the relation to transport. Bioconjugate Chemistry, 2004.* ***15****(4): p. 774-782.*

21. *Monteiro-Riviere, N.A., et al., Multi-walled carbon nanotube interactions with human epidermal keratinocytes. Toxicology Letters, 2005.* ***155****(3): p. 377-384.*

22. *Oberdorster, E., Manufactured nanomaterials (Fullerenes, C-60) induce oxidative stress in the brain of juvenile largemouth bass. Environmental Health Perspectives, 2004.* ***112****(10): p. 1058-1062.*

23. *Oberdorster, G., et al., Association of particulate air-pollition and acute mortality-involvement of ultrafine particles. Inhalation Toxicology, 1995. 7(1): p. 111-124.*

24. *Ginzburg, V.V. and S. Balijepailli, Modeling the thermodynamics of the interaction of nanoparticles with cell membranes. Nano Letters, 2007. 7(12): p. 3716-3722.*

25. *Qiao, R., et al., Translocation of C-60 and its derivatives across a lipid bilayer. Nano Letters, 2007. 7(3): p. 614-619.*

26. *Smith, G.D. and D. Bedrov, Transport of C-60 fullerenes through a lipid membrane: A molecular dynamics simulation study. Biophysical Journal, 2007: p. 65A-66A.*

27. *Bedrov, D., et al., Passive transport of C-60 fullerenes through a lipid membrane: A molecular dynamics simulation study. Journal of Physical Chemistry B, 2008.*

112*(7): p. 2078-2084.*

28. *Shi, X.H., Y. Kong, and H.J. Gao, Coarse grained molecular dynamics and theoretical studies of carbon nanotubes entering cell membrane. Acta Mechanica Sinica, 2008.* ***24****(2): p. 161-169.*

29. *Wallace, E.J. and M.S.P. Sansom, Blocking of carbon nanotube based nanoinjectors by lipids: A simulation study. Nano Letters, 2008.* ***8****(9): p. 2751-2756.*

30. *Li, Y., X. Chen, and N. Gu, Computational Investigation of Interaction between Nanoparticles and Membranes: Hydrophobic/Hydrophilic Effect. Journal of Physical Chemistry B, 2008.* ***112****(51): p. 16647-16653.*

31. *Li, Y. and N. Gu, Thermodynamics of Charged Nanoparticle Adsorption on Charge-Neutral Membranes: A Simulation Study. Journal of Physical Chemistry B, 2010.* ***114****(8): p. 2749-2754.*

32. *Ramalho, J.P.P.R.J.P.P., P. Gkeka, and L. Sarkisov, Structure and Phase Transformations of DPPC Lipid Bilayers in the Presence of Nanoparticles: Insights from Coarse-Grained Molecular Dynamics Simulations. Langmuir, 2011.* ***27****(7): p. 3723-3730.*

33. *Lin, J., et al., Penetration of Lipid Membranes by Gold Nanoparticles: Insights into Cellular Uptake, Cytotoxicity, and Their Relationship. ACS Nano.* ***4****(9): p. 5421-5429.*

34. *Lin, X.B., Y. Li, and N. Gu, Molecular dynamics simulations of the interactions of charge-neutral PAMAM dendrimers with pulmonary surfactant. Soft Matter, 2011.* ***7****(8): p. 3882-3888.*

35. *Yang, K. and Y.Q. Ma, Computer simulation of the translocation of nanoparticles with different shapes across a lipid bilayer. Nature Nanotechnology.* ***5****(8): p. 579-583.*

36. *Brooks, B.R., et al., CHARMM - A program for macromolecular energy, minimization, and dynamics calculations. Journal of Computational Chemistry, 1983.* ***4****(2): p. 187-217.*

37. *Jorgensen, W.L., D.S. Maxwell, and J. TiradoRives, Development and testing of the OPLS all-atom force field on conformational energetics and properties of organic liquids. Journal of the American Chemical Society, 1996.* ***118****(45): p. 11225-11236.*

38. *Tsige, M., et al., Molecular dynamics simulations and integral equation theory of alkane chains: Comparison of explicit and united atom models. Macromolecules, 2003.* ***36****(6): p. 2158-2164.*

39. *Reith, D., M. Putz, and F. Muller-Plathe, Deriving effective mesoscale potentials from atomistic simulations. Journal of Computational Chemistry, 2003.* ***24****(13): p.*

1624-1636.

40. Marrink, S.J., A.H. de Vries, and A.E. Mark, Coarse grained model for semiquantitative lipid simulations. Journal of Physical Chemistry B, 2004. ***108****(2): p. 750-760.*

41. Marrink, S.J., et al., The MARTINI force field: Coarse grained model for biomolecular simulations. Journal of Physical Chemistry B, 2007. ***111****(27): p. 7812-7824.*

42. Monticelli, L., et al., The MARTINI coarse-grained force field: Extension to proteins. Journal of Chemical Theory and Computation, 2008. ***4****(5): p. 819-834.*

43. Marrink, S.J. and H.J.C. Berendsen, Simulation of water transport through a lipid membrane. Journal of Physical Chemistry, 1994. ***98****(15): p. 4155-4168.*

44. Tieleman, D.P., S.J. Marrink, and H.J.C. Berendsen, A computer perspective of membranes: molecular dynamics studies of lipid bilayer systems. Biochimica Et Biophysica Acta-Reviews on Biomembranes, 1997. ***1331****(3): p. 235-270.*

45. Lindahl, E. and O. Edholm, Mesoscopic undulations and thickness fluctuations in lipid bilayers from molecular dynamics simulations. Biophysical Journal, 2000. ***79****(1): p. 426-433.*

46. Patra, M., et al., Molecular dynamics simulations of lipid bilayers: Major artifacts due to truncating electrostatic interactions. Biophysical Journal, 2003. ***84****(6): p. 3636-3645.*

47. Sum, A.K., R. Faller, and J.J. de Pablo, Molecular simulation study of phospholipid bilayers and insights of the interactions with disaccharides. Biophysical Journal, 2003. ***85****(5): p. 2830-2844.*

48. Goetz, R. and R. Lipowsky, Computer simulations of bilayer membranes: Self-assembly and interfacial tension. Journal of Chemical Physics, 1998. ***108****(17): p. 7397-7409.*

49. Shelley, J.C., et al., A coarse grain model for phospholipid simulations. Journal of Physical Chemistry B, 2001. ***105****(19): p. 4464-4470.*

50. Kranenburg, M., M. Venturoli, and B. Smit, Phase behavior and induced interdigitation in bilayers studied with dissipative particle dynamics. Journal of Physical Chemistry B, 2003. ***107****(41): p. 11491-11501.*

51. Daniel, M.C. and D. Astruc, Gold nanoparticles: Assembly, supramolecular chemistry, quantum-size-related properties, and applications toward biology, catalysis, and nanotechnology. Chemical Reviews, 2004. ***104****(1): p. 293-346.*

52. Neouze, M.-A. and U. Schubert, Surface modification and functionalization of metal

and metal oxide nanoparticles by organic ligands. Monatshefte Fur Chemie, 2008. ***139****(3): p. 183-195.*

53. *Sperling, R.A., et al., Biological applications of gold nanoparticles. Chemical Society Reviews, 2008.* ***37****(9): p. 1896-1908.*

54. *Zhang, S., G. Leem, and T.R. Lee, Monolayer-Protected Gold Nanoparticles Prepared Using Long-Chain Alkanethioacetates. Langmuir, 2009.* ***25****(24): p. 13855-13860.*

55. *Weare, W.W., et al., Improved synthesis of small (d(CORE) approximate to 1.5 nm) phosphine-stabilized gold nanoparticles. Journal of the American Chemical Society, 2000.* ***122****(51): p. 12890-12891.*

56. *Peterle, T., et al., Multidentate thioether ligands coating gold nanoparticles. Chemical Communications, 2008(29): p. 3438-3440.*

57. *Thomas, K.G., J. Zajicek, and P.V. Kamat, Surface binding properties of tetraoctylammonium bromide-capped gold nanoparticles. Langmuir, 2002.* ***18****(9): p. 3722-3727.*

58. *Sethi, M., D.B. Pacardo, and M.R. Knecht, Biological Surface Effects of Metallic Nanomaterials for Applications in Assembly and Catalysis. Langmuir, 2010.* ***26****(19): p. 15121-15134.*

59. *Angelova, P., et al., Fluorescent monolayer protected gold nanoparticles - Preparation and structure elucidation. Journal of Molecular Structure, 2011.* ***993****(1-3): p. 185-192.*

60. *Feigl, C., et al., A theoretical study of size and temperature dependent morphology transformations in gold nanoparticles. Chemical Physics Letters, 2009.* ***474****(1-3): p. 115-118.*

61. *Ghorai, P.K. and S.C. Glotzer, Molecular dynamics simulation study of self-assembled monolayers of alkanethiol surfactants on spherical gold nanoparticles. Journal of Physical Chemistry C, 2007.* ***111****(43): p. 15857-15862.*

62. *Yang, A.-C. and C.-I. Weng, Structural and Dynamic Properties of Water near Monolayer-Protected Gold Clusters with Various Alkanethiol Tail Groups. The Journal of Physical Chemistry C, 2010.* ***114****(19): p. 8697-8709.*

63. *Duchesne, L., et al., Supramolecular domains in mixed peptide self-assembled monolayers on gold nanoparticles. Chembiochem, 2008.* ***9****(13): p. 2127-2134.*

64. *Lee, O.S., T.R. Prytkova, and G.C. Schatz, Using DNA to Link Gold Nanoparticles, Polymers, and Molecules: A Theoretical Perspective. Journal of Physical Chemistry Letters, 2010.* ***1****(12): p. 1781-1788.*

65. *Yuan, H.J., C.J. Jameson, and S. Murad, Diffusion of gases across lipid membranes with OmpA channel: a molecular dynamics study. Molecular Physics.* ***108****(12): p. 1569-1581.*

66. *Nagle, J.F. and S. Tristram-Nagle, Structure of lipid bilayers. Biochimica Et Biophysica Acta-Reviews on Biomembranes, 2000.* ***1469****(3): p. 159-195.*

67. *Nagle, J.F., et al., X-ray structure determination of fully hydrated L(alpha) phase dipalmitoylphosphatidylcholine bilayers. Biophysical Journal, 1996.* ***70****(3): p. 1419-1431.*

68. *Douliez, J.P., A. Leonard, and E.J. Dufourc, Restatement of order parameters in biomemebranes - calculation of C-C bond order paramters from C-D quadrupolar splittings. Biophysical Journal, 1995.* ***68****(5): p. 1727-1739.*

69. *Whetten, R.L., et al., Nanocrystal gold molecules. Advanced Materials, 1996.* ***8****(5): p. 428-&.*

70. *Erkoc, S., Stability of gold clusters: molecular-dynamics simulations. Physica E, 2000.* ***8****(3): p. 210-218.*

71. *Nayebi, P. and E. Zaminpayma, Crystallization of Liquid Gold Nanoparticles by Molecular Dynamics Simulation. Journal of Cluster Science, 2009.* ***20****(4): p. 661-670.*

72. *Cleveland, C.L., et al., Structural evolution of smaller gold nanocrystals: The truncated decahedral motif. Physical Review Letters, 1997.* ***79****(10): p. 1873-1876.*

73. *Lee, O.S. and G.C. Schatz, Interaction between DNAs on a Gold Surface. Journal of Physical Chemistry C, 2009.* ***113****(36): p. 15941-15947.*

74. *Chang, C.I., et al., Adsorption mechanism of water molecules surrounding Au nanoparticles of different sizes. Journal of Chemical Physics, 2008.* ***128****(15): p. 9.*

75. *Hofler, L. and R.E. Gyurcsanyi, Coarse grained molecular dynamics simulation of electromechanically-gated DNA modified conical nanopores. Electroanalysis, 2008.* ***20****(3): p. 301-307.*

76. *Lin, X.B., Y. Li, and N. Gu, Nanoparticle's Size Effect on Its Translocation Across a Lipid Bilayer: A Molecular Dynamics Simulation. Journal of Computational and Theoretical Nanoscience.* ***7****(1): p. 269-276.*

77. *Maitland G.C, R.M., Brian Smith E., Wakeham W.A., ed. Intermolecular forces. Their Origin and determination 1987, Oxford University Press.*

78. *Shi, Q., S. Izvekov, and G.A. Voth, Mixed atomistic and coarse-grained molecular dynamics: Simulation of a membrane-bound ion channel. Journal of Physical Chemistry B, 2006.* ***110****(31): p. 15045-15048.*

79. *Wu, Z.B., et al., Hybrid atomistic-coarse-grained treatment of thin-film lubrication. I. Journal of Chemical Physics, 2004.* ***120****(14): p. 6744-6750.*

80. *Wu, Z.B., D.J. Diestler, and X.C. Zeng, Hybrid atomistic-coarse-grained treatment of thin-film lubrication. II. Journal of Chemical Physics, 2004.* ***121****(16): p. 8029-8038.*

81. *Luedtke, W.D. and U. Landman, Structure and thermodynamics of self-assembled monolayers on gold nanocrystallites. Journal of Physical Chemistry B, 1998.* ***102****(34): p. 6566-6572.*

82. *Hostetler, M.J., et al., Alkanethiolate gold cluster molecules with core diameters from 1.5 to 5.2 nm: Core and monolayer properties as a function of core size. Langmuir, 1998.* ***14****(1): p. 17-30.*

83. *Tiwari, P., et al., Functionalized Gold Nanoparticles and Their Biomedical Applications. Nanomaterials, 2011.* ***1****(1): p. 31-63.*

84. *Cho, W.-S., et al., Size-dependent tissue kinetics of PEG-coated gold nanoparticles. Toxicology and Applied Pharmacology, 2010.* ***245****(1): p. 116-123.*

85. *Pan, Y., et al., Size-dependent cytotoxicity of gold nanoparticles. Small, 2007.* ***3****(11): p. 1941-1949.*

86. *Hainfeld, J.F., D.N. Slatkin, and H.M. Smilowitz, The use of gold nanoparticles to enhance radiotherapy in mice. Physics in Medicine and Biology, 2004.* ***49****(18): p. N309-N315.*

87. *Chithrani, B.D., A.A. Ghazani, and W.C.W. Chan, Determining the size and shape dependence of gold nanoparticle uptake into mammalian cells. Nano Letters, 2006.* ***6****(4): p. 662-668.*

88. *Jiang, W., et al., Nanoparticle-mediated cellular response is size-dependent. Nature Nanotechnology, 2008.* ***3****(3): p. 145-150.*

89. *Wang, S.-H., et al., Size-dependent endocytosis of gold nanoparticles studied by three-dimensional mapping of plasmonic scattering images. Journal of Nanobiotechnology, 2010.* ***8****.*

90. *Bonting, S.L. and J.J.H.H.M. De Pont, eds. Membrane Transport. 1981.*

91. *Nel, A., et al., Toxic potential of materials at the nanolevel. Science, 2006.* ***311****(5761): p. 622-627.*

92. *Goodman, C.M., et al., Toxicity of gold nanoparticles functionalized with cationic and anionic side chains. Bioconjugate Chemistry, 2004.* ***15****(4): p. 897-900.*

93. *Sayes, C.M., et al., Functionalization density dependence of single-walled carbon*

nanotubes cytotoxicity in vitro. Toxicology Letters, 2006. ***161****(2): p. 135-142.*

94. *Roiter, Y., et al., Interaction of nanoparticles with lipid membrane. Nano Letters, 2008.* ***8****(3): p. 941-944.*

95. *Peetla, C. and V. Labhasetwar, Effect of Molecular Structure of Cationic Surfactants on Biophysical Interactions of Surfactant-Modified Nanoparticles with a Model Membrane and Cellular Uptake. Langmuir, 2009.* ***25****(4): p. 2369-2377.*

96. *Chen, J.M., et al., Cationic Nanoparticles Induce Nanoscale Disruption in Living Cell Plasma Membranes. Journal of Physical Chemistry B, 2009.* ***113****(32): p. 11179-11185.*

97. *Fiedler, S.L. and A. Violi, Simulation of Nanoparticle Permeation through a Lipid Membrane. Biophysical Journal.* ***99****(1): p. 144-152.*

98. *Wong-Ekkabut, J., et al., Computer simulation study of fullerene translocation through lipid membranes. Nature Nanotechnology, 2008.* ***3****(6): p. 363-368.*

99. *Lee, H. and R.G. Larson, Lipid bilayer curvature and pore formation induced by charged linear polymers and dendrimers: The effect of molecular shape. Journal of Physical Chemistry B, 2008.* ***112****(39): p. 12279-12285.*

100. *Moore, M.N., Do nanoparticles present ecotoxicological risks for the health of the aquatic environment? Environment International, 2006.* ***32****(8): p. 967-976.*

101. *Navarro, E., et al., Environmental behavior and ecotoxicity of engineered nanoparticles to algae, plants, and fungi. Ecotoxicology, 2008.* ***17****(5): p. 372-386.*

102. *Bilensoy, E., et al., Development of nonsurfactant cyclodextrin nanoparticles loaded with anticancer drug paclitaxel. Journal of Pharmaceutical Sciences, 2008.* ***97****(4): p. 1519-1529.*

103. *Tedesco, S., et al., Oxidative stress and toxicity of gold nanoparticles in Mytilus edulis. Aquatic Toxicology.* ***100****(2): p. 178-186.*

104. *Yuan, H.J., C.J. Jameson, and S. Murad, Exploring gas permeability of lipid membranes using coarse-grained molecular dynamics. Molecular Simulation, 2009.* ***35****(10-11): p. 953-961.*

105. *Chen, X., et al., A cell nanoinjector based on carbon nanotubes. Proceedings of the National Academy of Sciences of the United States of America, 2007.* ***104****(20): p. 8218-8222.*

106. *Obataya, I., et al., Nanoscale operation of a living cell using an atomic force microscope with a nanoneedle. Nano Letters, 2005.* ***5****(1): p. 27-30.*

107. *Vakarelski, I.U., et al., Penetration of living cell membranes with fortified carbon*

nanotube tips. Langmuir, 2007. ***23****(22): p. 10893-10896.*

108. Yin, H., H.P. Too, and G.M. Chow, The effects of particle size and surface coating on the cytotoxicity of nickel ferrite. Biomaterials, 2005. ***26****(29): p. 5818-5826.*

109. Nair, S., et al., Role of size scale of ZnO nanoparticles and microparticles on toxicity toward bacteria and osteoblast cancer cells. Journal of Materials Science-Materials in Medicine, 2009. ***20****: p. 235-241.*

110. Vasir, J.K. and V. Labhasetwar, Quantification of the force of nanoparticle-cell membrane interactions and its influence on intracellular trafficking of nanoparticles. Biomaterials, 2008. ***29****(31): p. 4244-4252.*

111. Cherukuri, P., et al., Near-infrared fluorescence microscopy of single-walled carbon nanotubes in phagocytic cells. Journal of the American Chemical Society, 2004. ***126****(48): p. 15638-15639.*

112. Verma, A. and F. Stellacci, Effect of Surface Properties on Nanoparticle-Cell Interactions. Small, 2010. ***6****(1): p. 12-21.*

113. Plimpton, S., Fast parallel algorithms for short-range molecular dynamics. Journal of Computational Physics, 1995. ***117****(1): p. 1-19.*

114. Schneider, T. and E. Stoll, Molecular-dynamics study of a 3-dimensional one-component model for distortive phase-transitions. Physical Review B, 1978. ***17****(3): p. 1302-1322.*

115. Marrink, S.J. and H.J.C. Berendsen, Permeation process of small molecules across lipid membranes studied by molecular dynamics simulations. Journal of Physical Chemistry, 1996. ***100****(41): p. 16729-16738.*

116. Van der Spoel, D., et al., GROMACS: Fast, flexible, and free. Journal of Computational Chemistry, 2005. ***26****(16): p. 1701-1718.*

117. Baron, R., et al., Configurational entropies of lipids in pure and mixed bilayers from atomic-level and coarse-grained molecular dynamics simulations. Journal of Physical Chemistry B, 2006. ***110****(31): p. 15602-15614.*

118. Baron, R., et al., Comparison of thermodynamic properties of coarse-grained and atomic-level simulation models. Chemphyschem, 2007. ***8****(3): p. 452-461.*

119. Mecke, A., et al., Lipid bilayer disruption by polycationic polymers: The roles of size and chemical functional group. Langmuir, 2005. ***21****(23): p. 10348-10354.*

120. Mecke, A., et al., Direct observation of lipid bilayer disruption by poly(amidoamine) dendrimers. Chemistry and Physics of Lipids, 2004. ***132****(1): p. 3-14.*

121. Kruis, F.E., H. Fissan, and A. Peled, Synthesis of nanoparticles in the gas phase for

electronic, optical and magnetic applications - A review. Journal of Aerosol Science, 1998. ***29****(5-6): p. 511-535.*

122. *Shan, J. and H. Tenhu, Recent advances in polymer protected gold nanoparticles: synthesis, properties and applications. Chemical Communications, 2007(44): p. 4580-4598.*

123. *Boisselier, E. and D. Astruc, Gold nanoparticles in nanomedicine: preparations, imaging, diagnostics, therapies and toxicity. Chemical Society Reviews, 2009.* ***38****(6): p. 1759-1782.*

124. *He, C., et al., Effects of particle size and surface charge on cellular uptake and biodistribution of polymeric nanoparticles. Biomaterials, 2010.* ***31****(13): p. 3657-3666.*

125. *Verma, A., et al., Surface-structure-regulated cell-membrane penetration by monolayer-protected nanoparticles. Nat Mater, 2008. 7(7): p. 588-595.*

126. *Verma, P. and N.A. Melosh, Gigaohm resistance membrane seals with stealth probe electrodes. Applied Physics Letters, 2010.* ***97****(3).*

127. *Min, Y., et al., The role of interparticle and external forces in nanoparticle assembly. Nat Mater, 2008. 7(7): p. 527-538.*

128. *Be'er, A., et al., Quantitative experimental studies of spontaneous rotations of bismuth nanoparticles. Physical Review B, 2006.* ***74****(22): p. 224111.*

129. *Mitra, A., et al., Nano-optofluidic Detection of Single Viruses and Nanoparticles. ACS Nano, 2010.* ***4****(3): p. 1305-1312.*

130. *Deamer, D.W. and J. Bramhall, Permeability of lipid bilayers to water and ionic solutes. Chemistry and Physics of Lipids, 1986.* ***40****(2-4): p. 167-188.*

131. *Toyoshima, Y. and T.E. Thompson, Chloride flux in bilayer membranes - chloride permeability in aqueous dispersions of single-walled bilayer vesicles. Biochemistry, 1975.* ***14****(7): p. 1525-1531.*

132. *Tepper, H.L. and G.A. Voth, Mechanisms of passive ion permeation through lipid bilayers: Insights from simulations. Journal of Physical Chemistry B, 2006.* ***110****(42): p. 21327-21337.*

133. *Gurtovenko, A.A., J. Anwar, and I. Vattulainen, Defect-Mediated Trafficking across Cell Membranes: Insights from in Silico Modeling. Chemical Reviews, 2010.* ***110****(10): p. 6077-6103.*

134. *Leontiadou, H., A.E. Mark, and S.-J. Marrink, Ion transport across transmembrane pores. Biophysical Journal, 2007.* ***92****(12): p. 4209-4215.*

135. *Kandasamy, S.K. and R.G. Larson, Cation and anion transport through hydrophilic pores in lipid bilayers. Journal of Chemical Physics, 2006.* ***125****(7).*

136. *Gurtovenko, A.A. and I. Vattulainen, Ion leakage through transient water pores in protein-free lipid membranes driven by transmembrane ionic charge imbalance. Biophysical Journal, 2007.* ***92****(6): p. 1878-1890.*

137. *Lawaczeck, R., Deffect structures in membranes- routes for the permeation of small molecules. Berichte Der Bunsen-Gesellschaft-Physical Chemistry Chemical Physics, 1988.* ***92****(9): p. 961-963.*

138. *Jansen, M. and A. Blume, A comparative study of diffusive and osmotic water permeation across bilayers composed of phospholipids with different head groups and fatty acyl chains. Biophysical Journal, 1995.* ***68****(3): p. 997-1008.*

139. *Hamilton, R.T. and E.W. Kaler, ALKALI-METAL ION-TRANSPORT THROUGH THIN BILAYERS. Journal of Physical Chemistry, 1990.* ***94****(6): p. 2560-2566.*

140. *Song, B., et al., Permeation of nanocrystals across lipid membranes. Molecular Physics, 2011.* ***109****(11): p. 1511-1526.*

141. *Song, B., et al., Role of surface ligands in nanoparticle permeation through a model membrane: a coarse-grained molecular dynamics simulations study. Molecular Physics, 2012.* ***in press****.*

142. *Lin, J., et al., Penetration of Lipid Membranes by Gold Nanoparticles: Insights into Cellular Uptake, Cytotoxicity, and Their Relationship. ACS Nano, 2010.* ***4****(9): p. 5421-5429.*

143. *Fiedler, S.L. and A. Violi, Simulation of Nanoparticle Permeation through a Lipid Membrane. Biophysical Journal, 2010.* ***99****(1): p. 144-152.*

144. *Prates Ramalho, J.P., P. Gkeka, and L. Sarkisov, Structure and phase transformations of DPPC lipid bilayers in the presence of nanoparticles: insights from coarse-grained molecular dynamics simulations. Langmuir : the ACS journal of surfaces and colloids, 2011.* ***27****(7): p. 3723-30.*

145. *Van Lehn, R.C. and A. Alexander-Katz, Penetration of lipid bilayers by nanoparticles with environmentally-responsive surfaces: simulations and theory. Soft Matter, 2011. 7(24): p. 11392-11404.*

146. *Li, Y. and N. Gu, Computer Simulation of the Inclusion of Hydrophobic Nanoparticles into a Lipid Bilayer. Journal of Nanoscience and Nanotechnology, 2010.* ***10****(11): p. 7616-7619.*

147. *Gurtovenko, A.A. and I. Vattulainen, Molecular mechanism for lipid flip-flops. Journal of Physical Chemistry B, 2007.* ***111****(48): p. 13554-13559.*

148. *Bennett, W.F.D. and D.P. Tieleman, Water Defect and Pore Formation in Atomistic and Coarse-Grained Lipid Membranes: Pushing the Limits of Coarse Graining. Journal of Chemical Theory and Computation, 2011.* ***7****(9): p. 2981-2988.*

149. *Liu, J. and J.C. Conboy, 1,2-diacyl-phosphatidylcholine flip-flop measured directly by sum-frequency vibrational spectroscopy. Biophysical Journal, 2005.* ***89****(4): p. 2522-2532.*

150. *Anglin, T.C., et al., Free Energy and Entropy of Activation for Phospholipid Flip-Flop in Planar Supported Lipid Bilayers. Journal of Physical Chemistry B, 2010.* ***114****(5): p. 1903-1914.*

151. *Raggers, R.J., et al., Lipid traffic: The ABC of transbilayer movement. Traffic, 2000.* ***1****(3): p. 226-234.*

152. *Schwarz, S., C.W.M. Haest, and B. Deuticke, Extensive electroporation abolishes experimentally induced shape transformations of erythrocytes: a consequence of phospholipid symmetrization. Biochimica Et Biophysica Acta-Biomembranes, 1999.* ***1421****(2): p. 361-379.*

153. *Liu, H.M., S. Murad, and C.J. Jameson, Ion permeation dynamics in carbon nanotubes. Journal of Chemical Physics, 2006.* ***125****(8).*

154. *Chanturiya, A., et al., New cationic lipids form channel-like pores in phospholipid bilayers. Biophysical Journal, 2003.* ***84****(3): p. 1750-1755.*

155. *Manno, S., Y. Takakuwa, and N. Mohandas, Identification of a functional role for lipid asymmetry in biological membranes: Phosphatidylserine-skeletal protein interactions modulate membrane stability. Proceedings of the National Academy of Sciences of the United States of America, 2002.* ***99****(4): p. 1943-1948.*

156. *Pomorski, T., et al., Lipid distribution and transport across cellular membranes. Seminars in Cell & Developmental Biology, 2001.* ***12****(2): p. 139-148.*

157. *Balasubramanian, K. and A.J. Schroit, Aminophospholipid asymmetry: A matter of life and death. Annual Review of Physiology, 2003.* ***65****: p. 701-734.*

158. *de Vries, A.H., A.E. Mark, and S.J. Marrink, Molecular dynamics simulation of the spontaneous formation of a small DPPC vesicle in water in atomistic detail. Journal of the American Chemical Society, 2004.* ***126****(14): p. 4488-4489.*

159. *Dickey, A.N. and R. Faller, How alcohol chain-length and concentration modulate hydrogen bond formation in a lipid bilayer. Biophysical Journal, 2007.* ***92****(7): p. 2366-2376.*

160. *Leontiadou, H., A.E. Mark, and S.J. Marrink, Antimicrobial peptides in action. Journal of the American Chemical Society, 2006.* ***128****(37): p. 12156-12161.*

161. *Tieleman, D.P. and S.-J. Marrink, Lipids out of equilibrium: Energetics of desorption and pore mediated flip-flop. Journal of the American Chemical Society, 2006.* ***128****(38): p. 12462-12467.*

162. *Chernomordik, L.V. and M.M. Kozlov, Protein-Lipid Interplay in Fusion and Fission of Biological Membranes. Annual Review of Biochemistry, 2003.* ***72****(1): p. 175-207.*

163. *Arsianti, M., et al., Polyethylenimine Based Magnetic Iron-Oxide Vector: The Effect of Vector Component Assembly on Cellular Entry Mechanism, Intracellular Localization, and Cellular Viability. Biomacromolecules, 2010.* ***11****(9): p. 2521-2531.*

164. *Kadiu, I. and H. Gendelman, Human Immunodeficiency Virus type 1 Endocytic Trafficking Through Macrophage Bridging Conduits Facilitates Spread of Infection. Journal of Neuroimmune Pharmacology, 2011.* ***6****(4): p. 658-675.*

165. *Ramanan, V., et al., Systems biology and physical biology of clathrin-mediated endocytosis. Integrative Biology, 2011.* ***3****(8): p. 803-815.*

166. *Szleifer, I., et al., Molecular theory of curvature elasticity in serfactant films. Journal of Chemical Physics, 1990.* ***92****(11): p. 6800-6817.*

167. *Nebel, S., P. Ganz, and J. Seelig, Heat Changes in Lipid Membranes under Sudden Osmotic Stress†. Biochemistry, 1997.* ***36****(10): p. 2853-2859.*

168. *Crowley, J.M., Electrical Breakdown of Bimolecular Lipid Membranes as an Electromechanical Instability. Biophysical Journal, 1973.* ***13****(7): p. 711-724.*

169. *Evans, E.A. and R.M. Hochmuth, Mechanochemical Properties of Membranes, in Current Topics in Membranes and Transport, B. Felix and K. Arnost, Editors. 1978, Academic Press. p. 1-64.*

170. *Scarlata, S.F., Compression of lipid membranes as observed at varying membrane positions. Biophysical Journal, 1991.* ***60****(2): p. 334-340.*

171. *Wong, P.T.T. and H.H. Mantsch, Reorientational and Conformational Ordering Processes at Elevated Pressures in 1,2-Dioleoyl Phosphatidylcholine: A Raman and Infrared Spectroscopic Study. Biophysical Journal, 1988.* ***54****(5): p. 781-790.*

172. *Braganza, L.F. and D.L. Worcester, Structural changes in lipid bilayers and biological membranes caused by hydrostatic pressure. Biochemistry, 1986.* ***25****(23): p. 7484-7488.*

VITA

NAME: Bo Song

EDUCATION:

Ph.D., Chemical Engineering, University of Illinois at Chicago, Chicago, USA, 2012
M.S., Statistics, University of Illinois at Chicago, Chicago, USA, 2012
M.S., Chemical Engineering, Xiamen University, Xiamen, China, 2008
B.S., Chemical Engineering and Technology, Xiamen University, Xiamen, China, 2005

PUBLICATIONS:

Journal:

1. H. Yuan, S. V. Pham, **B. Song**, C. J. Jameson, S. Murad, *Compressibility study of biological membrane using coarse-grained molecular dynamics simulation*, in preparation.
2. **B. Song**, H. Yuan, S. V. Pham, J. Jameson, S. Murad, *Nanoparticle permeation induces water penetration, ion transport and lipid flip-flop*, ***Langmuir***, revision submitted.
3. **B. Song**, H. Yuan, C. J. Jameson, S. Murad, *Role of surface ligands in nanoparticle permeation through a model membrane: a coarse-grained molecular dynamics simulations study*, ***Molecular Physics***, 2012, 110(18): 2181-2195.
4. **B. Song**, H. Yuan, C. J. Jameson, S. Murad, *Permeation of Nanocrystals across Lipid Membranes*, ***Molecular Physics***, 2011,109(11): 1511-1526.
5. **B. Song**, Q. Jiang, Z. Cao, *On-line calculation and analysis of heat efficiency on circulating fluidized bed boiler unit*, ***Chemical Industry and Engineering Progress***, 2008, 4:32-37. (in Chinese).

Conference Proceedings:

1. **B. Song**, H. Yuan, C. J. Jameson, S. Murad, *Nanoparticle permeation-induced water penetration and ion transport through a lipid membrane*, ***Proceedings of AIChE Annual Meeting***, Pittsburg, PA, USA (2012), accepted.
2. H. Yuan, A. Raze, **B. Song**, S. Murad, *Treated waste water source heat pump design and improvement*, ***Proceedings of AIChE Annual Meeting***, Pittsburg, PA, USA (2012), accepted.
3. **B. Song**, H. Yuan, C. J. Jameson, S. Murad, *Investigations on permeation of functionalized nanoparticles through lipid bilayers using molecular dynamics simulations*, ***Proceedings of AIChE Annual Meeting***, Minneapolis, MN, USA (2011).
4. **B. Song**, Q. Jiang, Z. Cao, *Optimization of heat efficiency of CFBB by orthogonal analysis based on artificial neural network*, ***Proceedings of World Congress of Intelligent Control and Automation***, Chongqing, China (2008) (in Chinese).
5. Z. Cao, H. Zheng, Q. Jiang, **B. Song**, *Dynamic modeling and control program simulation for a sterilization cauldron*, ***Proceedings of International Conference on Mechatronics and Machine Vision in Practice***, Xiamen, China (2007).